Multifunctional Polymer Fiber Probes for Biomedical Application

Jongwoon Kim

Dissertation submitted to the faculty of the Virginia Polytechnic Institute and State University in partial fulfillment of the requirements for the degree of

Doctor of Philosophy

In

Electrical Engineering

Xiaoting Jia

Daniel Fine English

Wei Zhou

Anbo Wang

Blake Johnson

May 2, 2024

Blacksburg, Virginia, USA.

Keywords: Multifunctional fiber probes, electrophysiology, optogenetics, drug delivery, tumor ablation, neural interface, cannabinoids, sharp wave-ripples, hippocampus

Multifunctional Polymer Fiber Probes for Biomedical Application

Jongwoon Kim

ABSTRACT

Biomedical devices play a crucial role in the healthcare system, enabling more effective treatments, less invasive procedures, and more precise diagnoses. Due to these compelling reasons, development of new biomedical devices and biomaterials have always been in high demand. Exploring and refining fabrication methods are essential to the development of new biomedical devices. Some of the common fabrication methods include microfabrication methods (photolithography and soft lithography), 3D printing (additive manufacturing), laser machining, thermal drawing, and electrospinning. The choice of fabrication methods heavily depends on the materials, geometry, and functionalities of biomedical devices. Currently, the thermal drawing process has proven to be an excellent scalable fabrication platform for neural interface, tissue engineering, tumor/cancer treatment, soft robotics, and smart textiles. This Ph.D. dissertation summarizes my research on the fabrication and validation of thermally drawn multifunctional polymer fiber probes for modern biomedical applications, primarily in the fields of neural interfaces and tumor treatments.

Understanding the neural basis of behavior requires monitoring and manipulating combinations of physiological elements and their interactions in behaving animals. Utilizing the thermal drawing process, we developed T-DOpE (Tapered Drug delivery, Optical stimulation, and Electrophysiology) probes and Tetro-DOpE (Tetrode-like Drug delivery, Optical stimulation, and Electrophysiology) probes that can simultaneously record and manipulate neural activity in behaving rodents. Taking advantage of the triple-functionality, we monitored local field potential (LFP) while manipulating cannabinoid receptors (CB1R; microfluidic agonist delivery) and CA1 neuronal activity using optogenetics. Focal infusion of CB1R agonist downregulated theta and

sharp wave-ripple oscillations (SPW-Rs). Furthermore, we found that CB1R activation reduces sharp wave-ripples by impairing the innate SPW-R-generating ability of the CA1 circuit.

Microscale electroporation devices are mostly restricted to in vitro experiments (i.e., microchannel and microcapillary). We developed a flexible microscale electroporation fiber probe through a thermal drawing process and femtosecond laser micromachining techniques. The novel fiber microprobes enable microscale electroporation and arbitrarily select the cell groups of interest to electroporate. Successful reversible and irreversible microscale electroporation was observed in a 3D collagen scaffold (seeded with U251 human glioma cells) using fluorescent staining.

Leveraging the scalable thermal drawing process, we envision a wide distribution of multifunctional polymer fiber probes in research facilities and hospitals. Along with the fiber probes presented in this dissertation, additional insight and future perspective on thermally drawn biomedical devices are discussed.

Multifunctional Polymer Fiber Probes for Biomedical Application

Jongwoon Kim

GENERAL AUDIENCE ABSTRACT

The thermal drawing process is a versatile and scalable platform for fabricating functional fiber technology. The process was formerly adapted from fabrication method for silica optical fibers, widely used in telecommunication (e.g., telephone, internet, cable TV, etc.). To name some functionalities of these fibers, they can move, hear, sense touch, change colors, harvest and store energy, record and manipulate brain activity, and ablate tumors. As imagined, these functionalities are derived from the unique geometry and functional materials embedded along the fiber. Therefore, developing the fiber design tailored to a specific application is a critical step to making a successful fiber product. In this dissertation, I will present my work on biomedical devices fabricated with the thermal drawing process and their application in neuroscience and tumor/cancer treatment.

Utilizing the thermal drawing process, we developed neural interfaces that can be implanted into the deep brain and record and simultaneously manipulate the neural activity. These neural interfaces (Chapter 2,3; T-DOpE and Tetro-DOpE probes, respectively) are able to record both local field potentials (LFP; activity of thousands or more neurons) and single action potentials (single on/off signal from individual neurons nearby). By manipulating the gene expression, we can control the activity of neurons with specific light (λ= 470nm; blue light) exposure. We implemented optical waveguide in our probes to guide light from a laser source to the tip of the probe and manipulate the neural activity. Furthermore, we fabricated micro-channels within the device to enable focal drug delivery at the tip of the device. Using the T-DOpE probe, we studied the effect of local synthetic cannabinoid injection in the hippocampus. We found that the local

injection of the drug in hippocampus CA1 makes neurons incapable of generating sharp wave-ripples (a neural signal associated with memory).

Electroporation is a biophysical phenomenon where short high electric field pulses introduce nanoscale defects in cell membrane. These defects can cause unstable cellular homeostasis and eventually leads to cell death. Due to reduced treatment time, no heat effect, and tissue selectivity, electroporation has been used in clinical trials for cancer treatments. Using the thermal drawing process and laser micromachining techniques, we developed a flexible microscale electroporation fiber probe capable of ablating tumor cells.

Due to the low-cost and scalability of thermal drawing process, we envision the use of thermally drawn functional fiber technology in biomedical fields. In this dissertation, I also address some challenges and future directions of thermally drawn functional fibers in biomedical fields.

Dedication

I dedicate this work to my mom, Shinae Koh, and my dad, Changkyu Kim. To my mom and dad, whose love, sacrifice, wisdom, and encouragement have illuminated my path to this achievement, your affection and compassion are the foundation of my success. Thank you for believing in me and standing by my every step of the way.

Acknowledgements

At the end of this journey, I have come to realize that this pursuit of PhD was not only for the sake obtaining a higher degree, but maturing my scientific intuition, strengthening my mental resilience, and learning to work and learn from colleagues and collaborators. Nothing would have been possible without support, assistance, and encouragement from advisors, mentors, professors, friends, and family.

To my advisor and mentor Dr. Xiaoting Jia: I joined your lab with no experimental skills, just writing and validating Matlab codes. You taught me the joy of being an experimentalist and I thank you for your patience and trust in me to become one. You have taught me to be a better scientist, engineer, and above all, a better person. I appreciate the time and freedom to explore different fields and crazy ideas. Thanks to this, I was able to discuss and brainstorm many ideas with many professors, which broadened my collaborative nature. Thank you for taking me in as your student. I will forever be grateful for all the help and support from you.

To my neuroscience mentor Dr. Daniel English: Coming in without any neuroscience background, you have been patient and supportive of me through the last few years. I have learned a lot from you and every time we talk, I learn something new about neuroscience. You have taught me what it's like to be a neuroscientist and to work with them. I am very grateful for the support, wisdom, and help along my PhD journey. I hope you miss me when it's time to eat lunch.

To my committee members, Dr. Anbo Wang, Dr. Black Johnson, and Dr. Wei Zhou: I thank you for the fruitful collaborations, support and advises during my time at VT.

To Ziang, Shan, Yujing from Jia lab: Thank you guys for all the support, guidance, and mentorship. I would not have become the engineer I am today without you guys.

To Hengji from Jia lab: I thank you for all the time we've spent together working, eating, and playing. I will always miss your jokes and mochis. I have enjoyed discussing and engineering our way out of problems. I hope you finish your PhD strong, and I am very proud of you.

To Alex, Yue, Astrid from Jia lab: I have enjoyed your company in the lab. I hope things go well in whatever you guys do in the future.

To Earl and Kaiser from English Lab: Thanks for the collaboration and working with me and Jia lab over the years. I hope you learned as much as I did from you guys. I am going to miss talking with you guys, hanging out, playing games, and learning from each other.

To Chelsea, Alana from English Lab: I enjoyed talking with you in the lab. Chelsea, I thank you for all the life wisdom and advice. Alana, I thank you for your optimism and energy.

To my collaborators, Shuo, Yajun, Ruixian, Alec: I thank you all for working with me on different projects. You all made me more knowledgeable in the field of fiber optics, electroporation, and photometry.

To my friends: Gibong, Jaewon, Myojoong: We all joined the VT PhD program on the same day, it has already been 6 years since. I appreciate all the nights drinking and talking nonsense. I would not have kept my sanity if not for you guys.

To my family, Jongyup, Catherine, and Peter: Thank you for your support and believing in me. It helped me a lot to know my family is always cheering for me.

To my love, Esther: We've met on my first year in PhD. I appreciate you standing by my side throughout my PhD journey. You sympathized with me when my manuscripts were rejected and celebrated when accepted. I always appreciate you "trying" to explain my work to others. I have learned to be more caring and emotional. Thank you for always supporting me with my work and what I do. You encourage me to be a better person every day. I can't wait to start the next chapter of our life together. Thank you for your love and Green Card.

I would also like to acknowledge my friends who have kept me sane and motivated during this journey. Thanks for playing tennis with me Cheolhei, Jihoon, Hyunggon, Hanjoon, Seokgyun, Seongbee, and Mincheol. Thanks for hanging out and drinking with me in Madison Kelvin, Yuri, Ian, Hyungjoo, Jenna, Milton, Dasol, Byeonguk, Veronica, and Sangmin. Thanks for games with me for daily/weekly dopamine kicks: Joel, Yeji, Hanju, Ginnay, Issac, Patrick, Eric, Phillip, Bedrow, Mat, Wookie, SY, Sook, Jihun, and Hyeonmyeong.

Table of Contents

Chapter 1
Introduction

In the late 1970s, telecommunication companies began to widely use fiber optics in their communication network systems.[1, 2] For many years, the fabrication and characterization of silica optical fibers have been modified and refined to enhance the optical properties of fibers for the telecommunication industry.[2-5] However, in the recent decades, functional multimateral fibers have been developed to explore other various modalities, such as electrical, chemical, and magnetic modes, delving into novel microstructure fiber designs and a wide range of materials, including polymer, metal, semiconductors, composites, etc.[6-11] Similar to the fabrication process for silica optical fibers, a preform, a macroscale design of the desired functional fiber, is heated inside a furnace and controllably drawn to produce a fiber in a remarkably scalable way. The functional fiber inherits the proportionally miniaturized cross section of the preform while maintaining all complex functionalities.[6-8, 10] Some of these functionalities include piezoelectricity[12-15], triboelectricity[16-20], energy storage[21, 22], and optoelectronics.[23-28] Today, fiber technology is implemented in many industries for a variety of applications[6, 7, 9, 10, 29-32], such as tele-communication, biomedical engineering, sensing and modulating technology, photonics and optoelectronics, defense and aerospace, soft robotics, smart fabric and textile, etc.

In this chapter, I first introduce the fabrication method of thermal drawing and the materials embedded in the flexible fibers that enable useful functionalities. Then, I present the biomedical applications of the functional fibers, namely in neural interfaces, chemical sensing, tissue engineering, tumor and cancer treatment, programmable soft robotics, and smart fabrics and textiles (Fig. 1.1).

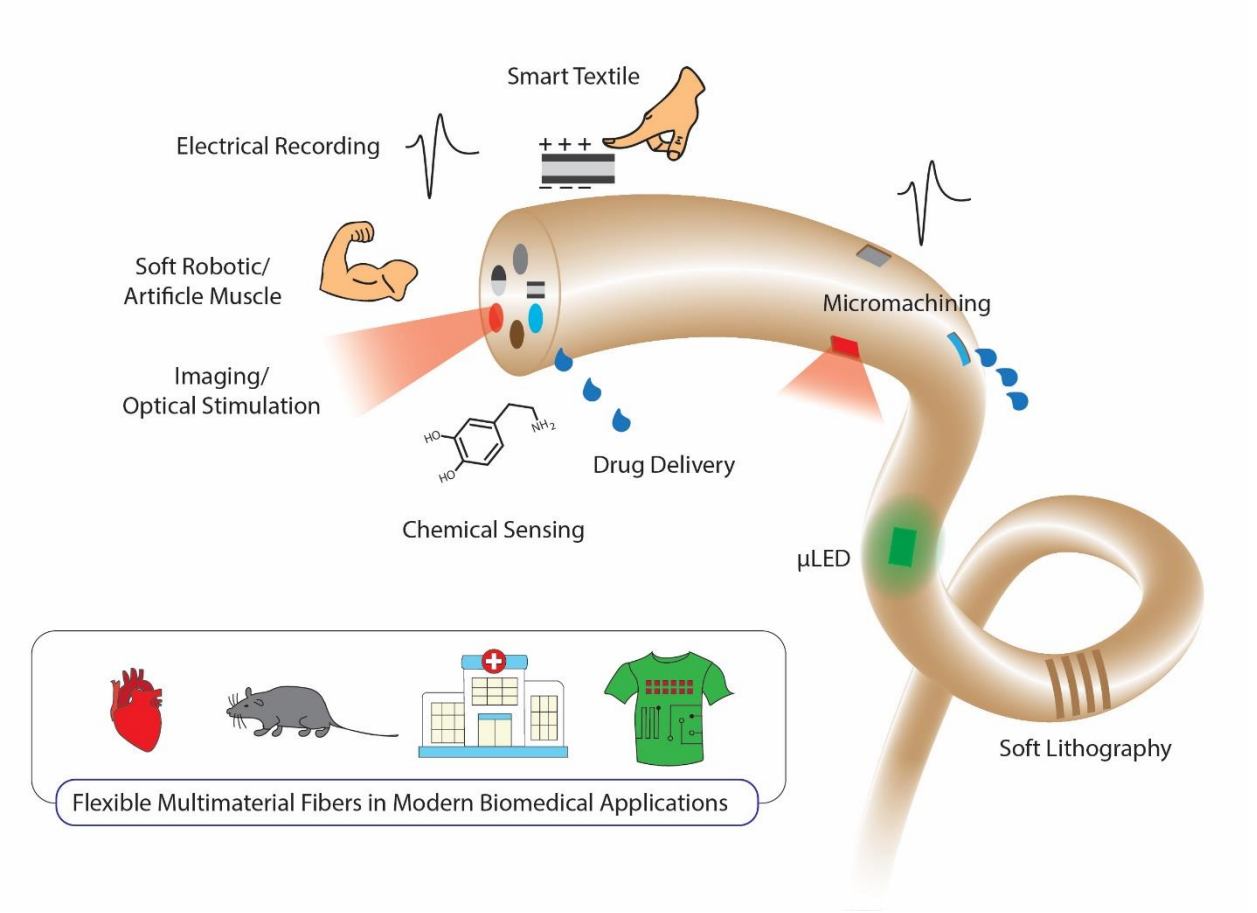

Figure 1.1: An overview of flexible multifunctional fibers in modern biomedical applications. Using the thermal drawing process, the fibers developed for biomedical fields can record electrochemical activities, deliver light, inject drug, measure neurotransmitter, actuate like muscles, and feel pressure. Post processing along the fiber length, such as surface patterning[33-35], bundling[36, 37], and microelectronics attachments[38], further increases the functionality and practicality of the fiber technology. Currently, these fibers are utilized and hold promising potentials in investigating organs and central nervous system (e.g., heart and brain) of animal models, aiding in diagnosis and treatment in healthcare, and increasing the functionalities of traditional fabrics and textiles.

1.1 Fabrication Method of Thermal Drawing

The very first step for fabrication functional fibers through thermal drawing process is designing and manufacturing of a preform.[6, 7, 9, 39] A preform is an initial macroscopic structure designed and fabricated for the thermal draw. The preform has the scaled up, but identical cross-sectional geometry and materials as the final fiber.[40] The cross-section dimensions and length of

the preform influence the overall length of the fiber.[6, 10] For example, a kilometer-long fiber would require a longer preform than a preform to produce hundreds-of-meters-long fiber. The design and composition of the preform are critical as they define the properties and functionalities of the produced fiber. The preform can include a wide range of functional materials such as thermoplastics, semi-crystalline, nanocomposites, metals, and semiconductors.[6, 7, 9, 10, 39] Some of these materials require an additional step of extracting water molecules trapped in the materials. This ensures a stable thermal draw without any defects in the resulting fiber from water vapor. The preform is meticulously designed and assembled utilizing various approaches including traditional machining techniques (milling, drilling, and trimming), thin film rolling, extrusion, and stacking.[28] Often, the finished preform is wrapped in a sacrificial layer to increase the stability of the draw and may be mechanically or chemically etched after the thermal draw. Lastly, the preform is consolidated in a vacuum oven with the appropriate temperature.

The preform is mounted in a draw tower, where it is softened and pulled into a fiber.[6, 7, 9, 10, 39] The draw tower usually consists of a furnace, a motor to feed the preform, a capstan to pull and draw fiber, a tension sensor, and two-dimensional laser scanner. A furnace for drawing polymer fibers typically requires three temperature zones: Top zone preheats the preforms, middle zone softens the preforms and produce fibers, and the bottom zone cools the fibers.[40] The precise temperatures of the three zones depend on the thermal properties of the preform materials. It is essential that the preform is heated in the furnace and becomes sufficiently viscous to achieve a stable thermal draw. The fiber dimension and length are controlled by precisely regulating the furnace temperature, the preform feeding speed, and the fiber drawing speed. The stress built up in the fiber during a thermal draw is computed from the measurements

obtained from the tension sensor and the laser scanner. In some cases, fibers are drawn in high stress to neutralize the surface-tension effect of the melted materials in the preform.[28, 40]

1.2 Materials and Functionalities

The thermal drawing process is a versatile platform and accommodates a wide range of materials enabling fabrication of functional fibers.[6, 7, 10] Again, the selection and integration of materials in the preform design are critical as they specifically impact the fiber functionalities. Some intrinsic properties of the materials noteworthy are mechanical, electrical, thermal, optical, chemical, and magnetic properties.[41-45] Functional materials can serve as essential elements in functional fibers as they possess specific native properties and behaviors that respond to external stimuli in a useful and controlled manner.[46] To give some examples, shape memory alloys can return to their original shape above a certain temperature.[47, 48] Thermoelectric materials convert temperature differences into electrical voltage.[48, 49] Similarly, piezoelectric materials generate an electric charge in response to mechanical stress and deformation.[50, 51] Photovoltaic materials are especially useful in solar cell technology as they convert sunlight into electricity.[52, 53] However, thermal drawing a combination of materials and integrating them into a single fiber may not be trivial due to the differences in thermal and mechanical properties of materials.

The optimal drawing parameters may vary drastically even within the same preform materials with respect to the geometry and the volume of each material. For example, a tube of polycarbonate preform would require less time to preheat before it can be pulled into a fiber than a solid rod polycarbonate preform. This allows for a higher feeding speed for the tube preform than for the solid preform. First, we present some guidelines for a successful thermal drawing of a multimaterial fiber. Afterward, some advice for convergence thermal drawing is discussed. (1) The preform must have at least one material that withstands the drawing stress while deforming

controllably, allowing the preform to transform into a fiber in the furnace neck-down region.[6, 40] This material may be critical if co-drawn with low-temperature metal as the material must withstand a high stress to counter the Plateau–Rayleigh capillary instability.[28, 40] Additional sacrificial layers of polymer may be employed to stabilize the thermal draw. (2) Other materials should have lower viscosity than the material in (1) during the thermal. If not, materials may break or crack under high stress.[6, 28, 40] For example, a high concentration of carbon in conductive polymer is probable to break during a thermal draw due to high viscosity. One way to avoid the break is to increase the temperature such that the conductive polymer is less viscous during the draw, which might lead to a change in the cladding material. (3) Lastly, materials should exhibit similar thermal properties such that there is no breakage or cracks caused during the rapid thermal cooling.[6, 28, 40]

On the other hand, the recently developed convergence drawing process enables co-drawing of multimaterials while violating some guidelines mentioned above. In the case of convergence drawing[10, 54], the preform is fabricated with empty channels where the material with high melting temperature (e.g., tungsten microwires and microelectronics) are fed into during the thermal drawing. In the neck-down region, the preform is pulled into a fiber and the empty channels collapse onto the material, encapsulating it in place. It is critical that the capstone speed is identical to the feeding speed of the material (microwire) to avoid a deformed fiber or breakages in the hard material. This method broadened the possible materials thermally drawable, enabling and increasing functionalities, such as superior electrical properties and embedment of microelectronics.

1.3 Application in neural interfaces

Implantable neural interfaces are important tools to study neural dynamics and find treatments and cures for neurological disorders and diseases.[72-75] Traditionally, tetrodes[76] and Utah arrays[77] were commonly used for high quality recording of extracellular activities (single units and LFP).[78-80] The electrodes on these devices enable localized manipulation of electrical current, resulting in neuronal excitations nearby.[72] With the recent advancements in fluorescence sensor[81, 82] and optogenetics,[83-85] identifying, recording and manipulating different cell types have been achieved and widely used.[86] This advancement naturally led into an explosion of novel and innovative bi-directional devices with electrical and optical modalities.[87-90] Amongst many new neural probes, polymer fiber probes, fabricated using the thermal drawing process, are being actively developed and utilized as flexible, multifunctional neural interfaces to study the brain circuitry.

The scalable thermal drawing process makes a very appealing platform for fabricating neural probes for its high yield and the inherent geometry of a fiber, suitable for implants. Fig. 1.2a shows the first realization of thermally drawn polymer fiber as flexible, multifunctional neural interface.[91] In this fiber, conductive polyethylene (CPE) served as recording electrodes. Polycarbonate (PC) wrapped in cyclic olefine copolymer (COC) was utilized as the optical waveguide of the fiber. The microfluidic channel enabled focal drug delivery at the tip of the fiber. In fig. 1.2b, platinum, gold, and copper were drawn with the fiber via convergence thermal drawing process, enabling lower impedance compared with the conductive composites.[92] One-step optogenetics was first demonstrated by infusing viral vectors to express channelrhodopsin 2 (ChR2) in medial prefrontal cortex (mPFC) with the fiber probe's microfluidic channel, as shown in fig.

1.2c.[93] This process removes the extra steps of cannula extraction and probe insertion and enables colocalized expression, light delivery, and electrophysiology recording.

From these initial generation of fiber neural probes, several innovative designs and/or additional methods were included to enhance the feature density, reduce tissue damage, and expand functionalities. Fig. 1.2d presents a platform that enables fiber probes to interface with the brain in 3-dimension via a helical scaffold.[34] The spatially expandable probes allow simultaneous monitoring and manipulation of neural activities from different regions of the brain with a single insertion point. By measuring electrophysiology from different regions of the brain in an epileptic mouse model, this probe showed a promising potential in studying neurological diseased brain across different regions. In fig. 1.2e, a two-step and convergence thermal drawing was revisited for consistent and easier fiber drawing.[94] These neural probes were mounted on a custom developed microdrive to enable depth-resolved investigation of neural circuits. Furthermore, the fiber probes showed a high compatibility with magnetic resonance imaging (MRI) even with an infusion of MRI contrast agent through the microfluidic channel. To enhance the biocompatibility and feature density of the fiber neural probes, Park et al. devised a hybrid fiber probe by integrating the polymer fibers within a hydrogel matrix.[36] Fig. 1.2f illustrates the fibers used in the fabrication of the hybrid probe and the hydrogel bonding techniques. These probes chronically recorded sorted single units over 6 months following implantation. Using multifunctionality of the flexible fibers to its fullest potential, microelectronic fibers were implanted into the ventral tegmental area (VTA) and gut (fig. 1.2g).[38] By coupling these fiber probes to NeuroStack, wireless optogenetic modulations in the brain and the gut were achieved. Sucrose solution injected through the microfluidic channel in the gut probe while simultaneously recording the spike activity in the VTA neural probe. Utilizing these probes, they discovered that optogenetic modulation of vagal

afferents from intestinal lumen was enough to induce a reward phenotype. Apart from using optogenetics or electrical stimulation to manipulate neural activity, fig. 1.2h presents a multifunctional fiber-based optoacoustic emitter probe to excite neurons with acoustic waves.[95] Using a controlled micro-injection process, an optoacoustic coating was deposited at the tip of the optical waveguide, which was fabricated via thermal drawing process. With nanosecond pulses of 16.6 uJ laser, a peak-to-peak pressure of 1.0 MPa was measured, which is sufficient to stimulate a neuron. Due to the intrinsic ability of neurons to respond to acoustic waves, no viral transfection is required for this specific modulation. Fig. 1.2i presents flexible electrofluidic neural interface for non-human primates (NHPs) with four electrodes and two microfluidic channels.[96] In this work, Garwood et al. locally infused γ-aminobutyric acid (GABA) to premotor cortex and putamen of rhesus macaque while simultaneously recording electrophysiology. Although they found some changes in single-unit firing rate and oscillatory structure of LFP after infusion, they did not observe any consistent changes in behavior. Recently, a thermal tapering process was developed to overcome the inherent challenge in backend connection (fig. 1.2j). The tip of the probe is miniaturized to reduce tissue damage while the large backend enables industrial scale connectorization.[97] Using the tri-modality of the probe, Kim et al. found local infusion of cannabinoid receptor agonist is sufficient to disrupt sharp wave-ripples generation regardless of CA3 inputs. In result, the thermal drawing process is an excellent platform for developing and fabricating novel deep-brain neural interfaces to study and understand the brain circuits.

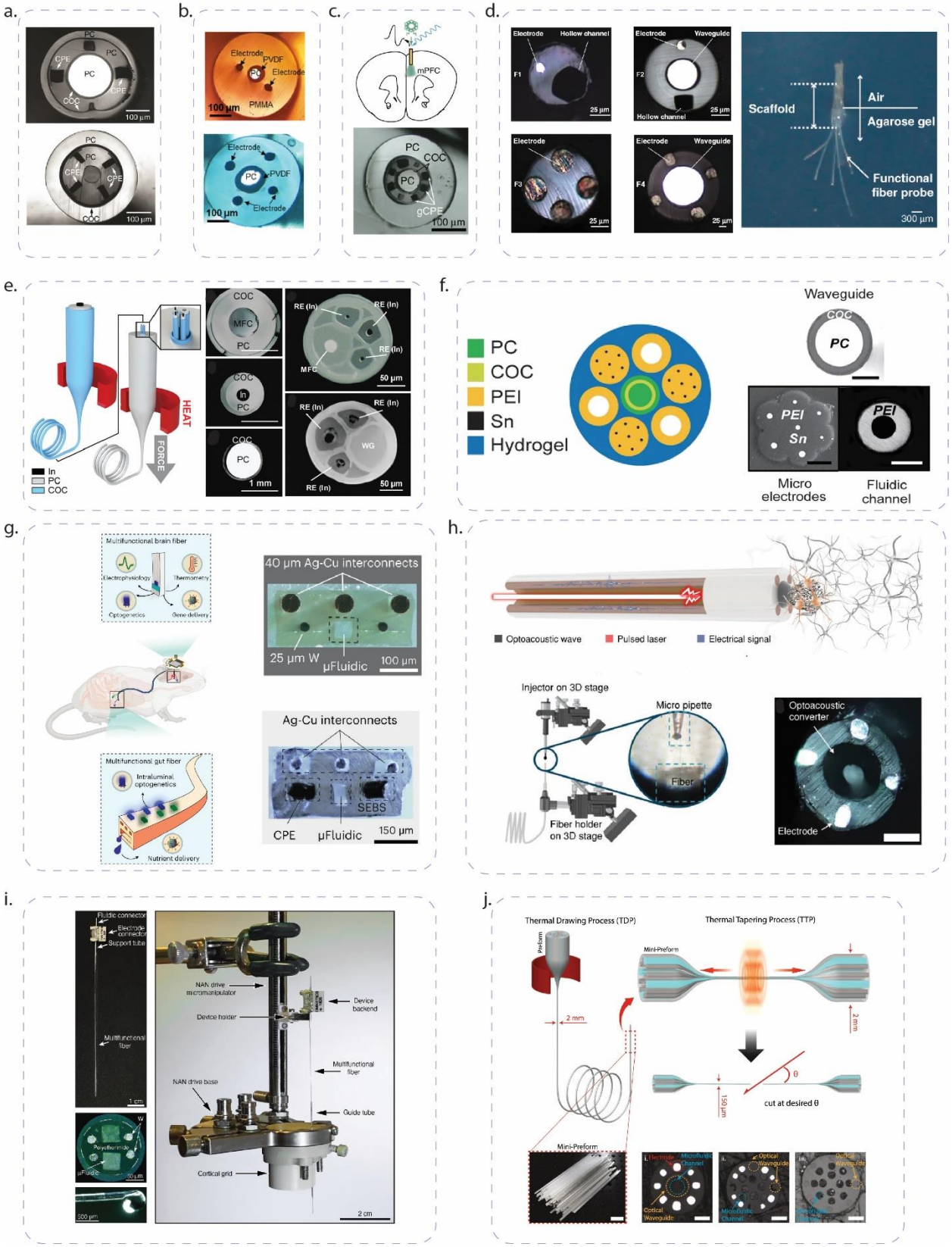

Figure 1.2: **Thermally drawn multifunctional fibers for neural interface. a.** Cross-sections of the first realization of neural fiber probes. Reproduced with permission[91]. Copyright 2015,

Springer Nature; **b.** Cross-sections of fiber neural probes with metal microwires using convergence thermal drawing process. Reproduced with permission.[92] Copyright 2021, John Wiley and Sons; **c.** One-step optogenetic fiber probe allows colocalized expression, recording, and optogenetics. Reproduced with permission[93]. Copyright 2017, Springer Nature; **d.** Spatially expendable fiber probes enabling multisite recording and manipulation across different regions. Reproduced with permission[34]. Copyright 2020, Springer Nature; **e.** MRI compatible multifunctional fiber neural probe. Reproduced with permission.[94] Copyright 2021, John Wiley and Sons; **f**. Modular integration of fiber probes and hydrogel to increase biocompatibility. Reproduced with permission[36]. Copyright 2021, Springer Nature; **g.** Simultaneous interrogation of sensing and delivery of sucrose in the gut while recording from the brain. Reproduced with permission[38]. Copyright 2023, Springer Nature; **h.** Optoacoustic fiber probe to stimulate neuronal activity. Reproduced with permission.[95] Copyright 2021, John Wiley and Sons; **i.** First implantation of multifunctional fiber neural probe in a non-human primate. Reproduced with permission.[96] Copyright 2023, AAAS; **j.** Thermal tapering method to ease the backend connections of fiber probes. Reproduced with permission[97]. Copyright 2024, Springer Nature.

1.3.1 Application in chemical sensing

In the central nervous system, balanced neurochemicals are essential in maintaining a healthy brain function.[98, 99] Recent studies have revealed that neurological, neurodegenerative, and psychiatric diseases are directly associated with neurochemical abnormalities in the brain.[100, 101] However, the presence of high concentrations of interferent molecules forms a formidable obstacle for current technologies to accurately monitor the low concentrations of targeted neurochemicals.[102] Microdialysis is a conventional FDA-approved sampling technique to monitor extracellular concentration.[103-106] However, time delay and concentration diffusion of targeted neural chemicals are unavoidable due to its inherent complications in sampling techniques.[106] Over the recent years, pH and neurochemical fiber sensors have been developed to record real-time neurochemical fluctuations.

In-brain pH has been shown as a critical factor in maintaining normal brain function.[101, 107-110] In fig. 1.3a, Booth et al developed two designs of fiber probe with graphite-doped electrodes to monitor pH and neurometabolic lactate.[111] For pH sensors, iridium oxide was layered on the electrodes, which are responsive to pH within the physiological range. As for the lactate biosensors,

enzyme was layered on top of the platinum black growth on the fiber electrodes. These probes were tested in an in vivo mouse model, presenting tools to study molecular mechanisms in the brain. Fig. 1.3b presents a three-electrode (conductive polycarbonate and platinum based metallic glasses) electrochemical fiber sensor.[112] Richard et al used cyclic voltammetry and chronoamperometry to detect and quantify paracetamol, a commonly used anesthetic drug. In fig. 1.3c, Guo, et al developed a pH fiber probe for spatially resolved and label-free pH sensing utilizing a light-addressable potentiometric sensor coupled to a flexible multimodal fiber.[113] This probe enables monitoring of pH changes over 14 pixels simultaneously with a spatial and temporal resolution of 250 μm and 30 Hz respectively. In this work, the probes were implanted into the hippocampus of rats and recorded pH changes over multiple pixels at both physiological and pathological conditions. Fig. 1.3d demonstrates a fiber probe which enables neurochemical sensing with high sensitivity and selectivity.[114] Saizaki et al developed a method to immobilize aptamers on the fiber microsensor. The aptamers were tagged with ferrocene as electrochemical readout of the binding between the aptamer and the target molecule. In this work, they focused on the dopamine sensing and showed high detection of dopamine selectivity in complex in vivo settings. They successfully monitored electrically induced dopamine release and electrophysiology across different brain regions. Overall, the thermal drawing process is a promising fabrication method for neurochemical sensing. However, the neuroscience community would greatly benefit from multifunctional fibers with photometry capability, as photometry is a standard neurochemical sensing nowadays.

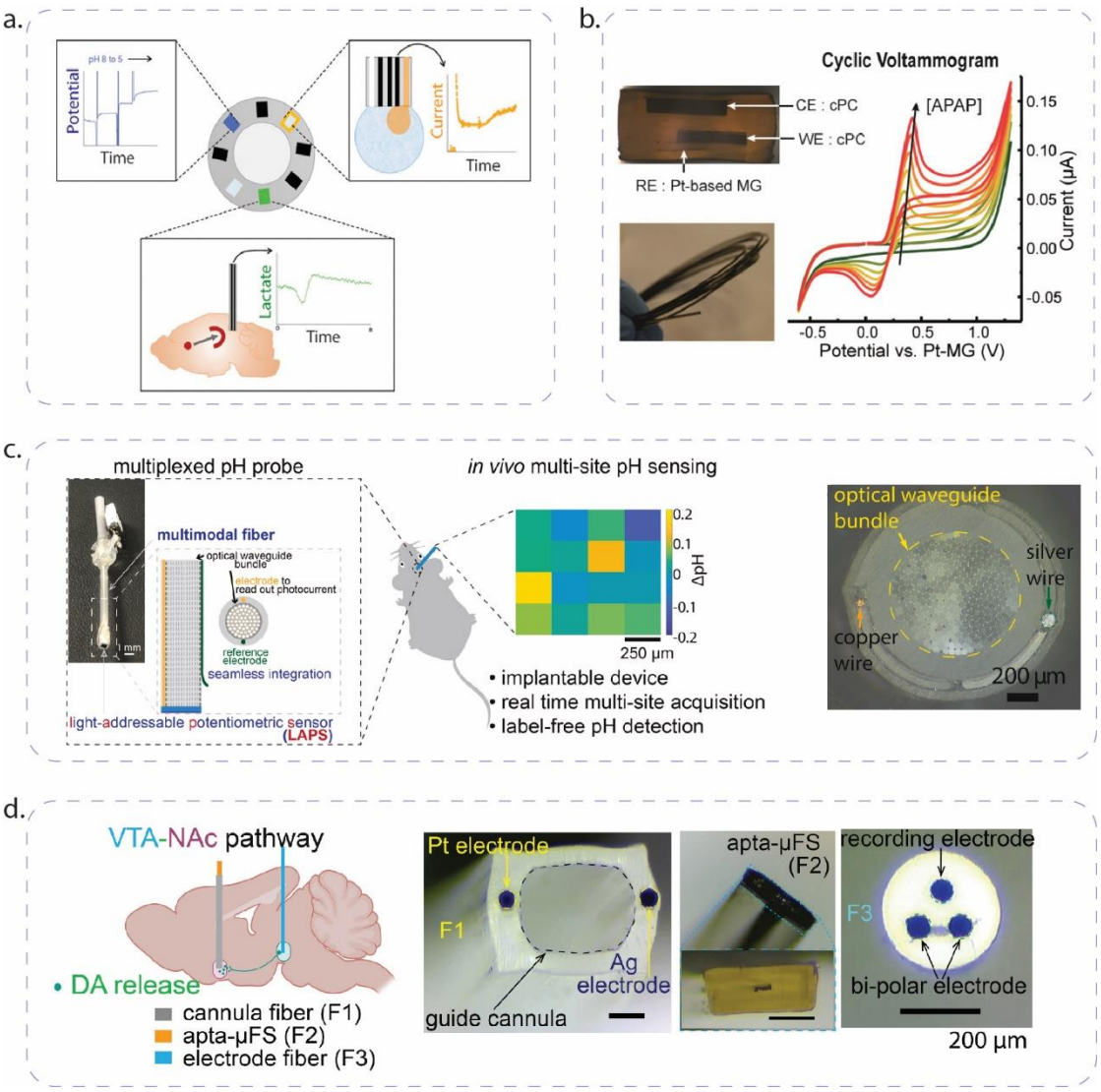

Figure 1.3: **Chemical sensing fibers mainly developed for neural applications. a.** Fiber electrodes doped with graphite for pH and neurometabolic lactate sensing in the brain. Reproduced with permission.[111] Copyright 2021, American Chemical Society; **b.** Fiber sensor that uses cyclic voltammetry and chronoamperometry to quantify paracetamol. Reproduced with permission.[112] Copyright 2021, American Chemical Society; **c.** Utilizing a light-addressable potentiometric sensor integrated with fiber probe, spatially resolved and label-free pH sensing was realized. Reproduced with permission.[113] Copyright 2021, Elsevier; **d.** Dopamine sensing and electrophysiology recording using aptamers on the fiber sensing tip. Reproduced with permission.[114] Copyright 2023, American Chemical Society;

1.4 Application in Tissue Engineering

Injured neural tissue and pathway often result in life-long discomfort and disabilities.[115-118] Nerve guidance scaffold to promote axonal growth can provide a therapeutic solution to the severed neural pathways.[119-122] Commercially available guidance scaffolds are often limited by either flexibility, geometry, length, or biocompatibility.[123] Recently, new scaffolds have been developed through many different methods such as molding, extrusion, freeze drying, freeze drying, 3D printing, etc.[121, 122, 124-128]

A couple of innovative regenerative scaffolds have been fabricated using the thermal drawing process, investigating the appropriate geometry and materials for axonal growth. In fig. 1.4a, Koppes et al. fabricated polyetherimide (PEI) nerve guidance scaffold with variation in the geometry and core size (50 – 200 μm).[129] The scaffolds with dimensions larger than 40 μm and smaller than 150 μm were likely to host growing neurites. They found that microgrooves enhance the neurite growth within the thermally drawn fiber scaffold. Fig. 1.4b shows the regenerative scaffold produced using fiber drawing combined with salt leaching, which enable tunable cross sections and porosity.[125] The porous fibers were further arranged into complex scaffold geometry utilizing filament surface heating fuse-printing. These porous scaffolds showed enhanced performance in sensory neuron growth compared to non-porous scaffold with identical material and geometry. As a result, the scalable thermal drawing process is a promising platform for neural tissue engineering due to its fine control over microscale features and adaptability with wide range of biocompatible materials.

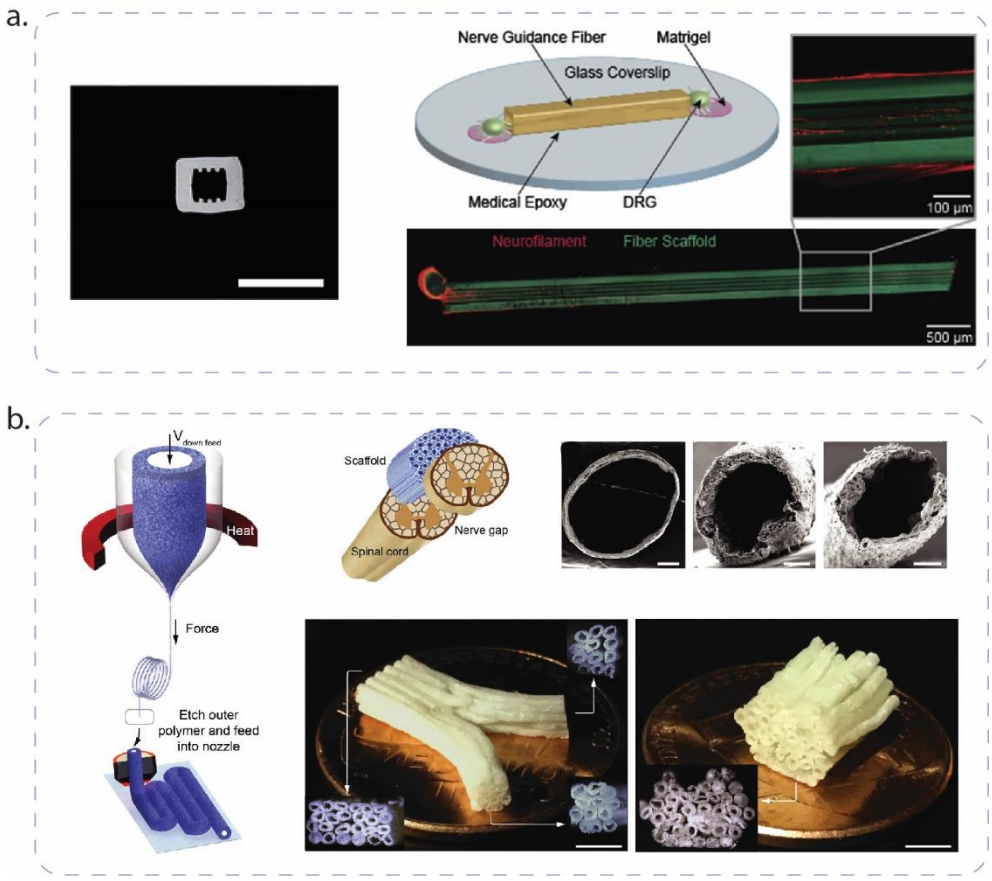

Figure 1.4: **Thermally drawn fibers as nerve guidance scaffold: a.** Polyetherimide fiber with 50 µm inner diameter and microgrooves facilitate growing neurites. Reproduced with permission.[129] Copyright 2016, Elsevier; **b.** The porous fibers scaffolds, utilizing filament surface heating fuse-printing and thermal drawing, enhanced sensory neuron growth. Reproduced with permission.[125] Copyright 2019, John Wiley and Sons.

1.5 Applications in cancer/tumor treatment

Cancer ranks as the second leading cause of death globally.[130, 131] It is characterized primarily by the abnormal ability of tumor cells to proliferate and withstand apoptosis[132], which is essential for their resistance to conventional treatments like chemotherapy and radiotherapy.[133-137] Traditionally, treatment options were limited to surgery, radiation, chemotherapy, or in combination. However, recent advancements have highlighted the complex pathways involved in cancer's progression and how they can be targeted for therapy.[134, 138, 139] This has led to the

development of new treatments, including drugs, biological agents, and immune therapies, which, despite not significantly reducing mortality rates, offer hope for extending the lives of those with metastatic cancer.[134]

Current drug delivery strategies cannot sustainably supply drug, monitor therapeutic response, and adjust drug dose over the course of weeks. Chin et al developed an implantable fiber probe to deliver immune checkpoint blockade (ICB) antibodies through the microfluidic channel and monitor the tumor impedance measurement using electrodes over a few weeks (fig. 1.5a).[140] Using the optical waveguide in the device, they also applied photodynamic therapy which enhances the anti-tumor immunity and lengthens intratumoral drug retention. They discovered in multiple tumor models that photodynamic therapy with local ICB antibodies delivery cures/ delays tumor growth. Irreversible electroporation (IRE) treatment applies pulses of high magnitude electric field to increase the permeability of the cell, thereby disturbing the cellular homeostasis and leading to cell death.[141, 142] IRE has some key advantages over the traditional methods, such as reduction in treatment time, absence of heat effect, sharp ablation regions, and tissue selectivity.[129, 141-143] Using thermal drawing process and femtosecond laser micromachining technique, Kim et al. developed a flexible fiber-based microscale electroporation device (fig. 1.5b).[35] The fiber-based device demonstrated microscale IRE in a 3D collagen scaffold seeded with U251 human glioma cells.

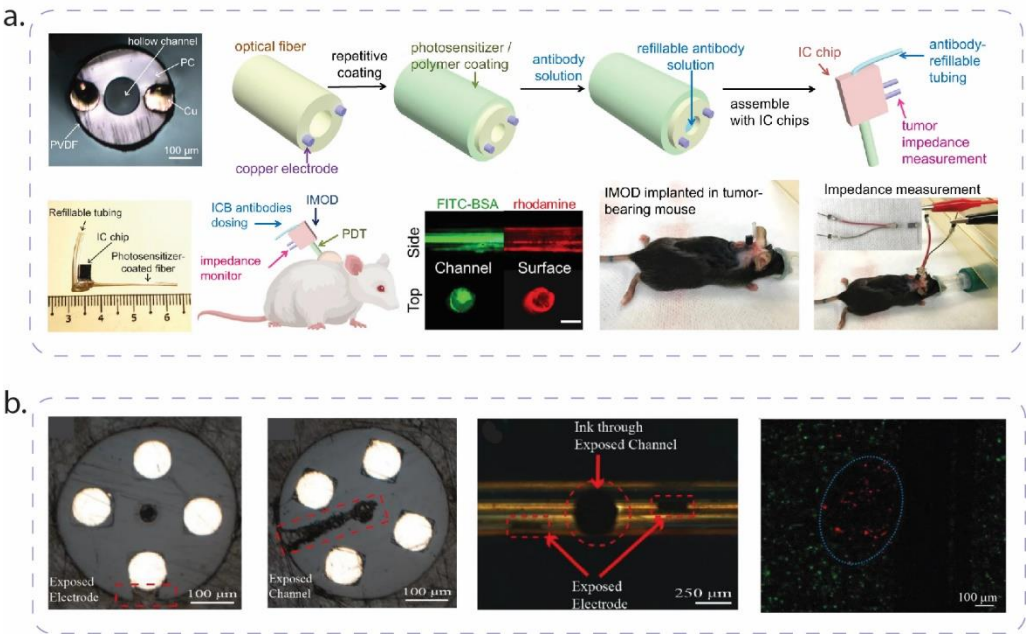

Figure 1.5: **Multifunctional fibers in cancer and tumor treatment: a.** Implantable fiber probe to deliver antibodies and monitor tumor impedance measurements. Reproduced with permission[140]. Copyright 2021, Springer Nature; **b.** Fibers with exposed microfluidic channels and electrodes enable microscale electroporation to ablate tumor cells. Reproduced with permission[35]. Copyright 2022, Springer Nature;

1.6 Application in Programmable Soft Robotic

From prosthetics, endoscopy, to minimal invasive surgery, multifunctional soft robotics hold high potential in biomedical applications.[57, 144-148] These soft robotics are often capable of navigating through biological environments through various methods[149, 150] such as pneumatics[151], hydraulics[152], shape memory[153], or magnetics[154]. Additionally, they are equipped with sensing and/or actuating modalities enabling functionalities such as imaging, monitoring, optical stimulation, and drug delivery.[154-157] Many soft robotics have been developed through fabrication techniques including molding, 3-d printing, thin film electronic fabrication techniques.[148, 150, 158, 159] However, soft robotics are often limited by the material and geometry realizable with these manufacturing methods.

The thermal drawing process is a promising platform for innovating soft robotics in tubular form which are favorable in biomedical applications such as endoscopy and minimal invasive procedures. Submillimeter fiber robot, presented in fig. 1.6a, have been developed which can navigate with external magnetic field, record and stimulate via electrodes, and deliver optical stimulation and pharmacological drug.[160] Utilizing the thermal drawing process, Zhang et al. integrated a fiber with electrical, optical, and microfluidic components with a ferromagnetic jacket around the fiber. The robotic fiber was inserted in a Langendorff-perfused mouse heart model, recorded intracardiac electrogram, monitored bioimpedance, and performed pacing. Irreversible electroporation was demonstrated to abolish tumor cells utilizing the electrodes at the tip and imaging capability through the optical waveguide was illustrated in this study. In fig. 1.6b, Leber et al demonstrated thermal drawing as an excellent platform for soft microstructure fiber robotics with complex and dynamic motion navigation with multiple advanced functionalities.[147] The highly accurate motion was achievable with tendon-driven techniques supported by a kinematic model. Optical waveguide, electrical wire, and fluidic channels within the fiber robotics enabled advanced functionalities such as 3-D scanning, proximity sensing, and optical delivery. This robotic fiber shows great potential for minimally invasive surgeries, capable of displacement sensing, imaging, and adapting autonomously to their surroundings. Three-dimensional soft robotics, as shown in fig. 1.6c, are fabricated with a combination of thermal drawing process, macroscale strain and magnetization programming.[161] To fabricate a bimorphic elastomeric fiber, cyclic olefin copolymer elastomer (COCe) and styrene-ethylene-butylene-styrene (SEBS) with empty channels were thermally drawn. Then, ferromagnetic neodymium–iron–boron (Nd2Fe14B) alloy particles with photocurable elastomer in infused into the empty channel of SEBS. After macroscale lateral strain and magnetization, these robots can be controlled by unidirectional

magnetic fields. Lee et al. demonstrate store cargo storage, navigation through space, and release of cargo by modulating the unidirectional magnetic field. Exploring the differential expansion within polymer bimorph structures, Kanik et al. fabricated strain-programmable artificial muscles using the thermal drawing process.[162] As shown in fig. 1.6d, COCe and high density polyethylene (PE) were thermally drawn with poly(methyl methacrylate) (PMMA) cladding. These fibers were cold drawn at strain of 50 to 1300 % to manufacture actuated spring, due to the deformation in PE. These spring-like actuators withstand more than 1000% axial deformation and can lift more than 650 times their own weight with thermal and optical manipulation, highlighting its potential in robotics and prosthetic limb applications. In fig. 1.6e, Sato et al developed a steerable fiber sensor consisting of shape memory alloy, such as NiTi or NiTiCu, and PC or PE as cladding.[163] Carbon nanofiber composite, optical waveguide, and microfluidic channel are embedded into the steerable fiber to enable biosensing, drug delivery, and light stimulation. The tip of the fiber was actuated with high spatiotemporal resolution by electrically activating the shape memory alloy. Additionally using their carbon nano composite, they should selective detection of adrenaline as low as 100nM. They targeted bifurcated vessel model and acquired localized adrenaline readout utilizing their fiber sensor, illustrating thermal drawing process as an outstanding platform for fabricating soft and flexible tubular robotics.

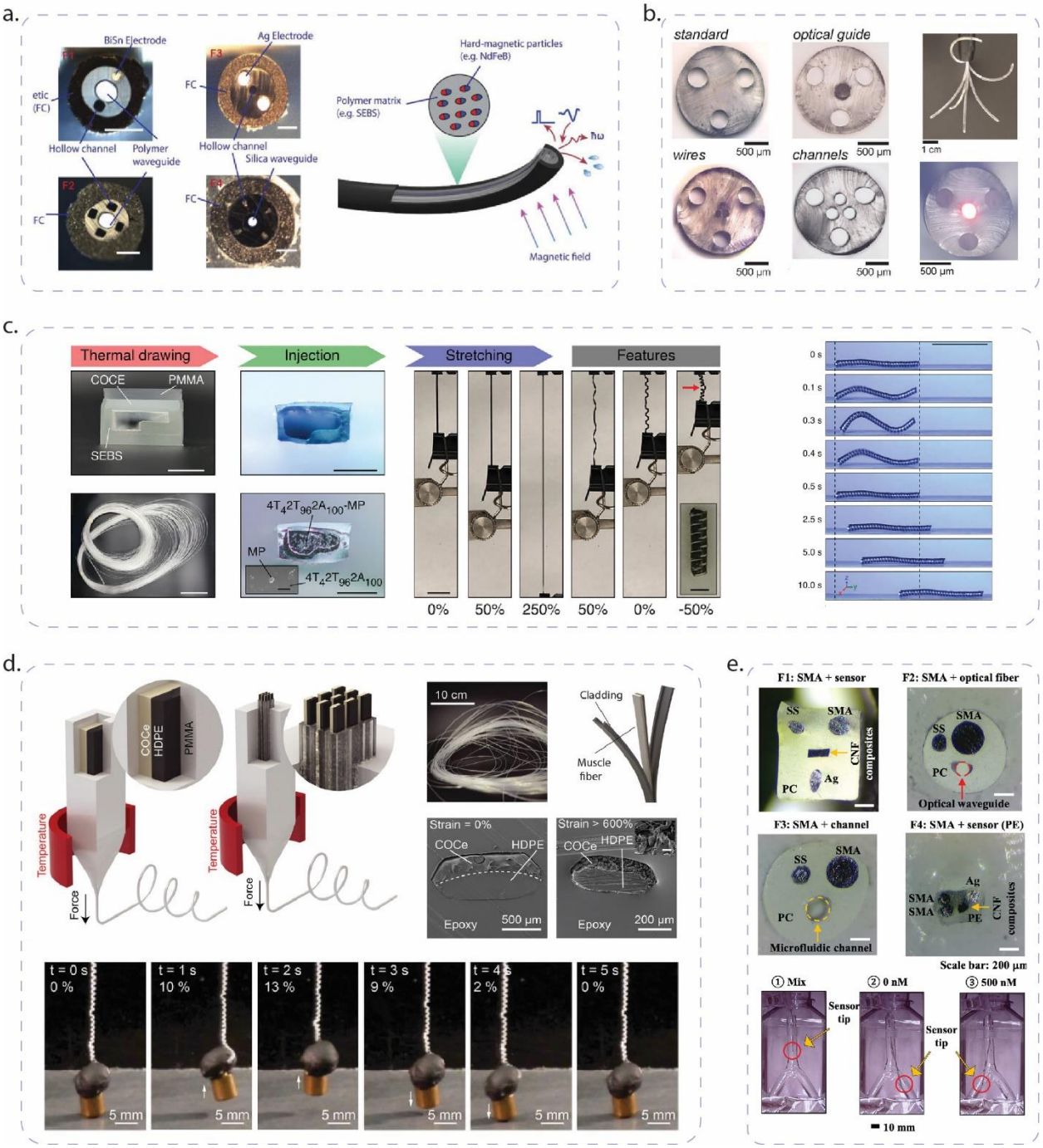

Figure 1.6: **Multifunctional flexible fibers as soft robotics: a.** Submillimeter fiber robot, which is navigated by external magnetic field, records and stimulate via electrodes and delivery light and drug. Reproduced with permission[160]. Copyright 2023, John Wiley and Sons; **b.** Tendon-driven technique to accurately move the fiber along with the multifunctionality. Reproduced with permission[147]. Copyright 2022, John Wiley and Sons; **c.** Bimorphic elastomeric fiber, fabricated with macroscale strain and magnetization programming, store cargo, navigate, and release cargo. Reproduced with permission[161]. Copyright 2023, John Wiley and Sons; **d.** Strain-programmable artificial muscle capable of lifting 650 times its own weight. Reproduced with permission[162].

Copyright 2019, AAAS; **e.** Biosensing and light and drug delivery fiber is steered with shape memory alloys. Reproduced with permission[163]. Copyright 2023, American Chemical Society;

1.7 Application in Smart Wearable and Textile

Flexible functional wearables and textiles are emerging as an ideal platform for many biomedical applications such as health monitoring, human-machine interface, and motion tracking.[164-169] Specifically, smart wearables and textile can offer useful insights into the user's health condition which can be utilized for disease prevention, enhanced clinical outcome, and improved quality of life.[167, 170] Many existing flexible skin-like sensors have been engineered with thin film fabrication techniques.[61-63, 167, 171] However, thermal drawing process has emerged as a powerful and scalable platform for manufacturing smart fabrics. These smart fibers are weaved into everyday wearables and textiles providing additional functions such as pressure and temperature sensing.[6, 7] Additionally, integration of the fiber through weaving presents certain benefits such as breathability, durability, and wear resistance.[6, 7]

Pressure sensing enables detection of mechanical stimulation and provides insights in compression, elongation, bending, and torsion of the fabric.[171, 172] In clinical settings, real-time recording of pressure exerted by human body on seats, beds, and shoes can enable faster diagnosis and personalized treatment and intervention. Usually, the pressure sensing in many functional wearables and textiles is realized by fluctuation in electrical resistance, capacitance, piezoelectricity, or triboelectricity.[172-175] In fig. 1.7a, Yu et al. presented thermally drawn functional fiber capable of measuring pressure or temperature.[176] The fiber consists of thermoplastic, TPE, and metal electrodes. For pressure sensing, they utilized a vector network analyzer to perform frequency domain reflectometry, which precisely provide the location of the pressured region. Using a similar set up, the temperature sensing was realized by the changes in frequency domain

reflectometry when the elastomer expends or shrinks due to temperature fluctuations. Fig. 1.7b presents a microstructure elastomeric fiber that consist of tens of liquid metal.[177] The pressure points were detected using the time-domain reflectometry. Even under two modes of deformation, stretching and pressing, the detected region of pressure points agreed with the actual pressure points. Triboelectric fiber with elastomer and liquid metal was fabricated using the thermal drawing process (fig. 1.7c).[17] Using this fiber, a finger gesture senor was developed where the output of the fiber increased as the bending angle increased. This fiber can also be worn around the torso and the triboelectricity due to the elongation and release motion during breathing can be measured through the output of the fiber. To simultaneously locate and quantify the pressure points, Leber et al. developed an elastomeric fiber with three small CPE sheets on top and a large CPE sheet at an incline on the bottom, as shown in fig. 1.7d.[178] With this clever design, the top electrodes came into consecutive contact with the inclined bottom electrode as the pressure on the fiber increases. Fibers were integrated onto a gymnastic mat for monitoring pressure distribution on a 2D space providing information on body position, posture, and motion. They successfully demonstrated that this set-up can significantly help patients prone to pressure ulcers. Wang et al thermally drew fiber with high performing silicon and germanium as crystalline semiconductors core with glass cladding. The glass cladding was removed by acid etching and the semiconductor fiber was redrawn with thermoplastics and metal wires using the convergence thermal drawing (fig. 1.7e).[24] The resulting optoelectric fiber was woven into other fabric and enabled a broad scope of applications. Real-time monitoring of photoresponse on a phone was achieved by weaving the fiber on a beanie. They demonstrated light fidelity (Li-Fi) based indoor communication system through integrating the fibers in daily clothing. Using photoplethysmography, heart rate was

monitored through weaving the fiber on a watch band. Lastly, they realized an underwater wireless communication system using the fiber.

Body temperature acts as a vital marker for an individual's health state, indicating potential infections and cardiovascular problems.[179] Fig. 1.7f presents a temperature fiber sensor thermally drawn with PLA doped reduced graphene oxide (rGO) core with linear low-density polyethylene (LLDPE) cladding and sacrificial polystyrene (PS).[180] The fiber sensor measured the temperature with high sensitivity and fast response within the physiological range. The durability of the fiber tested under various level of humidity, many wash machine cycles, and exposure to household chemicals. They demonstrate the feasibility of this temperature fiber sensor woven onto clothing and gloves with reliable performance.

Acoustic modality in biomedical application have advanced in the recent decades ranging from photoacoustic microscopy, drug delivery, to therapeutic ultrasound.[181] Acoustic fabric has promising potential in acoustic communications, acoustic health indicators such as heartbeat, and situational acoustic awareness.[13] Yan et al. developed an acoustic fiber that can detect audible sound and operate as a sensitive microphone utilizing the thermal drawing process (fig. 1.7g).[13] The acoustic sensing and actuating is achievable with a piezoelectric active layer, poly(vinylidene fluoride-trifluoroethylene) (P(VDF-TrFE)) loaded with barium titanate (BaTiO3) ceramic particles. The performance of the fiber, woven into a shirt, was demonstrated by successful directional detection and acoustic communication. Close contact between the fiber and the chest enables the fiber to record cardiac signals, presenting promising application skin interfaced stethoscope.

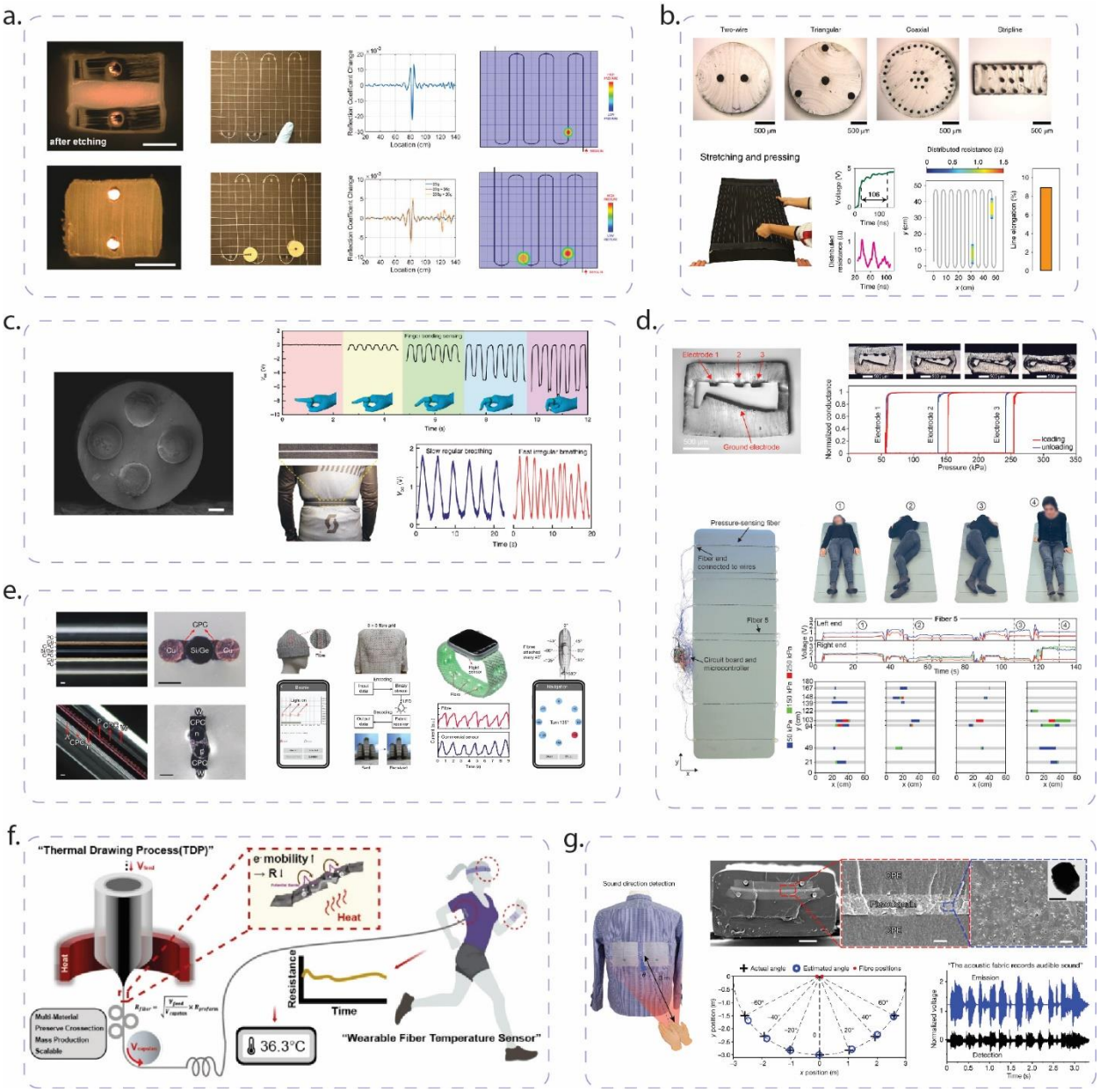

Figure 1.7: **Functional fiber in smart textile and fabric: a.** Using frequency domain reflectometry, pressure points and temperature were measured in the fiber. Reproduced with permission.[176] Copyright 2020, John Wiley and Sons; **b.** Elastomeric fiber with liquid metal used time-domain reflectometry to detect pressure point even during deformation. Reproduced with permission.[177] Copyright 2020, Springer Nature; **c.** Triboelectric fiber to detect motion of finger flexing and breathing. Reproduced with permission.[17] Copyright 2020, Springer Nature; **d.** Electrode contacts in elastomeric fiber measure pressure points on a mat. Reproduced with permission.[178] Copyright 2019, John Wiley and Sons; **e.** Optoelectronic fiber which responds to light enabling light-based communication and photoplethysmography. Reproduced with permission.[24] Copyright 2024, Springer Nature; **f.** Temperature sensing fiber with high sensitivity within the physiological range. Reproduced with permission.[180] Copyright 2023, Springer Nature;

g. Acoustic fiber which can detect sound and operate as a microphone. Reproduced with permission.[13] Copyright 2022, Springer Nature;

1.8 Scope and Organization

Thermally drawn flexible multifunctional fibers hold remarkable potentials in a variety of biomedical application, such as neural probes, chemical sensing, nerve guidance scaffolds, cancer and tumor treatment, soft robotics, and smart textile. However, connecting optical waveguide, microfluidic channel, electrodes (microwires, conductive composites, and liquid metal) to the outside modules, such as laser, drug repository, electronics, and analyzer, can often be challenging.

Specifically, there is a trade-off between the complexity of the functional fiber and the ease of connection. The more densely packed functionalities in the fibers are, the harder it is to successfully connect them all to outside modules. In chapter 2 and chapter 3, I present thermal tapering process and bundling techniques along with the thermal drawing process to fabricate novel multifunctional neural fiber probes. These fiber probes are fabricated smaller (~150μm and 100μm), thereby reducing tissue damage and recording more units compared with the traditional thermally drawn fiber neural probes. Additionally, we reduced the labor-intensive and complicated back-end connections by implementing tapering and bundling.

Another challenge in implantable multifunctional fiber sensors and actuators is the inability sense and actuate along the fiber length. Sensing and actuation usually only happen at the tip of the fiber probe. In chapter 4, I utilized femtosecond laser micromachining techniques to expose electrodes along the length of the thermally drawn functional fiber. This enabled microscale irreversible electroporation (clinically approved tumor treatment) along the side of the fiber with

customizable the size and pattern of the ablated regions. Lastly, chapter 5 concludes the dissertation. I summarize the research achievements in developing thermally drawn neural probes and electroporation device and discuss the future direction and perspectives.

1.9 References

1. Keck, D., Maurer, R. & Schultz, P. On the ultimate lower limit of attenuation in glass optical waveguides. *Applied Physics Letters* **22**, 307-309 (1973).
2. Ramaswami, R., Sivarajan, K. & Sasaki, G. Optical networks: a practical perspective. (Morgan Kaufmann, 2009).
3. Senior, J.M. & Jamro, M.Y. Optical fiber communications: principles and practice. (Pearson Education, 2009).
4. Agrawal, G.P. Fiber-optic communication systems. (John Wiley & Sons, 2012).
5. Marcuse, D. Theory of dielectric optical waveguides. (Elsevier, 2013).
6. Shen, Y. et al. Thermally drawn multifunctional fibers: Toward the next generation of information technology. *InfoMat* **4**, e12318 (2022).
7. Yan, W. et al. Thermally drawn advanced functional fibers: New frontier of flexible electronics. *Materials Today* **35**, 168-194 (2020).
8. Tao, G., Stolyarov, A.M. & Abouraddy, A.F. Multimaterial Fibers. *International Journal of Applied Glass Science* **3**, 349-368 (2012).
9. Yan, W. et al. Advanced Multimaterial Electronic and Optoelectronic Fibers and Textiles. *Advanced Materials* **31**, 1802348 (2019).
10. Loke, G., Yan, W., Khudiyev, T., Noel, G. & Fink, Y. Recent Progress and Perspectives of Thermally Drawn Multimaterial Fiber Electronics. *Advanced Materials* **32**, 1904911 (2020).
11. Banerjee, H. et al. Soft Multimaterial Magnetic Fibers and Textiles. *Advanced Materials* **35**, 2212202 (2023).
12. Egusa, S. et al. Multimaterial piezoelectric fibres. *Nature materials* **9**, 643-648 (2010).
13. Yan, W. et al. Single fibre enables acoustic fabrics via nanometre-scale vibrations. *Nature* **603**, 616-623 (2022).
14. Chocat, N. et al. Piezoelectric fibers for conformal acoustics. *Advanced materials* **24**, 5327 (2012).
15. Wang, S. et al. Flexible Piezoelectric Fibers for Acoustic Sensing and Positioning. *Advanced Electronic Materials* **3**, 1600449 (2017).
16. Feng, Z. et al. Scalable, washable and lightweight triboelectric-energy-generating fibers by the thermal drawing process for industrial loom weaving. *Nano Energy* **74**, 104805 (2020).
17. Dong, C. et al. High-efficiency super-elastic liquid metal based triboelectric fibers and textiles. *Nature Communications* **11**, 3537 (2020).
18. Pan, S. et al. Super-elastic microstructured triboelectric fibers and textiles fabricated by extrusion and thermal drawing for smart-home applications. *Nano Energy* **122**, 109259 (2024).

19. Hasan, M.M. et al. Scalable Fabrication of MXene-PVDF Nanocomposite Triboelectric Fibers via Thermal Drawing. *Small* **19**, 2206107 (2023).
20. Dong, C. et al. 3D stretchable and self-encapsulated multimaterial triboelectric fibers. *Science Advances* **8**, eabo0869.
21. Khudiyev, T. et al. Thermally drawn rechargeable battery fiber enables pervasive power. *Materials Today* **52**, 80-89 (2022).
22. Khudiyev, T. et al. 100 m Long Thermally Drawn Supercapacitor Fibers with Applications to 3D Printing and Textiles. *Advanced Materials* **32**, 2004971 (2020).
23. Bayindir, M. et al. Metal–insulator–semiconductor optoelectronic fibres. *Nature* **431**, 826-829 (2004).
24. Wang, Z. et al. High-quality semiconductor fibres via mechanical design. *Nature* **626**, 72-78 (2024).
25. Tsui, H.C.L. & Healy, N. Recent progress of semiconductor optoelectronic fibers. *Frontiers of Optoelectronics* **14**, 383-398 (2021).
26. Bayindir, M. et al. Integrated fibres for self-monitored optical transport. *Nature Materials* **4**, 820-825 (2005).
27. Abouraddy, A.F. et al. Large-scale optical-field measurements with geometric fibre constructs. *Nature Materials* **5**, 532-536 (2006).
28. Zhang, J., Wang, Z., Wang, Z. & Wei, L. Advanced Multi-Material Optoelectronic Fibers: A Review. *Journal of Lightwave Technology* **39**, 3836-3845 (2021).
29. Soares, M.S. et al. Immunosensing based on optical fiber technology: Recent advances. *Biosensors* **11**, 305 (2021).
30. Pathak, A. & Viphavakit, C. A review on all-optical fiber-based VOC sensors: Heading towards the development of promising technology. *Sensors and Actuators A: Physical* **338**, 113455 (2022).
31. Vaiano, P. et al. Lab on fiber technology for biological sensing applications. *Laser & Photonics Reviews* **10**, 922-961 (2016).
32. Qian, Y., Zhao, Y., Wu, Q.-l. & Yang, Y. Review of salinity measurement technology based on optical fiber sensor. *Sensors and Actuators B: Chemical* **260**, 86-105 (2018).
33. Wang, Z. et al. Designer patterned functional fibers via direct imprinting in thermal drawing. *Nature Communications* **11**, 3842 (2020).
34. Jiang, S. et al. Spatially expandable fiber-based probes as a multifunctional deep brain interface. *Nature Communications* **11**, 6115 (2020).
35. Kim, J. et al. Laser Machined Fiber-Based Microprobe: Application in Microscale Electroporation. *Advanced Fiber Materials* **4**, 859-872 (2022).
36. Park, S. et al. Adaptive and multifunctional hydrogel hybrid probes for long-term sensing and modulation of neural activity. *Nature Communications* **12**, 3435 (2021).
37. Tabet, A. et al. Modular Integration of Hydrogel Neural Interfaces. *ACS Central Science* **7**, 1516-1523 (2021).
38. Sahasrabudhe, A. et al. Multifunctional microelectronic fibers enable wireless modulation of gut and brain neural circuits. *Nature Biotechnology* (2023).
39. Bayindir, M. et al. Kilometer-long ordered nanophotonic devices by preform-to-fiber fabrication. *IEEE Journal of Selected Topics in Quantum Electronics* **12**, 1202-1213 (2006).
40. Abouraddy, A.F. et al. Towards multimaterial multifunctional fibres that see, hear, sense and communicate. *Nature Materials* **6**, 336-347 (2007).

41. Yu, X. et al. Graphene-based smart materials. *Nature Reviews Materials* **2**, 17046 (2017).
42. Su, M. & Song, Y. Printable Smart Materials and Devices: Strategies and Applications. *Chemical Reviews* **122**, 5144-5164 (2022).
43. Callister, W.D. et al. Materials science and engineering: an introduction, Vol. 7. (John wiley & sons New York, 2007).
44. Mittemeijer, E.J. Fundamentals of materials science, Vol. 8. (Springer, 2010).
45. Shackelford, J.F. Materials science for engineers. *Upper Saddle River, New Jersey* (2000).
46. Regis, J.E. et al. Recent Trends and Innovation in Additive Manufacturing of Soft Functional Materials. *Materials (Basel)* **14** (2021).
47. Otsuka, K. & Ren, X. Recent developments in the research of shape memory alloys. *Intermetallics* **7**, 511-528 (1999).
48. Jani, J.M., Leary, M., Subic, A. & Gibson, M.A. A review of shape memory alloy research, applications and opportunities. *Materials & Design (1980-2015)* **56**, 1078-1113 (2014).
49. Liu, W. et al. New trends, strategies and opportunities in thermoelectric materials: A perspective. *Materials Today Physics* **1**, 50-60 (2017).
50. Tressler, J.F., Alkoy, S. & Newnham, R.E. Piezoelectric sensors and sensor materials. *Journal of electroceramics* **2**, 257-272 (1998).
51. Safaei, M., Sodano, H.A. & Anton, S.R. A review of energy harvesting using piezoelectric materials: state-of-the-art a decade later (2008–2018). *Smart materials and structures* **28**, 113001 (2019).
52. Polman, A., Knight, M., Garnett, E.C., Ehrler, B. & Sinke, W.C. Photovoltaic materials: Present efficiencies and future challenges. *Science* **352**, aad4424 (2016).
53. Han, X., Ji, Y. & Yang, Y. Ferroelectric photovoltaic materials and devices. *Advanced Functional Materials* **32**, 2109625 (2022).
54. Rein, M. et al. Diode fibres for fabric-based optical communications. *Nature* **560**, 214-218 (2018).
55. Tettey, F., Parupelli, S.K. & Desai, S. A Review of Biomedical Devices: Classification, Regulatory Guidelines, Human Factors, Software as a Medical Device, and Cybersecurity. *Biomedical Materials & Devices* **2**, 316-341 (2024).
56. Mamo, H.B., Adamiak, M. & Kunwar, A. 3D printed biomedical devices and their applications: A review on state-of-the-art technologies, existing challenges, and future perspectives. *Journal of the Mechanical Behavior of Biomedical Materials* **143**, 105930 (2023).
57. Cianchetti, M., Laschi, C., Menciassi, A. & Dario, P. Biomedical applications of soft robotics. *Nature Reviews Materials* **3**, 143-153 (2018).
58. Wu, Z. et al. Interstitial fluid-based wearable biosensors for minimally invasive healthcare and biomedical applications. *Communications Materials* **5**, 33 (2024).
59. Ratner, B.D. & Bryant, S.J. Biomaterials: where we have been and where we are going. *Annu. Rev. Biomed. Eng.* **6**, 41-75 (2004).
60. Navarro, M., Michiardi, A., Castano, O. & Planell, J. Biomaterials in orthopaedics. *Journal of the royal society interface* **5**, 1137-1158 (2008).
61. Hench, L.L. & Thompson, I. Twenty-first century challenges for biomaterials. *Journal of the Royal Society Interface* **7**, S379-S391 (2010).

62. Yang, Y. & Gao, W. Wearable and flexible electronics for continuous molecular monitoring. *Chemical Society Reviews* **48**, 1465-1491 (2019).
63. Gao, W., Ota, H., Kiriya, D., Takei, K. & Javey, A. Flexible Electronics toward Wearable Sensing. *Accounts of Chemical Research* **52**, 523-533 (2019).
64. Sun, Y. & Rogers, J.A. Inorganic Semiconductors for Flexible Electronics. *Advanced Materials* **19**, 1897-1916 (2007).
65. Yang, E. et al. Bio-based polymers for 3D printing of bioscaffolds. *Polymer Reviews* **58**, 668-687 (2018).
66. Kalkal, A. et al. Recent advances in 3D printing technologies for wearable (bio) sensors. *Additive Manufacturing* **46**, 102088 (2021).
67. Gattass, R.R. & Mazur, E. Femtosecond laser micromachining in transparent materials. *Nature Photonics* **2**, 219-225 (2008).
68. Sugioka, K. et al. Femtosecond laser 3D micromachining: a powerful tool for the fabrication of microfluidic, optofluidic, and electrofluidic devices based on glass. *Lab on a Chip* **14**, 3447-3458 (2014).
69. Ding, J. et al. Electrospun polymer biomaterials. *Progress in Polymer Science* **90**, 1-34 (2019).
70. Zhang, X., Reagan, M.R. & Kaplan, D.L. Electrospun silk biomaterial scaffolds for regenerative medicine. *Advanced drug delivery reviews* **61**, 988-1006 (2009).
71. Soares, R.M.D., Siqueira, N.M., Prabhakaram, M.P. & Ramakrishna, S. Electrospinning and electrospray of bio-based and natural polymers for biomaterials development. *Materials Science and Engineering: C* **92**, 969-982 (2018).
72. Buzsáki, G. Large-scale recording of neuronal ensembles. *Nature Neuroscience* **7**, 446-451 (2004).
73. Li, H., Wang, J. & Fang, Y. Recent developments in multifunctional neural probes for simultaneous neural recording and modulation. *Microsystems & Nanoengineering* **9**, 4 (2023).
74. Neely, R.M., Piech, D.K., Santacruz, S.R., Maharbiz, M.M. & Carmena, J.M. Recent advances in neural dust: towards a neural interface platform. *Current Opinion in Neurobiology* **50**, 64-71 (2018).
75. Buzsáki, G. & Draguhn, A. Neuronal Oscillations in Cortical Networks. *Science* **304**, 1926-1929 (2004).
76. McNaughton, B.L., O'Keefe, J. & Barnes, C.A. The stereotrode: a new technique for simultaneous isolation of several single units in the central nervous system from multiple unit records. *Journal of neuroscience methods* **8**, 391-397 (1983).
77. Jones, K.E., Campbell, P.K. & Normann, R.A. A glass/silicon composite intracortical electrode array. *Annals of biomedical engineering* **20**, 423-437 (1992).
78. Gray, C.M., Maldonado, P.E., Wilson, M. & McNaughton, B. Tetrodes markedly improve the reliability and yield of multiple single-unit isolation from multi-unit recordings in cat striate cortex. *Journal of Neuroscience Methods* **63**, 43-54 (1995).
79. Mokri, Y. et al. Sorting Overlapping Spike Waveforms from Electrode and Tetrode Recordings. *Front Neuroinform* **11**, 53 (2017).
80. Sponheim, C. et al. Longevity and reliability of chronic unit recordings using the Utah, intracortical multi-electrode arrays. *J Neural Eng* **18** (2021).

81. Dong, C. et al. Fluorescence Imaging of Neural Activity, Neurochemical Dynamics, and Drug-Specific Receptor Conformation with Genetically Encoded Sensors. *Annu Rev Neurosci* **45**, 273-294 (2022).
82. Leopold, A.V., Shcherbakova, D.M. & Verkhusha, V.V. Fluorescent Biosensors for Neurotransmission and Neuromodulation: Engineering and Applications. *Frontiers in Cellular Neuroscience* **13** (2019).
83. Emiliani, V. et al. Optogenetics for light control of biological systems. *Nature Reviews Methods Primers* **2**, 55 (2022).
84. Boyden, E.S., Zhang, F., Bamberg, E., Nagel, G. & Deisseroth, K. Millisecond-timescale, genetically targeted optical control of neural activity. *Nature Neuroscience* **8**, 1263-1268 (2005).
85. Zhang, F., Aravanis, A.M., Adamantidis, A., de Lecea, L. & Deisseroth, K. Circuit-breakers: optical technologies for probing neural signals and systems. *Nature Reviews Neuroscience* **8**, 577-581 (2007).
86. Deubner, J., Coulon, P. & Diester, I. Optogenetic approaches to study the mammalian brain. *Current Opinion in Structural Biology* **57**, 157-163 (2019).
87. Zou, L. et al. Self-assembled multifunctional neural probes for precise integration of optogenetics and electrophysiology. *Nature Communications* **12**, 5871 (2021).
88. Kim, K. et al. Artifact-free and high-temporal-resolution in vivo opto-electrophysiology with microLED optoelectrodes. *Nature communications* **11**, 2063 (2020).
89. Rubehn, B., Wolff, S.B., Tovote, P., Lüthi, A. & Stieglitz, T. A polymer-based neural microimplant for optogenetic applications: design and first in vivo study. *Lab on a Chip* **13**, 579-588 (2013).
90. Zhao, Z. et al. Nanoelectronic coating enabled versatile multifunctional neural probes. *Nano letters* **17**, 4588-4595 (2017).
91. Canales, A. et al. Multifunctional fibers for simultaneous optical, electrical and chemical interrogation of neural circuits in vivo. *Nature Biotechnology* **33**, 277-284 (2015).
92. Du, M. et al. Flexible Fiber Probe for Efficient Neural Stimulation and Detection. *Advanced Science* **7**, 2001410 (2020).
93. Park, S. et al. One-step optogenetics with multifunctional flexible polymer fibers. *Nature Neuroscience* **20**, 612-619 (2017).
94. Antonini, M.-J. et al. Customizing MRI-Compatible Multifunctional Neural Interfaces through Fiber Drawing. *Advanced Functional Materials* **31**, 2104857 (2021).
95. Zheng, N. et al. Multifunctional Fiber-Based Optoacoustic Emitter as a Bidirectional Brain Interface. *Advanced Healthcare Materials* **12**, 2300430 (2023).
96. Garwood, I.C. et al. Multifunctional fibers enable modulation of cortical and deep brain activity during cognitive behavior in macaques. *Science Advances* **9**, eadh0974.
97. Kim, J. et al. T-DOpE probes reveal sensitivity of hippocampal oscillations to cannabinoids in behaving mice. *Nature Communications* **15**, 1686 (2024).
98. Du, J. et al. Protons are a neurotransmitter that regulates synaptic plasticity in the lateral amygdala. *Proceedings of the National Academy of Sciences* **111**, 8961-8966 (2014).
99. Lee, J.-Y. et al. Multimodal brain and retinal imaging of dopaminergic degeneration in Parkinson disease. *Nature Reviews Neurology* **18**, 203-220 (2022).
100. Hagihara, H. et al. Decreased Brain pH as a Shared Endophenotype of Psychiatric Disorders. *Neuropsychopharmacology* **43**, 459-468 (2018).

101. Ismail, Z. et al. Psychosis in Alzheimer disease — mechanisms, genetics and therapeutic opportunities. *Nature Reviews Neurology* **18**, 131-144 (2022).
102. Xu, C., Wu, F., Yu, P. & Mao, L. In Vivo Electrochemical Sensors for Neurochemicals: Recent Update. *ACS Sensors* **4**, 3102-3118 (2019).
103. Chefer, V.I., Thompson, A.C., Zapata, A. & Shippenberg, T.S. Overview of brain microdialysis. *Curr Protoc Neurosci* **Chapter 7**, Unit7.1 (2009).
104. Ungerstedt, U. Microdialysis—principles and applications for studies in animals and man. *Journal of internal medicine* **230**, 365-373 (1991).
105. Benveniste, H. & Hüttemeier, P.C. Microdialysis—theory and application. *Progress in neurobiology* **35**, 195-215 (1990).
106. Plock, N. & Kloft, C. Microdialysis—theoretical background and recent implementation in applied life-sciences. *European journal of pharmaceutical sciences* **25**, 1-24 (2005).
107. CHESLER, M. Regulation and Modulation of pH in the Brain. *Physiological Reviews* **83**, 1183-1221 (2003).
108. Soto, E., Ortega-Ramírez, A. & Vega, R. Protons as Messengers of Intercellular Communication in the Nervous System. *Frontiers in Cellular Neuroscience* **12** (2018).
109. Xiong, Z.-Q., Saggau, P. & Stringer, J.L. Activity-dependent intracellular acidification correlates with the duration of seizure activity. *Journal of Neuroscience* **20**, 1290-1296 (2000).
110. Ziemann, A.E. et al. Seizure termination by acidosis depends on ASIC1a. *Nature neuroscience* **11**, 816-822 (2008).
111. Booth, M.A. et al. Fiber-Based Electrochemical Biosensors for Monitoring pH and Transient Neurometabolic Lactate. *Analytical Chemistry* **93**, 6646-6655 (2021).
112. Richard, I., Schyrr, B., Aiassa, S., Carrara, S. & Sorin, F. All-in-Fiber Electrochemical Sensing. *ACS Applied Materials & Interfaces* **13**, 43356-43363 (2021).
113. Guo, Y. et al. Miniature multiplexed label-free pH probe in vivo. *Biosensors and Bioelectronics* **174**, 112870 (2021).
114. Saizaki, T. et al. The Development of Aptamer-Coupled Microelectrode Fiber Sensors (apta-μFS) for Highly Selective Neurochemical Sensing. *Analytical Chemistry* **95**, 6791-6800 (2023).
115. Olson, J.L., Atala, A. & Yoo, J.J. Tissue engineering: current strategies and future directions. *Chonnam Med J* **47**, 1-13 (2011).
116. Li, Y. et al. Tissue Engineering Strategies for Peripheral Nerve Regeneration. *Front Neurol* **12**, 768267 (2021).
117. Kaplan, B. & Levenberg, S. The Role of Biomaterials in Peripheral Nerve and Spinal Cord Injury: A Review. *Int J Mol Sci* **23** (2022).
118. Li, R. et al. Growth factors-based therapeutic strategies and their underlying signaling mechanisms for peripheral nerve regeneration. *Acta Pharmacologica Sinica* **41**, 1289-1300 (2020).
119. Vijayavenkataraman, S. Nerve guide conduits for peripheral nerve injury repair: A review on design, materials and fabrication methods. *Acta Biomaterialia* **106**, 54-69 (2020).
120. Sarker, M., Naghieh, S., McInnes, A.D., Schreyer, D.J. & Chen, X. Strategic Design and Fabrication of Nerve Guidance Conduits for Peripheral Nerve Regeneration. *Biotechnology Journal* **13**, 1700635 (2018).

121. Tuinstra, H.M. et al. Multifunctional, multichannel bridges that deliver neurotrophin encoding lentivirus for regeneration following spinal cord injury. *Biomaterials* **33**, 1618-1626 (2012).
122. Mobini, S., Spearman, B.S., Lacko, C.S. & Schmidt, C.E. Recent advances in strategies for peripheral nerve tissue engineering. *Current Opinion in Biomedical Engineering* **4**, 134-142 (2017).
123. Gong, B. et al. Neural tissue engineering: From bioactive scaffolds and in situ monitoring to regeneration. *Exploration (Beijing)* **2**, 20210035 (2022).
124. Bellamkonda, R.V. Peripheral nerve regeneration: An opinion on channels, scaffolds and anisotropy. *Biomaterials* **27**, 3515-3518 (2006).
125. Shahriari, D. et al. Scalable Fabrication of Porous Microchannel Nerve Guidance Scaffolds with Complex Geometries. *Advanced Materials* **31**, 1902021 (2019).
126. Stokols, S. et al. Templated agarose scaffolds support linear axonal regeneration. *Tissue engineering* **12**, 2777-2787 (2006).
127. Pawar, K. et al. Increasing capillary diameter and the incorporation of gelatin enhance axon outgrowth in alginate-based anisotropic hydrogels. *Acta biomaterialia* **7**, 2826-2834 (2011).
128. Koffler, J. et al. Biomimetic 3D-printed scaffolds for spinal cord injury repair. *Nature medicine* **25**, 263-269 (2019).
129. Koppes, R.A. et al. Thermally drawn fibers as nerve guidance scaffolds. *Biomaterials* **81**, 27-35 (2016).
130. Wang, H. et al. Global, regional, and national life expectancy, all-cause mortality, and cause-specific mortality for 249 causes of death, 1980–2015: a systematic analysis for the Global Burden of Disease Study 2015. *The lancet* **388**, 1459-1544 (2016).
131. Guan, X. Cancer metastases: challenges and opportunities. *Acta Pharmaceutica Sinica B* **5**, 402-418 (2015).
132. Mohammad, R.M. et al. Broad targeting of resistance to apoptosis in cancer. *Seminars in Cancer Biology* **35**, S78-S103 (2015).
133. Bidram, E. et al. A concise review on cancer treatment methods and delivery systems. *Journal of Drug Delivery Science and Technology* **54**, 101350 (2019).
134. Debela, D.T. et al. New approaches and procedures for cancer treatment: Current perspectives. *SAGE Open Med* **9**, 20503121211034366 (2021).
135. Chabner, B.A. & Roberts, T.G. Chemotherapy and the war on cancer. *Nature Reviews Cancer* **5**, 65-72 (2005).
136. Chen, H.H. & Kuo, M.T. Improving radiotherapy in cancer treatment: Promises and challenges. *Oncotarget* **8**, 62742 (2017).
137. Schaue, D. & McBride, W.H. Opportunities and challenges of radiotherapy for treating cancer. *Nature reviews Clinical oncology* **12**, 527-540 (2015).
138. Vogelstein, B. & Kinzler, K.W. Cancer genes and the pathways they control. *Nature medicine* **10**, 789-799 (2004).
139. Debatin, K.-M. Apoptosis pathways in cancer and cancer therapy. *Cancer Immunology, Immunotherapy* **53**, 153-159 (2004).
140. Chin, A.L. et al. Implantable optical fibers for immunotherapeutics delivery and tumor impedance measurement. *Nature Communications* **12**, 5138 (2021).

141. Jiang, C., Davalos, R.V. & Bischof, J.C. A review of basic to clinical studies of irreversible electroporation therapy. *IEEE Transactions on biomedical Engineering* **62**, 4-20 (2014).
142. Scheffer, H.J. et al. Irreversible electroporation for nonthermal tumor ablation in the clinical setting: a systematic review of safety and efficacy. *Journal of Vascular and Interventional Radiology* **25**, 997-1011 (2014).
143. Rubinsky, B., Onik, G. & Mikus, P. Irreversible electroporation: a new ablation modality--clinical implications. *Technol Cancer Res Treat* **6**, 37-48 (2007).
144. Runciman, M., Darzi, A. & Mylonas, G.P. Soft Robotics in Minimally Invasive Surgery. *Soft Robot* **6**, 423-443 (2019).
145. Rich, S.I., Wood, R.J. & Majidi, C. Untethered soft robotics. *Nature Electronics* **1**, 102-112 (2018).
146. Hsiao, J.-H., Chang, J.-Y. & Cheng, C.-M. Soft medical robotics: clinical and biomedical applications, challenges, and future directions. *Advanced Robotics* **33**, 1099-1111 (2019).
147. Leber, A. et al. Highly Integrated Multi-Material Fibers for Soft Robotics. *Advanced Science* **10**, 2204016 (2023).
148. Qiu, Y. et al. Integrated Sensors for Soft Medical Robotics. *Small* **n/a**, 2308805 (2024).
149. Kim, S., Laschi, C. & Trimmer, B. Soft robotics: a bioinspired evolution in robotics. *Trends in Biotechnology* **31**, 287-294 (2013).
150. Manti, M., Cacucciolo, V. & Cianchetti, M. Stiffening in Soft Robotics: A Review of the State of the Art. *IEEE Robotics & Automation Magazine* **23**, 93-106 (2016).
151. Paek, J., Cho, I. & Kim, J. Microrobotic tentacles with spiral bending capability based on shape-engineered elastomeric microtubes. *Scientific reports* **5**, 10768 (2015).
152. Lindenroth, L., Duriez, C., Back, J., Rhode, K. & Liu, H. in 2017 IEEE/RSJ International Conference on Intelligent Robots and Systems (IROS) 2923-2928 (IEEE, 2017).
153. Gul, J.Z., Yang, Y.J., Su, K.Y. & Choi, K.H. Omni directional multimaterial soft cylindrical actuator and its application as a steerable catheter. *Soft robotics* **4**, 224-240 (2017).
154. Kim, Y., Parada, G.A., Liu, S. & Zhao, X. Ferromagnetic soft continuum robots. *Science Robotics* **4**, eaax7329 (2019).
155. Martinez, R.V. et al. Robotic tentacles with three-dimensional mobility based on flexible elastomers. *Advanced materials* (2013).
156. Fusco, S. et al. Shape-Switching Microrobots for Medical Applications: The Influence of Shape in Drug Delivery and Locomotion. *ACS Applied Materials & Interfaces* **7**, 6803-6811 (2015).
157. Whitesides, G.M. Soft Robotics. *Angewandte Chemie International Edition* **57**, 4258-4273 (2018).
158. Schmitt, F., Piccin, O., Barbé, L. & Bayle, B. Soft Robots Manufacturing: A Review. *Frontiers in Robotics and AI* **5** (2018).
159. Gul, J.Z. et al. 3D printing for soft robotics - a review. *Sci Technol Adv Mater* **19**, 243-262 (2018).
160. Zhang, Y. et al. Submillimeter Multifunctional Ferromagnetic Fiber Robots for Navigation, Sensing, and Modulation. *Advanced Healthcare Materials* **12**, 2300964 (2023).
161. Lee, Y. et al. Magnetically Actuated Fiber-Based Soft Robots. *Advanced Materials* **35**, 2301916 (2023).

162. Kanik, M. et al. Strain-programmable fiber-based artificial muscle. *Science* **365**, 145-150 (2019).
163. Sato, Y. & Guo, Y. Shape-Memory-Alloys Enabled Actuatable Fiber Sensors via the Preform-to-Fiber Fabrication. *ACS Applied Engineering Materials* **1**, 822-831 (2023).
164. Yang, W. et al. Single body-coupled fiber enables chipless textile electronics. *Science* **384**, 74-81 (2024).
165. Wicaksono, I. et al. A tailored, electronic textile conformable suit for large-scale spatiotemporal physiological sensing in vivo. *npj Flexible Electronics* **4**, 5 (2020).
166. Choi, S., Lee, H., Ghaffari, R., Hyeon, T. & Kim, D.-H. Recent Advances in Flexible and Stretchable Bio-Electronic Devices Integrated with Nanomaterials. *Advanced Materials* **28**, 4203-4218 (2016).
167. Chen, G. et al. Electronic Textiles for Wearable Point-of-Care Systems. *Chemical Reviews* **122**, 3259-3291 (2022).
168. Stoppa, M. & Chiolerio, A. Wearable electronics and smart textiles: a critical review. *Sensors (Basel)* **14**, 11957-11992 (2014).
169. Zaman, S.u., Tao, X., Cochrane, C. & Koncar, V. Smart E-Textile Systems: A Review for Healthcare Applications. *Electronics* **11**, 99 (2022).
170. Meng, K. et al. A Wireless Textile-Based Sensor System for Self-Powered Personalized Health Care. *Matter* **2**, 896-907 (2020).
171. Khoshnoud, F. & Silva, C.W.d. Recent advances in MEMS sensor technology – biomedical applications. *IEEE Instrumentation & Measurement Magazine* **15**, 8-14 (2012).
172. Meng, K. et al. Wearable Pressure Sensors for Pulse Wave Monitoring. *Advanced Materials* **34**, 2109357 (2022).
173. Zhang, B., Ren, T., Li, H., Chen, B. & Mao, Y. Recent Progress of Nature Materials Based Triboelectric Nanogenerators for Electronic Skins and Human–Machine Interaction. *Advanced Energy and Sustainability Research* **5**, 2300245 (2024).
174. Tian, G. et al. Hierarchical Piezoelectric Composites for Noninvasive Continuous Cardiovascular Monitoring. *Advanced Materials* **n/a**, 2313612 (2024).
175. Deng, Z., Guo, L., Chen, X. & Wu, W. Smart Wearable Systems for Health Monitoring. *Sensors* **23**, 2479 (2023).
176. Yu, L. et al. Flexible Multi-Material Fibers for Distributed Pressure and Temperature Sensing. *Advanced Functional Materials* **30**, 1908915 (2020).
177. Leber, A. et al. Soft and stretchable liquid metal transmission lines as distributed probes of multimodal deformations. *Nature Electronics* **3**, 316-326 (2020).
178. Leber, A. et al. Compressible and Electrically Conducting Fibers for Large-Area Sensing of Pressures. *Advanced Functional Materials* **30**, 1904274 (2020).
179. Reith, J. et al. Body temperature in acute stroke: relation to stroke severity, infarct size, mortality, and outcome. *The Lancet* **347**, 422-425 (1996).
180. Ryu, W.M., Lee, Y., Son, Y., Park, G. & Park, S. Thermally Drawn Multi-material Fibers Based on Polymer Nanocomposite for Continuous Temperature Sensing. *Advanced Fiber Materials* **5**, 1712-1724 (2023).
181. Rufo, J., Zhang, P., Zhong, R., Lee, L.P. & Huang, T.J. A sound approach to advancing healthcare systems: the future of biomedical acoustics. *Nature Communications* **13**, 3459 (2022).

Chapter 2
Tapered Drug delivery, Optical Stimulation, and Electrophysiology (T-DOpE) Probes

2.1 Introduction

Recent advancements in neural interface technology have significantly improved our understanding of the nervous system,[1-10] presenting new opportunities to explore systems-level neurophysiology, the treatment of neurological disorders, and the development of brain-machine interfaces. However, the complexity of the brain's inner workings demands increased precision in the monitoring and manipulation of neural activity in order to decipher and understand its connectivity and dynamics.[1, 11-14] Optogenetics has been developed as a powerful tool to modulate and/or monitor neural activities with a high spatiotemporal resolution and cell-type specificity.[15, 16] It has led to the widespread adoption of bi-directional devices, which are able to monitor electrical activity and apply optical stimulation.[4, 17-20] However, other biological factors such as neurochemistry are intertwined with electrical activity, necessitating simultaneous opto-electro-pharmacological investigations. One such example, is the interaction of exogenous cannabinoids with neural circuitry. With the recent rise in popularity of cannabinoids due to widespread legalization in the United States, this pharmacological-electrophysiological interaction needs to be further investigated. Combining drug infusion with current opto-electric devices has remained challenging. Therefore, developing single devices that can interact with the brain of behaving mammals across such multiple modalities is a critical goal for the field.

A few technologies have been developed aiming to address this challenge,[21, 22] however, the fabrication of these probes is mostly based on cleanroom microfabrication techniques which

are time-consuming and expensive. Here, we develop a probe technology by merging two cutting edge fabrication approaches, i.e., thermal fiber drawing and multi-material tapering. This scalable probe technology opens opportunities for broad distribution of flexible opto-electro-pharmacological probes in the neuroscience community. In addition, a wide selection of new materials, geometrical arrangement, and functionalities can be embedded in these tapered fiber probes.

More specifically, the thermal fiber drawing method has emerged as a promising technique for producing scalable multimodality fiber devices at a low cost since 2015.[23-29] Such fiber devices are fabricated via a method commonly used in industry to produce optical fibers. The macroscale, multi-material preform is heated until softened, and pulled into hundreds of meters of fibers that can be as thin as a human hair. The fast and simple fabrication process utilizing affordable machinery and soft material results in a cheap, sturdy and biocompatible device. However, an inherent challenge of fiber technology lies in the uniform diameter across the length: there is a tradeoff between minimized sensing tip for biocompatibility and maximized backend tip for easy connection. This has limited the fiber's practicality in neuroscience applications. To overcome this challenge, we developed a thermal tapering process (TTP) and a semi-automated connection method, which enable us to fabricate microprobes with high structural and functional complexities and scalability (**fig. 2.1**, left). Using this approach, the connectorization is no longer a limiting factor in our probe design. It is noteworthy that over the past decades, the tapering of silica has enabled significant advancement in the neuroscience field such as glass micropipettes used in patch clamp recording. And more recently, tapered silica fiber was developed for multisite photometry[30] and single neuron recording.[8] In this work, we demonstrated multi-material tapering to create multiplexed, multifunctional neural probes. This Tapered Drug delivery, Optical Stimulation, and

Electrophysiology (T-DOpE) probe allows us to investigate highly complex neural circuitry such as that of the hippocampus in behaving mice performing tasks.

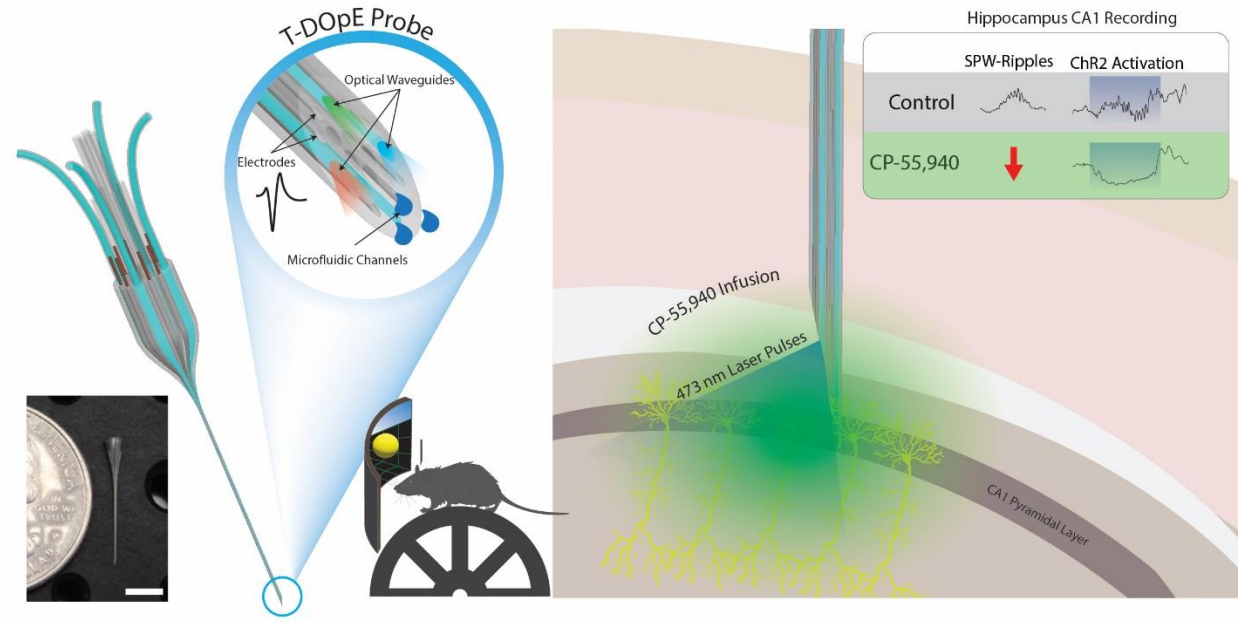

Figure 2.1: T-DOpE probe and CA1 electrophysiological activity in response to local chemical manipulations under natural and optically stimulated conditions. T-DOpE probe offers higher complexities at the sensing tip while easing the connection between the backend and the electronics. The probe is implanted into behaving head-fixed mice expressing channel rhodopsin (ChR2) in pyramidal neurons in hippocampal area CA1. Local infusion of synthetic cannabinoid (CB1 Agonist, CP-55,940) in CA1 is sufficient to abolish both spontaneous and optogenetically induced sharp wave-ripples (SPW-R) (Scale bar: 5mm).

The hippocampus plays a major role in memory including for learned spatial locations.[31, 32] During exploration, hippocampal area CA1 (CA1) pyramidal cell (PYR) activity is organized at the theta timescale (6-11 Hz);[33, 34] during consummatory behaviors and non-rapid eye movement sleep, large depolarization events drive the generation of sharp wave-ripples (SPW-R, 100-250 Hz). Coordinated activity of PYR organized first by theta followed by SPW-R associated replay is thought to support memory consolidation.[35] Further, SPW-Rs are an important electrophysiological marker of learning and memory[36, 37] and causal roles for SPW-Rs in driving specific behaviors have been demonstrated. Behavioral performance is improved when SPW-Rs

are extended in duration;[38] while disruption/truncation of SPW-Rs in both wake and non-rem sleep states decreases performance.[39-42] In rodents, cannabinoid type-1 receptor (CB1-R) activation leads to neuronal populations losing their temporally structed co-activity, thought to cause the disruption of hippocampal synchronous activity including epileptic seizures (high frequency oscillations),[43-46] as well as theta oscillations and SPW-Rs.[47, 48] The cannabinoid induced disruption of theta and SPW-Rs is suggested to be a mechanism behind cannabinoid-associated memory impairment in rodents[47, 49-52] and humans.[53-55] While a mechanism behind seizure disruption has been identified,[56] the relationship between the CB1R and memory-supporting rhythms remains unclear. It is believed cannabinoids act through CB1R to impair memory by changing the spiking activity of neurons, either through acting directly on cells expressing CB1R in CA1, or indirectly by acting on presynaptic partners.[52, 57-62] Thus, the precise mechanisms by which CB1R agonists impair hippocampal rhythms have yet to be identified.

Theta and SPW-R oscillations require independent mechanisms of generation,[33-35, 37, 63] and CB1R expression widely varies across cell types and brain areas,[51, 58-60, 64, 65] further complicating our understanding of specific cellular/synaptic loci at which cannabinoid signaling occurs. Among CA1 neurons, CB1 receptors are expressed on the axon terminals of by CCK+ basket cells, which act to suppress neurotransmitter release,[58, 59, 66] and on pyramidal cell dendrites, decreasing excitability.[67] The theta oscillation in CA1 is strongly supported by inputs from the medial septum,[33, 63] where CB1Rs are widely expressed including on axon terminals projecting to CA1.[64] Systemic infusion of CB1 agonists disrupts the theta oscillation and organization of spike timing,[47, 48] but because this method activates CB1Rs throughout the body and brain it is unable to identify mechanistic loci. Thus, it is currently unclear if the activation of CB1Rs within the medial septum, within CA1, or on projections from the medial septum are responsible for theta disruption. The

SPW-R oscillation is generated by the reciprocal interaction of excitatory pyramidal cells and local inhibitory interneurons in CA1,[68-71] initiated by strong excitatory input from Schaffer collaterals originating in CA3,[35, 37] whose terminals express CB1 receptors.[60-62] SPW-Rs can also be generated experimentally by depolarizing CA1 excitatory neurons.[68] The cellular-synaptic mechanisms by which cannabinoids disrupt SPW-Rs have remained enigmatic in large part due to the challenging nature of monitoring and manipulating neuronal activity with pharmacological interventions in microcircuits of behaving animals, which our probes robustly support. Specifically our devices are able to deliver the synthetic cannabinoid CP-55,940, a validated tool to study the effect of CB1R activation on neuronal activity,[47-49, 52] to a local circuit which we monitor with electrophysiology and manipulate further with optogenetics.

Here, we present the Thermal Tapering Process (TTP) which enables high feature density, functional complexity, and semi-automated backend connections. Various designs of the probe were fabricated to demonstrate the capabilities achievable with the tapering method. To test our device performance *in vivo*, T-DOpE probes were implanted in awake, behaving mice. We demonstrate that T-DOpE probes can reliably record hippocampal circuit electrophysiology in both acute and chronic platforms. We then demonstrated precisely controlled optical and chemical modulation of neural activity using our probes in CA1. We use our device to test the hypothesis that activation of CB1 receptors in CA1 weakens the theta oscillation during exploration. Additionally, we tested if activating CB1 receptors expressed by CA1 neurons is sufficient to disrupt SPW-Rs. We found that intra-CA1 administration of CP-55,940 during head-fixed navigation was sufficient to reduce theta oscillations and abolish spontaneous SPW-Rs. Interestingly, we discovered that the local infusion of CP-55,940 in CA1 of a mouse expressing channel rhodopsin (ChR2) in CA1 pyramidal cells inhibits optogenetically induced SPW-Rs (**fig.**

2.1, right). For the first time, we used a single device with unique multi-modal capabilities, to examine the effects of CA1 cannabinoid receptor activation on local oscillatory activity. We found that regardless of CA3 inputs, CB1R agonism disrupts SPW-R generation, emphasizing the importance of cannabinoid signaling for local circuit computation.

2.2 Results

2.2.1 T-DOpE Probe fabricated using Thermal Tapering Process

Multifunctional tapered probes with various designs were fabricated via the thermal drawing process (TDP) followed by a thermal tapering process (TTP). **Fig. 2.2a** shows the fabrication steps for a preform. A Polycarbonate (PC) rod was machined to create hollow channels (microfluidic channels in the finished device), and spaces to inlay waveguides and electrodes. Waveguides with PC core (refractive index n =1.586) and Poly(methyl 2-methylpropenoate) (PMMA; refractive index n = 1.49) cladding and bismuth tin (BiSn) alloy electrodes were then inserted into their respective positions. The preform was then wrapped in PC film and consolidated in a vacuum furnace. Through TDP, the finalized preform was heated and drawn down to a 2mm diameter fiber (**fig. 2.2b**). The fiber diameter was closely monitored via a laser micrometer and controlled by adjusting the pulling speed and temperature. The fiber was cut into 10cm long mini-preforms (~ one hundred per TDP draw) for the subsequent thermal tapering process (TTP). During TTP, mini-preforms are heated, softened and pulled to form a tapered structure (**fig. 2.2c**). The process is adapted from the fabrication method of heating glass pipettes and tapered silica optical fibers.[72] Here, instead of using a single material (silica) as in the traditional tapering approaches, we develop a multi-material thermal tapering approach to co-draw multiple functional components inside a polymer matrix. The pulled structure was then cut at a specific angle, resulting in two

individual microprobes with 2mm diameter backends and 150µm tapered tips for monitoring and manipulating neural activity.

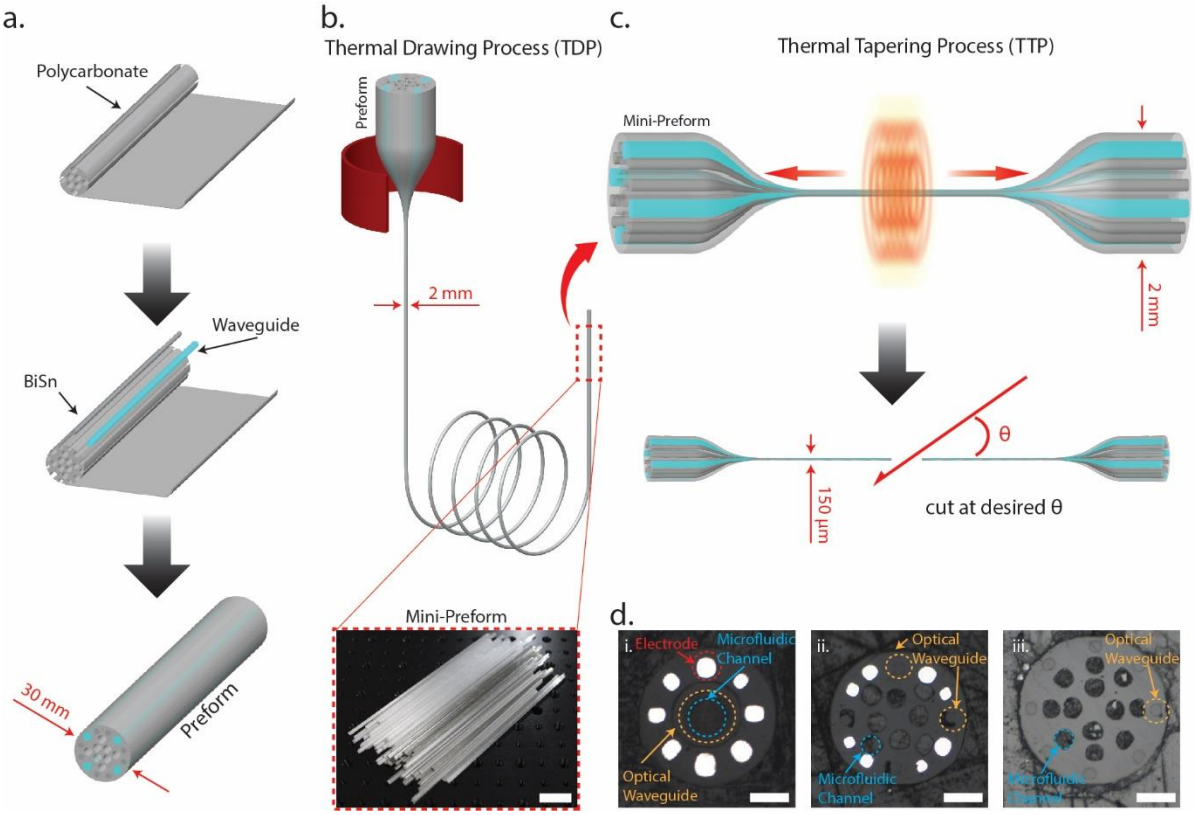

Figure 8.2: T-DOpE Probe fabricated using Thermal Tapering Process. **a.** Schematic of the preform fabrication. **b.** Thermal drawing process pulling 30mm diameter preform into 2mm diameter fibers. The fibers are dissected into 10cm long mini-preforms for tapering (Scale bar: 2cm) **c.** Illustration of the thermal tapering process of mini preform. Similar to glass pipette pulling, the mini preform is heated until softened, pulled and cut at a desired angle, resulting in two individual probes. **d.** Cross-sectional images of the three various designs. **(i)** eight electrodes, one microfluidic channel, and one optical waveguide. **(ii)** Eight electrodes, eight microfluidic channels, and four optical waveguides. **(iii)** Twelve microfluidic channels and eight optical waveguides. (Scale bar: 50µm)

By varying the temperature and the pulling speed thicker (200 µm in diameter) or thinner tapered fiber (50 µm in diameter) can be achieved, as shown in **supplementary fig. 2.1**. To meet the impedance requirement for high-quality neural recording, the electrodes were designed to be at least 25 µm in diameter. Drug delivery channels can be as small as 20 µm without collapsing (**Supplementary fig. 2.2**). However, the pressure required to push fluid through a microfluidic

channel is proportional to the channel radius^4 and fluid viscosity. For this study in which we delivered vehicle and CP-55,940 which has a high viscosity, we chose drug channels with a diameter of ~40 µm to ensure stable and reliable drug delivery. For this study, three different probe designs (8/1/1, 8/4/8 and 0/8/12; electrodes/waveguides/microfluidic channels, respectively) were fabricated. The size of the electrodes, microfluidic channels, and optical waveguides are ~25 µm, 30-50 µm, and 30 µm respectively. Their device tip cross sections are shown in **fig. 2.2d**. The BiSn electrodes record extracellular voltage while the optical waveguides control optogenetics, and the microfluidic channels enable focal drug infusion.

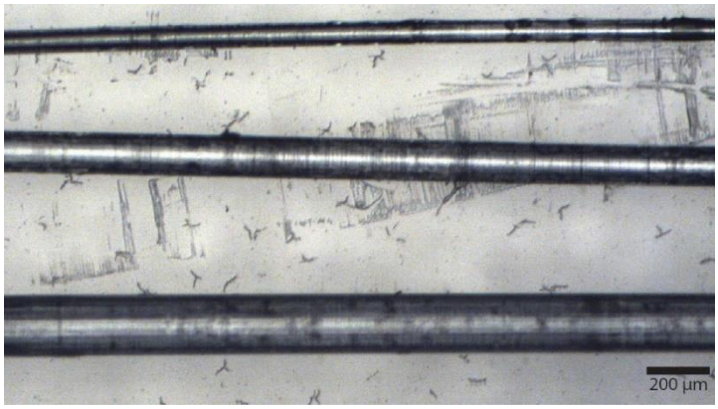

Supplementary Figure 2.1: Microscope image of three various thickness of fiber achieved with thermal tapering.

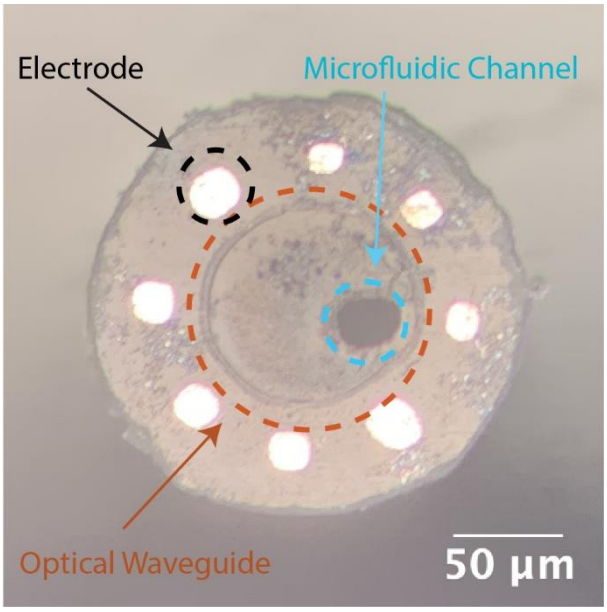

Supplementary Figure 2.2: Cross section of a probe design with 20 µm microfluidic channel.

2.2.2 T-DOpE probe connections and characterizations

We developed the fast, semi-automated backend connection method to replace the traditional method which is slow and labor-intensive. Our connection to the T-DOpE probe was executed exclusively on its 2mm backend (**fig. 2.3a**). Electrical connection was accomplished by heating the probe's backend and inserting insulated copper wires into melted electrodes. The probe was then cooled for the BiSn electrodes to solidify. The microfluidic connection was achieved by inserting a custom drawn thin PC tube into the microfluidic channels. Custom drawn polymer optical fibers were coupled onto the waveguides on the probe's backend. UV epoxy was then used to seal and fix the microfluidic and optical connections in place. A fully functional and connectorized probe with 8 electrodes, 4 waveguides and 8 microfluidic channels is shown in **fig. 2.3b.** Probes are fitted with industry standard adapters compatible with electrophysiology

equipment, optical modules, and drug delivery pumps. A photograph of a probe connected to a printed circuit board (PCB) is shown in **supplementary fig. 2.3**.

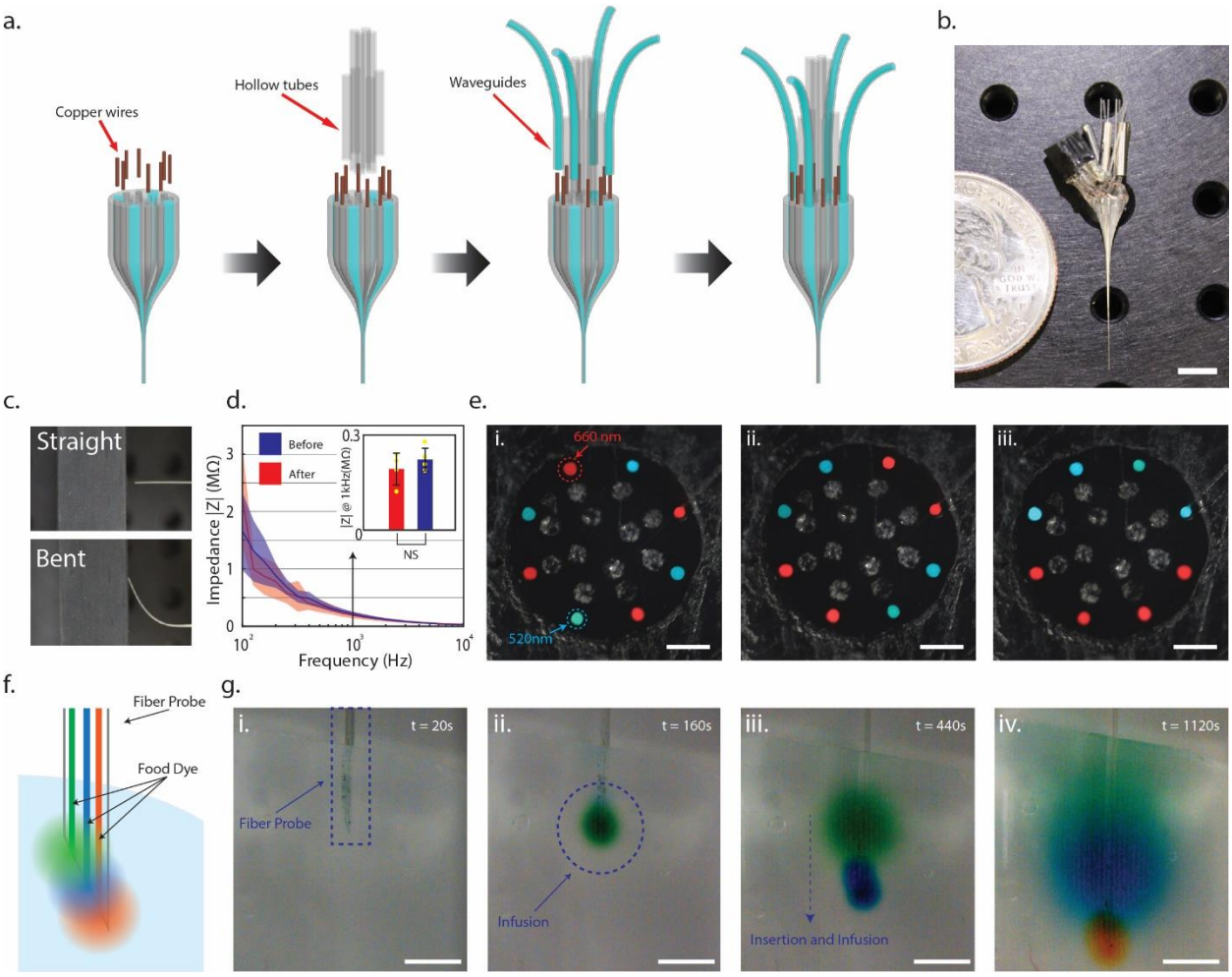

Figure 2.9: T-DOpE probe connections and characterizations. **a.** Schematic of the T-DOpE probe backend connection process. **b.** Photograph of a fully connected probe with eight electrodes, eight microfluidic channels, and four optical waveguides. (Scale bar: 5mm) **c.** Photograph of a straight probe and a probe bent roughly 45° to demonstrate the flexibility at the sensing end. **d.** Impedance measurements of the BiSn electrodes before and after bending. All error bars and shaded colors represent the standard deviation. (Student's two-tailed t-test, NS: not significant, $p>0.05$(After vs. Before, $p=0.3717$, electrode numbers=8)). Data are presented as mean ± SD. **e.** Cross-sectional images to illustrate the individual addressability of the optical waveguides. (Scale bar: 50µm) **f.** Cartoon of green, blue, and orange food dye independently injected via the probe into a brain phantom. **g.** Time-lapsed images to demonstrate the drug infusion in a 0.6% agarose gel. The inserted probe demonstrates the infusion of three different dyes at three different heights in the phantom. (Scale bar: 1mm)

To demonstrate the flexibility and durability of the probe, we bent the probe at a >45° by applying axial force pressing the tip on a hard surface as shown in **fig. 2.3c**. A video of a tapered probe bending is also available in **supplementary video 2.1**. We measured the spectral impedance of the T-DOpE probe before and after bending. As shown in fig. 3d, bending has no statistical impact on our device's impedance at 1 kHz, with an average impedance of 192 ± 50 kΩ before bending and 220 ± 30 kΩ after bending. (Paired t-test, NS: not significant, $p>0.05$ (After vs. Before, $p=0.3717$, $n=8$). Using a dynamic mechanical analyzer, we measured the bending stiffness of the three designs and stainless steel wire, included in **supplementary fig. 2.4**. Note that all designs have a much lower stiffness than the stainless steel wire with the same diameter. Additionally, the elongation to fracture of polycarbonate is 110%, which means, unlike some polymers that shatter like glass, such as acrylic, polycarbonate can undergo large deformation without breaking or cracking. We also demonstrated our optical waveguide's individual addressability in our device with 8 waveguides and 12 microfluidic channels. The cross-sectional images of the device with red and green lights emitting from the waveguides are shown in **fig. 2.3e**. The transmission spectrum of the optical waveguide is included in the **supplementary fig. 2.5**. To test our device's ability to deliver multiple drugs independently via separate microfluidic channels, we conducted an experiment with a device of the same design in 0.6% agarose gel as illustrated in **fig. 2.3f**. The device was first inserted in the agarose gel and delivered green food dye (**fig. 2.3g**). The blue and orange dye were infused after insertion into deeper regions of the gel. The diffusion of the dyes clearly indicated the infused regions of the agarose gel. The video of this experiment is available in **supplementary video 2.2**. These measurements and tests verify the functionality of our probe for extracellular recording, optogenetic manipulation, and drug delivery.

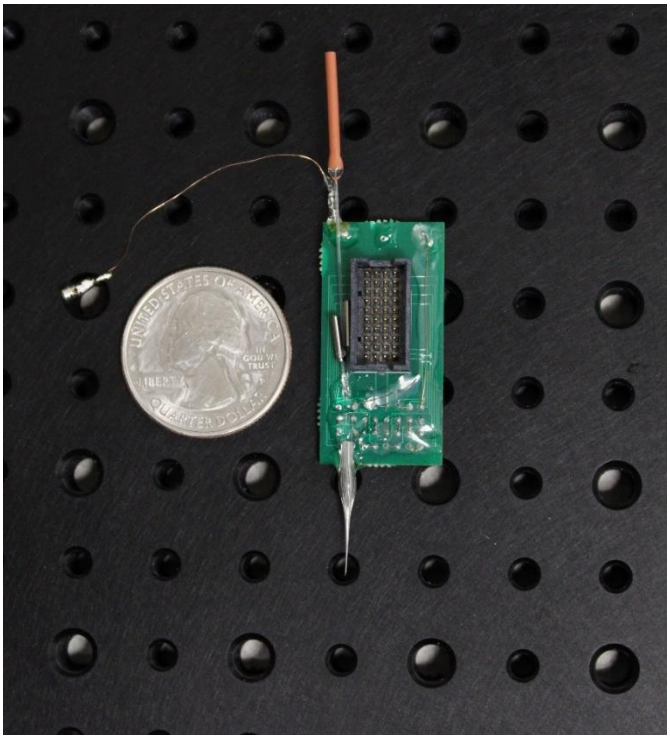

Supplementary Figure 3: Photograph of T-DOpE probe connected to PCB, ferrules, and microfluidic tube. T-DOpE probe connected to PCB was mainly used to monitor and manipulate CA1 circuitry acutely in behaving mice.

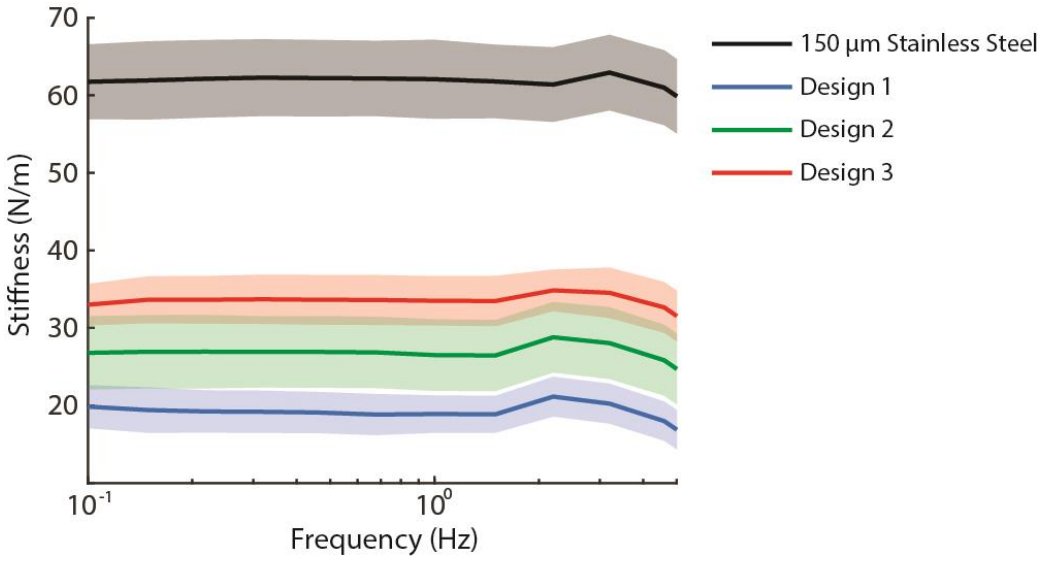

Supplementary Figure 4: Stiffness vs Frequency measurement using a dynamic mechanical analyzer. (n=4 for each designs)

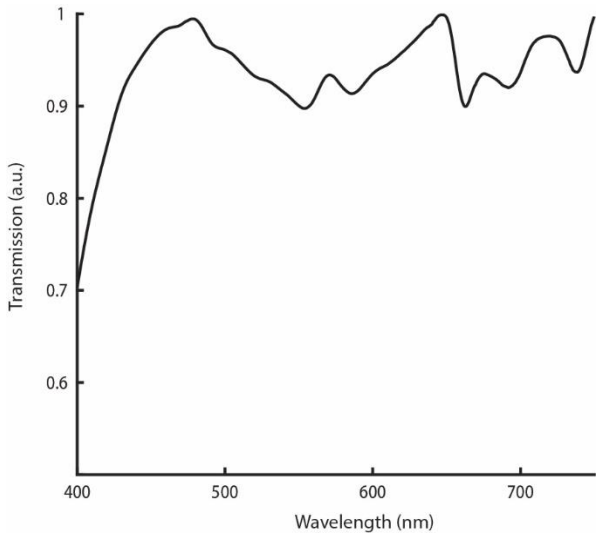

Supplementary Figure 5: Transmission Spectrum of the optical waveguide

2.2.3 *In vivo* electrophysiology recording capabilities of T-DOpE probe

To evaluate the functionalities of the T-DOpE probe *in vivo*, we collected acute and chronic electrophysiological activity in behaving mice. As shown in **fig. 2.4a**, probe implantation was targeted to the CA1 region of the hippocampus. **Fig. 2.4b** shows an example of an acute wideband (0.1 – 8000 Hz) extracellular trace from CA1, which demonstrates a transition from rest, when SPW-Rs occur, to a running state, when theta oscillations emerge. Shaded region **i**. demonstrates multi-unit activity in the raw trace (i.e., bandpass filtered at 0.1-8000 Hz). Shaded regions **ii**. and **iii**. indicate oscillations which are established as identifying electrophysiological landmarks of hippocampus CA1[36, 37, 73]: SPW-Rs (**ii**., 100-250 Hz), and theta-nested gamma oscillations (**iii**., Theta: 6-11 Hz, Gamma: 40-80 Hz)[33, 34]. T-DOpE probes can thus acquire single units and local field potential (LFP) activity in behaving animals without disrupting natural physiological process within the local circuit.

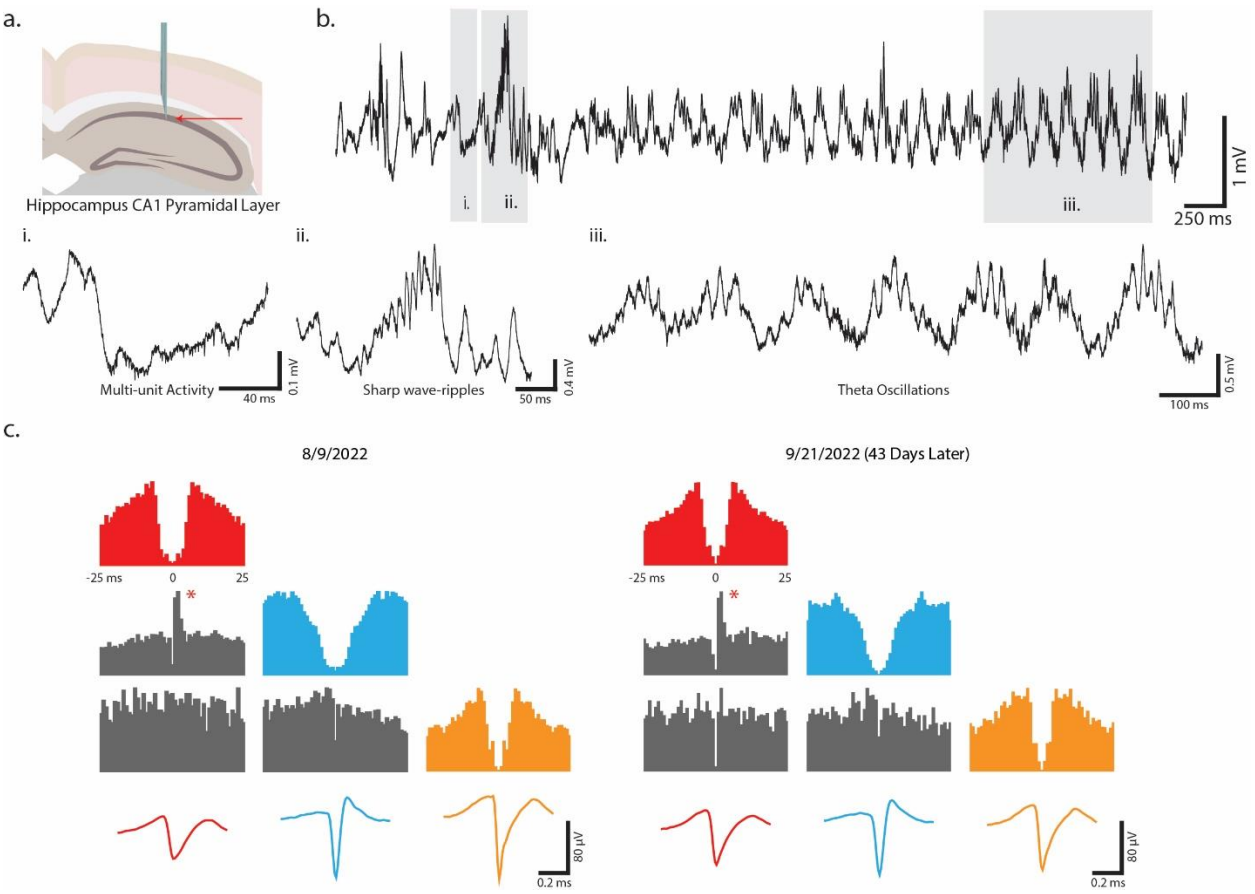

Figure 10: *In vivo* electrophysiology recording capabilities of T-DOpE probe. a. Schematic of the targeted implanted site, hippocampus CA1. **b.** Example wideband (0.1 – 8000 Hz) extracellular traces obtained from CA1. **(i)** Enlarged trace to display multi-unit activity. **(ii)** An example trace of a sharp wave-ripple (100-250 Hz) above the pyramidal layer. **(iii)** An example of theta-nested gamma oscillations (6-11 Hz; 40-80 Hz). **c.** Three example cells recorded on 8/9 and 9/21. Each cell is color coded to match the auto-correlations and the spike waveforms. *Peak in cross-correlation across the red and blue cells suggest their excitatory monosynaptic connection is maintained over 43 days.

We additionally chronically implanted the T-DOpE probes in CA1 (n=2 animals) to demonstrate biocompatibility and ability for long-term stable recording single unit recording capability. Three example putative neurons (i.e., single units) were identified from recordings on 8/9 and 9/21. Each cell is color coded to match the auto-correlations and the spike waveforms across days. The average waveforms recorded from each electrode are included in **supplementary fig. 2.6**. The neurons can be classified by the shape of the waveform and autocorrelation[74] (putative ID, red: pyramidal cell, blue: interneuron, and orange: pyramidal cell). The waveforms from each

electrode and the auto- and cross- correlation suggest that the probe recorded from the same group of neurons across 43 days. Additionally, the peak in the cross-correlation from the red and blue cells (**fig. 2.4c***) shows a monosynaptic connection where the red unit is driving the blue unit to fire action potentials[75, 76]. The observation that this monosynaptic connection maintained across 43 days further supports that fact that the probe can reliably record from the same population of neurons over at least one month, a common goal in modern probe designs[3, 4, 77]. Sorted units and their cluster qualities, such as L-ratio and isolation distance, over all the acute sessions are included in **supplementary table 2.1**. Though multi-unit activity (MUA) and power in the spike frequency band is observed in all recordings, we used Kilosort and manual curation using Phy to detect sortable units in 13 out of 19 acute sessions (n=15 animals). Detected units ranged from 1-7 units (median = 3) with 57.9% of units identified as putative pyramidal cells, and 42.1% as putative interneurons. Validated spike sorting metrics[74] of Isolation Distance (μ=26.9, σ=9.7), and percentage of spikes that violate the inter-spike interval (<2ms, μ=0.53%, σ=0.61%) are reported. These data demonstrate that our T-DOpE probe has sufficient biocompatibility and stability to perform longitudinal experiments without disrupting local circuitry.

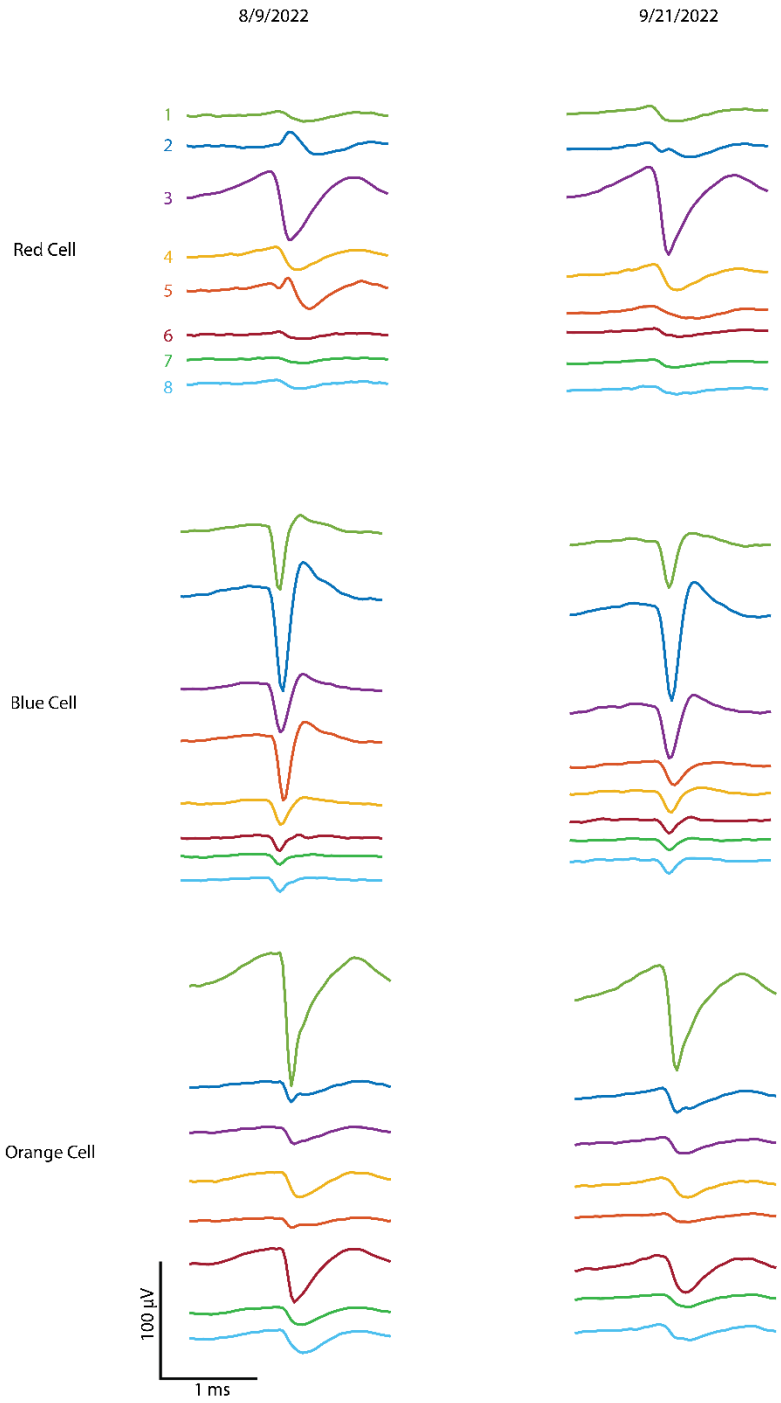

Supplementary Figure 2.6: Average waveform of identified cells in fig. 4c from each electrode. Red and blue cell maintained its monosynaptic connection over 43 days. The electrode number is color-coded and is not correlated with the location of the recording site.

Treatment Group	Mouse ID	Session ID	# of Units	Putative Cell type	Isolation Distance	% ISI Violation
Saline	m449	m449_230921	3 units	PYR	26.3	0.12
				INT	21.0	0.09
				INT	27.6	0.01
	m450	m450_230921	1 unit	INT	28.2	0.27
	m451	m451_230922	1 unit	INT	38.4	0.03
	m452	m452_290922	1 unit	PYR	19.0	3.31
Drug Vehicle	m400	m400_221219	MUA only			
	m401	m401_221224	MUA only			
	m402	m402_221209	5 units	PYR	18.7	0.51
				PYR	25.9	0.21
				PYR	26.6	2.04
				PYR	14.4	0.72
				INT	28.7	0.24
		m402_221212	2 units	PYR	23.8	0.30
				INT	22.9	1.45
	m441	m441_231002	1 unit	PYR	21.5	2.16
	m442	m442_231006	1 unit	PYR	18.7	0.15
CP-55,940	m402	m402_220926	3 units	PYR	44.1	0.01
				PYR	4.9	0.62
				INT	1.01	0.95
	m403	m403_221011	3 units	PYR	33.2	0.21
				INT	35.0	1.82
				INT	38.7	0.47
	m404	m404_221018	MUA only			
	m441	m441_231005	MUA only			
	m442	m442_231010	7 units	PYR	30.8	0.41
				PYR	26.2	0.12
				PYR	31.6	0.01
				PYR	30.4	0.36
				PYR	23.1	0.46
				INT	40.8	0.01
				INT	41.5	0.06
CP-55,940 & ChR2+	m406	m406_230201	3 units	PYR	27.1	1.44
				INT	29.9	0.18
				INT	31.4	0.11
	m432	m432_231019	MUA only			
	m433	m433_231013	7 units	PYR	21.8	0.18
				PYR	25.9	0.18
				PYR	17.5	0.31
				PYR	21.5	0.99
				INT	22.4	0.12
				INT	36.1	0.05
				INT	42.4	0.25
	m435	m435_231016	MUA only			

Supplementary Table 2.1: Sorted units and their cluster qualities over all acute sessions

2.2.4 *In vivo* modulation capabilities of T-DOpE probe: optogenetic and drug infusion

To validate the optical waveguides in our T-DOpE probe, we recorded from CA1 in mice with ChR2 expression restricted to CA1 pyramidal neurons. In these experiments, the probe is advanced until the four most ventral electrodes are ~100 μm above the center of the CA1 pyramidal layer, with the four most dorsal electrodes remaining in overlying cortex. **Fig. 2.5a** shows a representative optically evoked neural response from three levels of optical stimulation intensity (i,e., laser power). By regulating optical stimulation power, we were able to modulate individual unit spike rate (**fig. 2.5b**)**.** Note that the lowest optical power does not elicit action potentials, while middle and high level of optical power increase the firing rate. **Fig. 2.5c** presents examples of local field potential responses to three optical levels. No optically induced responses were observed in cortex, as expected because ChR2 expression was localized to CA1. In CA1, optical stimulation induced large negative deflections in the LFP, likely due to cation influx through ChR2 and active membrane conductances in the ChR2 expressing neurons, as well as synaptically evoked inward currents in postsynaptic neurons activated by glutamate release from the ChR2+ cells. Optogenetic activation of CA1 pyramidal cells (PYRs) induced local high frequency ripple-frequency oscillations in CA1[68]. **Fig. 2.5c*** indicates a SPW-R event endogenously occurring between optical stimulations. These findings demonstrate the probe's ability to monitor and manipulate local circuits while preserving physiological functions of the local circuit.

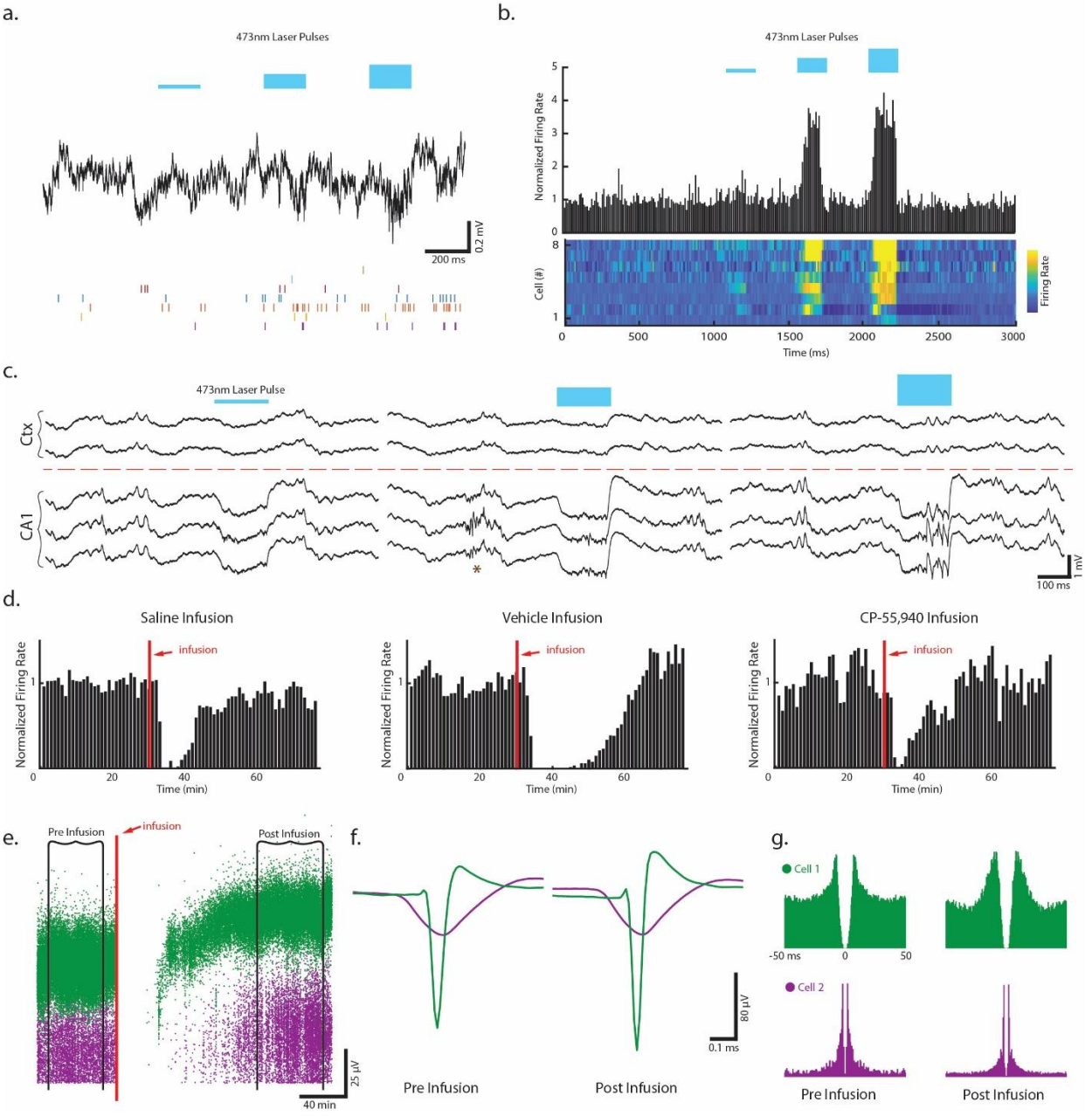

Figure 2.11: *In vivo* modulation capabilities of T-DOpE probe: optogenetic and drug infusion. **a.** Example trace of wideband extracellular response to optical stimulation. **b.** The firing rate of sorted cells during optical stimulation and the normalized firing rate across all sessions. **c.** Examples of optically evoked responses with three levels of laser power (units). No response was observed in the cortex due to AAV-ChR2 expression localized to CA1. The amount of optically evoked neuron activity can be increased by varying the light output, allowing us to achieve optically induced SPW-Rs at higher laser powers. * shows spontaneous SPW-Rs in between optical stimulations. **d.** Normalized firing rate of sorted cells in saline, vehicle, and drug+vehicle infusion. Note shortly after the infusion, the firing rate of all cells drastically decrease not due to pharmacological influence but to the physical displacement of the cells from the recording sites. **e.** Spike amplitude of an interneuron and a pyramidal cell to demonstrate the recovery after infusion

(200nL; 1nL s^{-1}). Given the device tip contains both the microfluidic channel and recording sites (< 20 μm in distance), the cells are pushed away and return after some period of time. **f.** Average spike waveforms of the two cells before and after infusion. **g.** Autocorrelation of the two cells before and after infusion.

There is a general problem in drug infusion into the brain in that tissue is displaced, which is especially noticeable when combined with single unit electrophysiology. To validate that the transient silencing of cells is a result of the physical cell displacement[72, 78, 79] instead of pharmacological influence, we performed a detailed comparison of the dynamic spike recording during the infusion of saline, vehicle, and drug with vehicle. We observed transient absences of spikes after infusion of either saline, vehicle, or drug+vehicle (**fig. 2.5d**, **supplementary fig. 2.7**). **Fig. 2.5e**, shows an example session where we infused 200 nL at 1nLs^{-1} infusion rate, and recording one putative pyramidal cell (purple) and interneuron (green). After the displaced tissue relaxed to its original position spikes were once again able to be detected, at the level of single both sorted cells (**fig. 2.5e**, post-infusion) and multi-unit activity (data not shown). **Fig. 2.5f,g** shows the spike waveforms and autocorrelations of the two cells before and after infusion. The similarities in their waveforms and auto-correlations suggest that these are the same interneuron and pyramidal cell. Importantly, small changes in waveform shape are likely due to the displacement and return of the tissue to the same location with some spatial jitter and thus a change in the effective resistance through the Ohmic brain tissue. However, this jitter is likely in the range of tens not hundreds of microns, explaining the similarity in baseline and recovery spikes. Of note, this is a major improvement over experimental designs which require drug infusion distant from recording sites, making the locus of effect difficult to interpret.

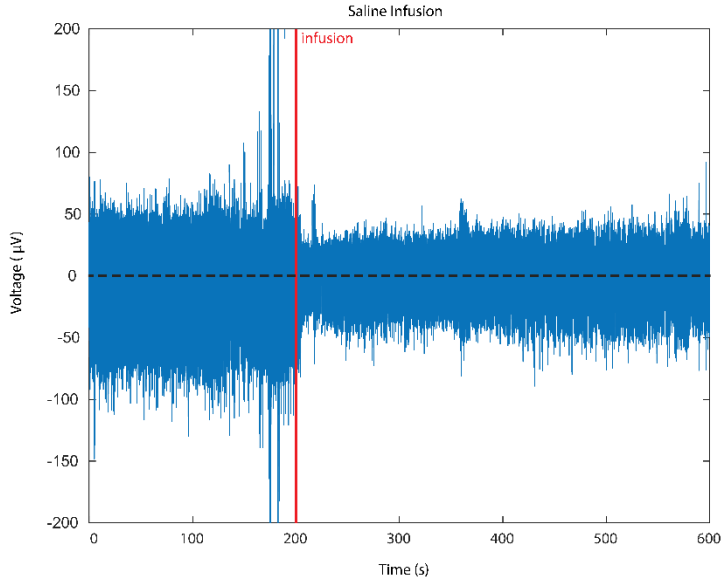
Saline Infusion
infusion
Voltage (μV)
Time (s)
200
150
100
50
0
-50
-100
-150
-200
0
100
200
300
400
500
600

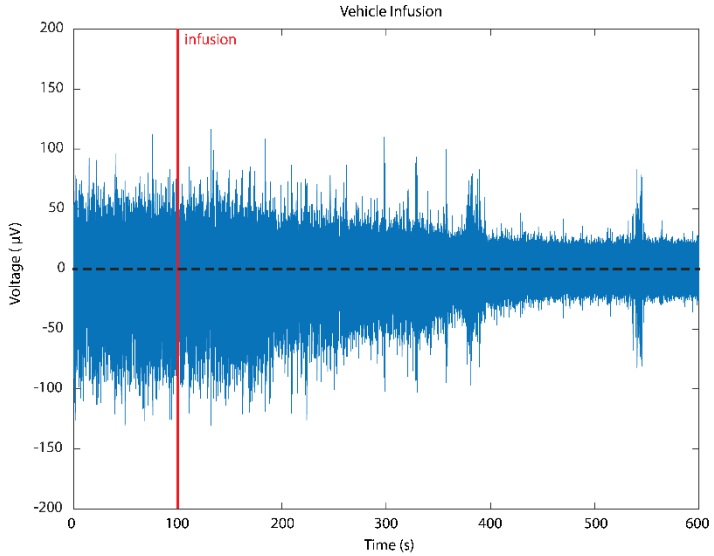
Vehicle Infusion
infusion
Voltage (μV)
Time (s)
200
150
100
50
0
-50
-100
-150
-200
0
100
200
300
400
500
600

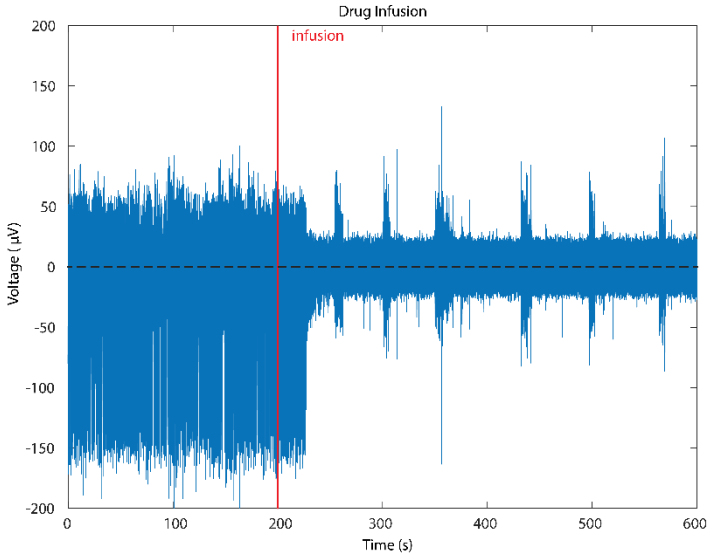
Drug Infusion
infusion
Voltage (μV)
Time (s)
200
150
100
50
0
-50
-100
-150
-200
0
100
200
300
400
500
600

Supplementary Figure 2.7: 10-minute single-unit resolution extracellular trace (600- 8000Hz) where the cells are inevitably displaced due to infusion (200nL, $1nLs^{-1}$). Before infusion, the multi-unit activities were recorded with T-DOpE probe. For all infusion (saline, vehicle, and drug), the neurons are pushed away, and the action potentials of these neurons cannot be recorded until the diffusion has finished. The symmetric noise are the muscle artifacts from the mice.

2.2.5 CA1 theta power reduced activation of CB1Rs in CA1

To examine the role of CB1R in hippocampal CA1 activity during behavior, we used the T-DOpE probe to focally infuse CB1R agonist, CP-55,940, in CA1 while simultaneously monitoring neural activity (animal number = 6 awake head fixed mice). **Fig. 2.6a** displays an illustration of the experimental setup. Head-fixed mice ran on a vertical wheel driving a 1-D visual virtual reality environment that reliably promotes natural (i.e. spontaneous not due to training) running behavior. **Fig. 2.6b** shows a representative session of CP-55,940 infusion (16.8ng; 200nL; $1nLs^{-1}$) following one-hour recording of baseline (**fig. 2.6b,c** is from one CP-55,940 session). The speed of the mouse is shown above the spectrogram of the session. While mice run assemblies of place cells are dynamically synchronized with the theta oscillation (6~11 Hz). The speed data is used to determine the running epochs of the mice, and to demonstrate that mice continue running following infusion. The average normalized speed of each session is shown in **supplementary table 2.2**. The local infusion of CP-55,940 was sufficient to lower the power of theta oscillations in the LFP (calculated from data restricted to running epochs (**fig. 2.6b**)). The representative power spectrum of baseline (Before infusion; duration: 60 minutes) and after drug infusion (one hour after infusion; duration: 60 minutes) are shown in **fig. 2.6c**. Note the peak at 8 Hz decreased by ~20%. **Fig. 2.6d** shows an example control session with drug vehicle (VEH), the normalized spectrum of the baseline and after VEH infusion. The comparison between baseline and VEH shows no significance while the comparison between the baseline and CP-55,940 showed significant difference (Paired t-test, NS: not significant $p \geq 0.05$, * $p \leq 0.05$(Baseline vs. VEH,

p=0.2737, animal number=5), (Baseline vs. CP-55,940, p=0.0026, animal number=5)) (**Fig. 2.6e**). Across all sessions, theta power significantly decreased following CP-55,940 infusion compared to vehicle control (n=5 animals for both VEH, and CP-55,940), with no changes in time spent running or average running speed following infusion (**Supplementary table 2.2**). These findings demonstrate that focal CA1, as opposed to systemic[47], agonism of CB1Rs is sufficient to reduce theta oscillations in CA1. These findings also suggest cannabinoids can impair hippocampal oscillations by acting upon only CB1Rs expressed in CA1 (terminals of inputs from the medial septum and Schaffer Collateral from CA3, or local CA1 neurons), without acting on those in other brain areas.

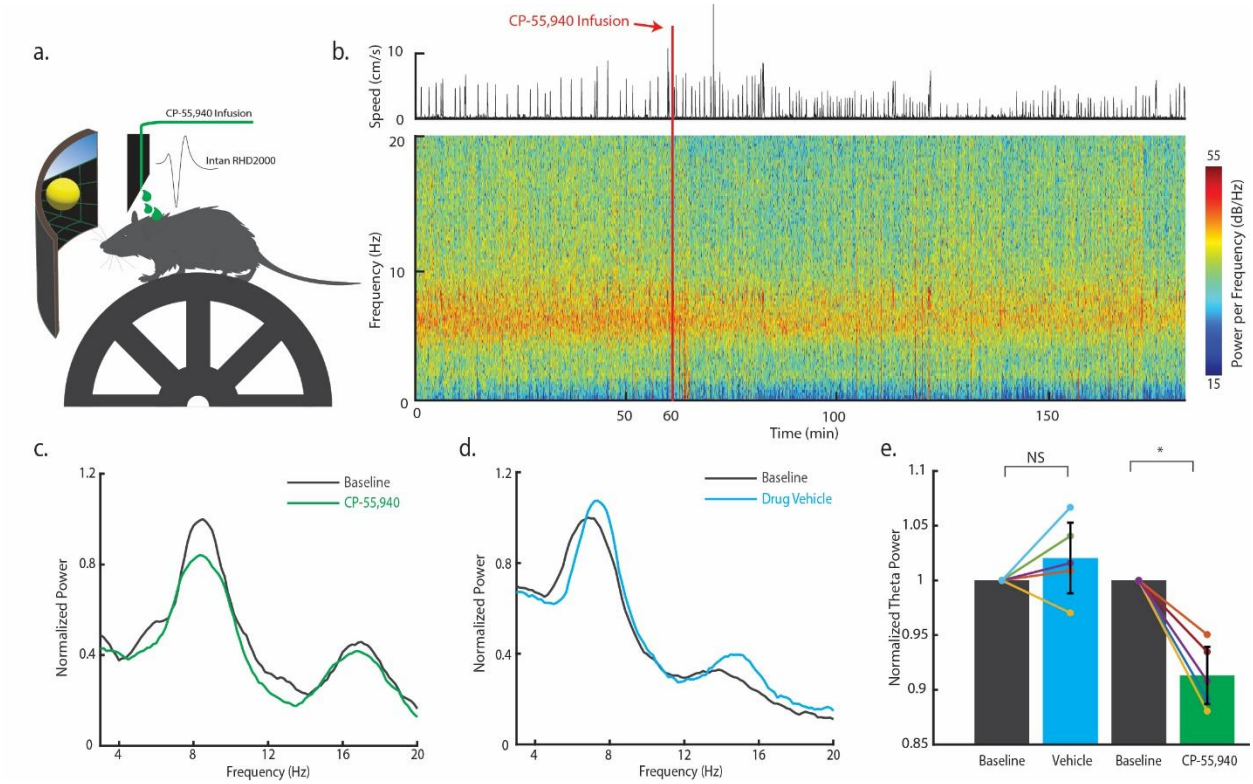

Figure 12: CA1 theta power during running is reduced by pharmacological activation of CB1Rs expressed in CA1. a. Illustration of the experimental setup. A head-fixed, wild-type mouse is mounted on the wheel. A virtual reality environment is presented on the screen to instigate running, and the virtual position is recorded. Local infusion and neural recordings are achieved using the T-DOpE probe. **b.** Power spectrogram of CP-55,940 infusion session in lower frequency bins (0 – 20 Hz). The upper panel shows the speed of the mouse. CP-55,940 (mg kg^{-1}; 200nL; 1nL s^{-1}) is locally infused at the recording sites after 60 minutes of baseline. **c.** Representative

normalized power spectrum of the baseline (Before infusion; duration: 60 minutes) and after CP-55,940 infusion (one hour after infusion; duration: 60 minutes) restricted to running time (>2cm s^{-1} and >1 s running epochs). **d.** Representative normalized power spectrum of the baseline (Before infusion; duration: 60 minutes) and after drug vehicle infusion (one hour after infusion; duration: 60 minutes) restricted to running time with the same criteria as above. **e.** Comparison of the normalized theta power (6 -11 Hz) between baseline and infused vehicle or drug (Paired two-sided t-test, NS: not significant $p \geq 0.05$, * $p \leq 0.05$(Baseline vs. Drug Vehicle, p=0.2737, animal number=5), (Baseline vs. CP-55,940, p=0.0026, animal number=5)). Data are presented as mean ± SD.

Minmax normalized average speed pre and post infusion (1 hour each)

Infusion type	Mouse ID	Mouse Session	Minmax norm. avg. speed & std preinfusion	Minmax norm. avg. speed & std postinfusion	P-value for paired t-test	% time spent running preinfusion (%)	% time spent running postinfusion (%)	P-value for paired t-test
Drug Vehicle	m400	m400_221219	0.0473; 0.0825	0.0532; 0.0960	0.9474 (Avg.Speed pre and post infusion is not stastically significant)	8.26	10.78	0.3353 (%time running pre and postinfusion is not stastically significant)
	m401	m401_221224	0.0698; 0.1257	0.0864; 0.1688		13.82	12.57	
	m402	m402_221212	0.0825; 0.1535	0.0661; 0.1485		20.55	13.82	
	m442	m442_231006	0.0500; 0.1199	0.0418; 0.1240		9.76	6.33	
CP-55,940	m402	m402_220926	0.0844; 0.1739	0.0601; 0.1360	0.8293 (Avg.Speed pre and post infusion is not stastically significant)	17.10	12.31	0.8277 (%time running pre and post infusion is not stastically significant)
	m403	m403_221011	0.0351; 0.0918	0.0455; 0.1010		6.89	7.40	
	m404	m404_221018	0.0633; 0.1149	0.0943; 0.1543		11.92	20.11	
	m441	m441_231005	0.0737; 0.1943	0.0723; 0.1736		11.76	12.51	
	m442	m442_231010	0.0658; 0.1603	0.0606; 0.1607		13.30	11.16	

Supplementary Table 2: Average speed and time spent running of the mice pre and post infusion. Paired two-sided t-tests were used for the comparison.

2.2.6 SPW-R rate lowered by activation of CB1Rs in CA1

Systemic administration of CP-55,940 decreases SPW-R rate and power in behaving animals,[47] and that under urethane anesthesia, intrahippocampal infusion of CP-55,940 reduces SPW-R power.[47] Interestingly, we find similar results for local intrahippocampal infusion in CA1 of behaving mice, further implicating local CB1R expression in changes in CA1. With data recorded from the same setup shown in **fig. 2.6a**, sessions were analyzed in higher frequency bands (100- 300 Hz) to study the influence of CP-55,940 on SPW-Rs. In **fig. 2.7a**, the power spectrogram of a CP-55,940 infusion session was computed with the ripple rate plotted on top. The upper panel shows the speed of the mouse. CP-55,940 (16.8ng; 200nL; $1nLs^{-1}$) was locally infused at the recording site after 60 minutes of baseline recordings. After the infusion, the power in 100-300 Hz bins significantly decreased, which indicates a reduction in SPW-Rs. Importantly, ripple rate returned to baseline after ~ 6 hours. (**fig. 2.7b**). Spectral analysis of the baseline (Before infusion; duration: 60 minutes) after CP-55,940 infusion (one hour after infusion; duration: 60 minutes)

were computed. The bump centered at 150 Hz in the baseline spectrum (**Fig. 2.7c**) disappeared following CP-55,940 infusion, due to the abolishment of SPW-Rs. The difference of the two spectra was plotted to further visualize the change in the power at each frequency (**fig. 2.7d**). The bump in **fig. 2.7c** is highlighted further by the negative peak at 150 Hz, due to impaired SPW-R generation. The ripple rate (per minute, normalized to ripple rate of the first hour) was calculated to investigate the impact of drug infusion on SPW-R occurrence (**fig. 2.7e**, 10 sessions). We compared the normalized SPW-R count between baseline and infused vehicle or drug in **fig. 2.7f**. (Wilcoxon Signed-rank test, ***** $p \leq 0.00001$, NA $p > 0.05$ (Baseline vs. VEH, p=0.5857, animal number=5), (Baseline vs. CP-55,940, p=1.7333e-6, animal number=5)). Overall, the injection of CP-55,940 (but not VEH) significantly lowered the ripple rate. This demonstrates the importance of local CA1 CB1R signaling in SPW-R dynamics in behaving mice.

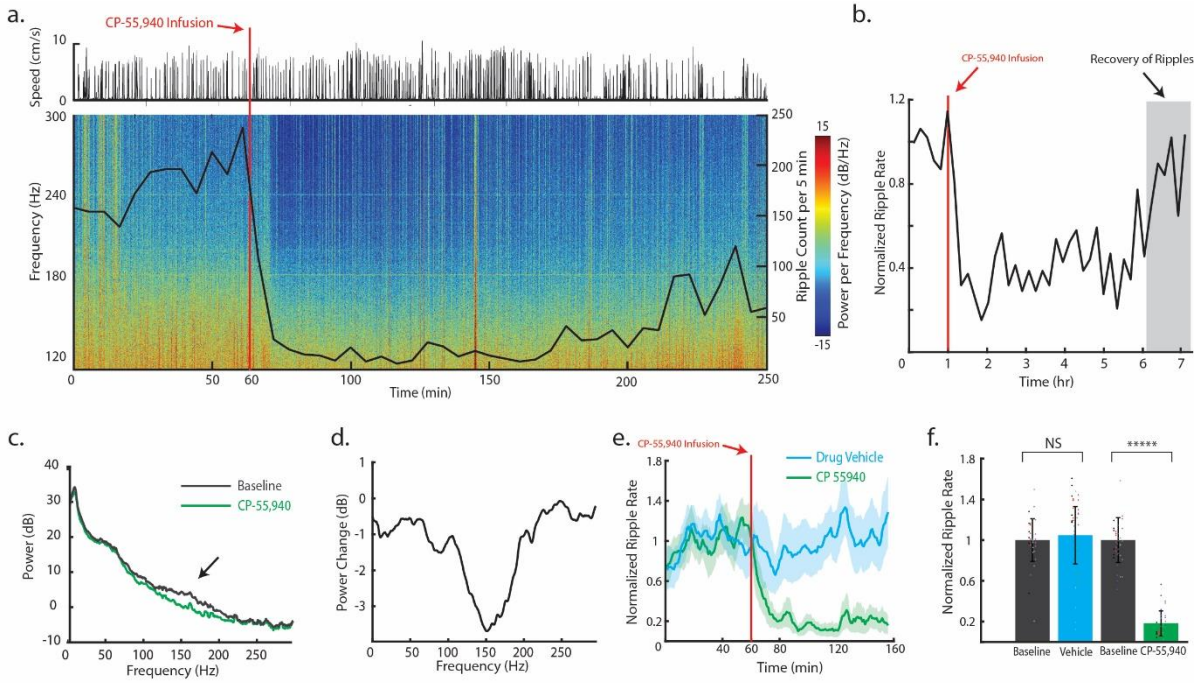

Figure 13: SPW-R rate is lowered by pharmacological activation of CB1Rs expressed in CA1. **a.** Power spectrogram of CP-55,940 infusion session on higher frequency bins (100 – 300 Hz) with the same experimental set-up as Fig. 6a. The ripple rate is plotted on top of the spectrogram with respect to the same timescale. The upper panel shows the speed of the mouse. CP-55,940 (mg kg^{-1}; 200nL; 1nL s^{-1}) is locally infused at the recording sites after 60 minutes of baseline. **b.** Ripple count per 10 minutes over 7-hour recording session **c.** Power spectrum of the baseline (Before infusion; duration: 60 minutes) and after CP-55,940 infusion (one hour after infusion; duration: 60 minutes). **d.** Spectral difference from the baseline to the recording after CP-55,940 infusion. **e.** Normalized ripple rate across all animals and sessions (drug vehicle and CP,55-940 infusion; animal number = 10). Data are presented as mean ± SEM. **f.** Normalized ripple count between baseline and infused vehicle or drug (two-sided Wilcoxon Signed-rank test, ***** $p \leqslant 0.00001$, NA $p > 0.05$ (Baseline vs. VEH, p=0.5857, animal number=5), (Baseline vs. CP-55,940, p=1.7333e-6, animal number=5)). Data are presented as mean ± SEM.

2.2.7 Inability to generate of SPW-Rs b activation of CA1 CB1Rs

SPW-Rs are generated when CA1 receives strong excitatory input from CA3, with the sharp wave resulting from dendritic depolarization of CA1 PYR by CA3, and the fast oscillation due to intra-CA1 interactions between excitatory pyramidal neurons and local GABAergic inhibitory interneurons[37, 68, 80]. While our results confirm that spontaneous SPW-R rate decreases

following intrahippocampal CP-55,940 infusion, it has remained unclear if this is due to signaling at CB1Rs expressed on synaptic terminals originating from CA3 inputs[51, 60, 81] and/or by hippocampal interneurons. To address whether changes in CA3 inputs could explain the reduction in SPW-Rs, we substituted the CA3 sharp wave excitation of CA1 PYR with direct ChR2 depolarization[68]. We used the T-Dope probe to optogenetically depolarize ChR2+ CA1 PYR before and after CP-55,940 infusion. Similar to the setup in **fig. 2.6a**, a head-fixed AAV-CamKII-ChR2 mouse was placed on the wheel with a 473nm laser connected to the T-DOpE probe to deliver optical pulses into CA1 (**fig. 2.8a**). Following 30 minutes of baseline, CA1 pyramidal cells were optically stimulated with a 150 ms optical pulses at low, medium, and high power over 40 minutes (**fig. 2.8b**; n=400 stimulations). 10 minutes after the last optical stimulation, CP-55,940 (16.8ng; 200nL; $1nLs^{-1}$) was focally infused. Once the tissue recovered from infusion, another set of optical pulses was delivered, using the same optical power levels. The spectrogram of the session was computed with the ripple rate overlayed, as shown in **fig. 2.8b**. Note the increased SPW-R events detected from 40–70 minute mark due to the optically induced SPW-Rs. After CP-55,940 infusion, the occurrence of SPW-R events drastically decreased and identical low, medium, and high light pulses were not sufficient to optically induce SPW-Rs (**fig. 2.8c**). Optical stimulation activated the network to the same extent before and after, as indicated by the fact that the mean optical LFP response to identical light pulses was not different (**fig. 2.8d**). Importantly, this demonstrates that failure to generate SPW-Rs post drug is not due to an inability to sufficiently depolarize CA1 neurons.

Wavelet transform was additionally computed and averaged over all sessions to visualized to optically induced SPW-Rs (**fig. 2.8e** and **supplementary fig. 2.8**). **Fig. 2.8f** shows the spectrum of baseline and after drug infusion at high optical pulses. The differences between baseline and

post-drug infusion were larger at higher optical pulse intensity (**fig. 2.8g**). The spectrum response to the high optical power in each session was minmax normalized and averaged (**fig. 2.8h**; animal number=4). The spectral difference between the baseline and CP-55,940 was computed and averaged, shown in **fig. 2.8i**. In all sessions, we observed increase in the ripple rate during the optical stimulation. After infusion of CP-55,940, the ripple rate drastically decreased, as expected from **fig. 2.7**. The optical stimulation after infusion did not recover the SPW-Rs. There is a significant decrease of normalized ripple rate from the baseline to after drug infusion. We also observed a significant difference in the ripple rate during optical stimulations before and after CP-55,940 infusion. (Wilcoxon Signed-rank test, ***** $p \leq 0.00001$, (Baseline vs. CP-55,940, p=1.8162e-5, animal number=4), (Optical Stim vs. Optical Stim after CP-55,940, p=8.2773e-6, animal number=4)). These data further support agonism of CB1Rs expressed by CA1 interneurons as the mechanism of agonist induced SPW-R suppression.

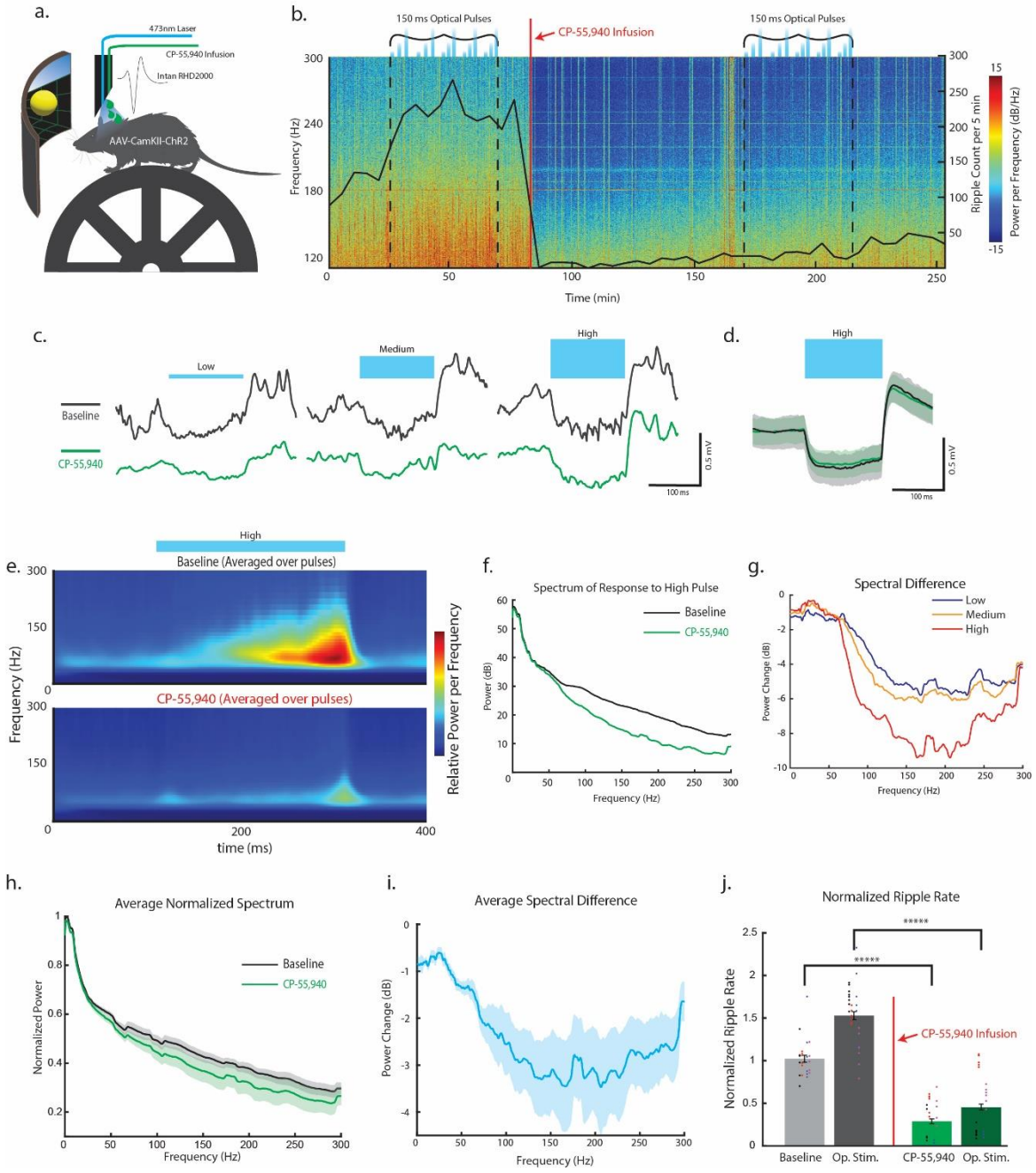

Figure 14: Generation of SPW-Rs by optical stimulation of CA1 PYR is abolished by pharmacological activation of CA1 CB1Rs. a. Illustration of the experimental setup. A head-fixed AAV-CamKII-ChR2 mouse is mounted on the wheel. A virtual reality environment is presented on the screen to instigate running, and the virtual position is recorded. Local infusion, optical stimulation, and neural recording are achieved using the T-DOpE probe. **b.** Power spectrogram of CP-55,940 infusion session on high frequency bins (100 – 300 Hz). Following 30 minutes of baseline, CA1 PYRs are optical stimulated (n=400 pulses of 150 ms at low, medium, and high power) over 40 minutes. CP-55,940 (mg kg^{-1}; 200nL; 1nLs^{-1}) is locally infused at the 80-minute mark. After the cells recover from the infusion, optical stimulation is repeated. **c.** Representative response to low, medium, and high optical stimulations during the baseline and

after CP-55,940 infusion. **d.** Average neural response to the high optical stimulation during the baseline and after CP-55,940 infusion. Data are presented as mean ± SD. **e.** Average Wavelet Transform of the activities in baseline and after drug infusion. **f.** Spectrum of baseline and for CP-55,940 infusion during high pulses. **g.** Spectral difference between the baseline and after CP-55,940 infusion for the optical pulses. **h.** The averaged normalized spectrum (animal number=4). Data are presented as mean ± SD. **i.** The averaged spectral difference between the baseline and after CP-55,940 infusion for high optical pulses (animal number=4). Data are presented as mean ± SD. **j.** Normalized ripple rate during baseline and during optical stimulation. After the infusion, normalized ripple rate 30 min before and during optical stimulation. (two-sided Wilcoxon Signed-rank test, ***** $p \leq 0.00001$, (Baseline vs. CP-55,940, p=1.8162e-5, animal number=4), (Optical Stim vs. Optical Stim after CP-55,940, p=8.2773e-6, animal number=4)). Data are presented as mean ± SEM.

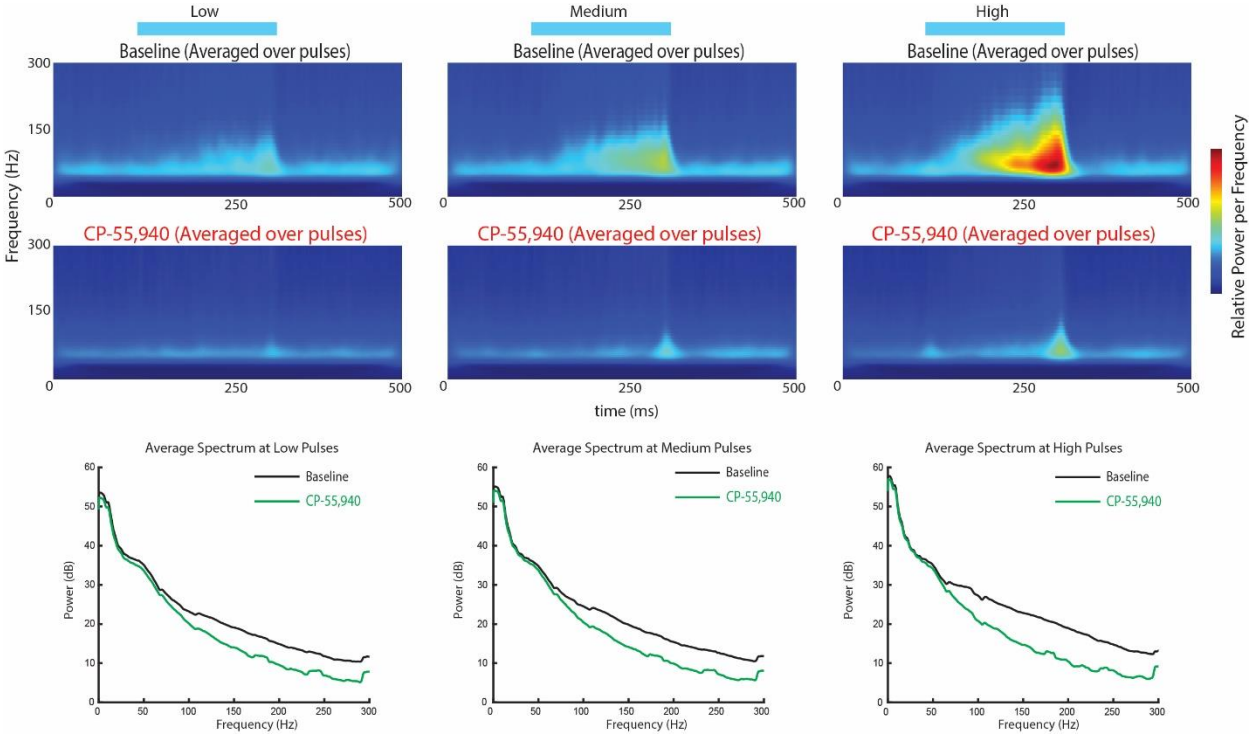

Supplementary Figure 8: Wavelet transforms and spectrum at low medium and high optical pulses.

2.3 Discussion and Conclusion

Here we fabricated T-DOpE probes via a scalable and low-cost thermal tapering method. The method enables high versatility and complexity in probe design, and the semi-automated connection method ensures scalability of the T-DOpE probes. Our *in vivo* study demonstrates

promising future experiments with the T-DOpE probe's reliable and precise recordings with simultaneous optical, and chemical manipulations to understand complex neural circuitry. Here, we used T-DOpE probes to investigate the role of CA1 CB1R signaling in hippocampal activity including theta and SPW-Rs in behaving animals. Our results suggest a critical role for CB1R signaling in the ability for CA1 circuits to generate ripples.

Typically, it is desirable to achieve a thinner probe to minimize tissue response[82] (i.e., neuron-scale devices). The thermal tapering process accomplishes this goal by allowing us to make an ultrafine tip at the tissue interface while maintaining a sizable backend that is compatible with industrial-level soldering/bonding process. For example, we can easily draw down mini-preforms to produce a 50 μm sensing tip with a backend diameter of 2 mm. Compared with cleanroom microfabrication-enabled devices, our approach allows low cost fabrication of flexible and multifunctional devices. Compared with fiber probes fabricated using TDPs, our T-DOpE devices enable dual-size end tips instead of a consistent diameter. In previous fiber probes, electrodes were manually connected by carefully scraping away insulated layers and then electrically connecting the exposed electrode to a pin. Microfluidic channels are connected by attaching polymer tubing to the fiber via a similar process as the electrode connection. Optical connection is done by attaching a ferrule to the back of the fiber, limiting it to one optical connection per device. This manual connection is a time-consuming and labor-intensive process that becomes increasingly difficult as the fiber gets thinner. In our T-DOpE probes, the relatively large size of the backend allows for a semi-automated connection process, reducing connection time, labor, and cost (**fig. 2.3a**; Cost: <10 dollar per unit). In addition, the previous connection process only allows connections to the outer layers of the device, and it is impossible to connect the channels near the center of the fiber without damaging outer channels. This restricts the complexity of the previous

probes. Our connection process enables electrical, optical, and chemical modalities in the entirety of the fiber to be easily connectorized and also allows T-DOpE probes to be readily available for wide distribution. We are eager to disseminate these devices and will make them available to the neuroscience community upon reasonable request. Additionally, devices can be fabricated by neuroscience labs collaborating with engineering labs with relevant skills and customized equipment (see methods).

Using our device, we demonstrated precise optical and chemical modulations *in vivo*. We successfully identified the same monosynaptic connection between a putative pyramidal cell and an interneuron across 43 days which highlights the stability of long-term recording (**fig. 2.4c**). The biocompatibility of the materials in T-DOpE probes (i.e., BiSn, PC, and PVDF) have been previously established.[23, 26] By carefully varying the optical power, we were able to achieve different levels of manipulations of neural circuitry: increasing firing rate and optically inducing SPW-Rs (**fig. 2.8c, 2.7e**). We also characterized the push and return of neurons after local infusion via electrophysiology (**fig. 2.5e**). The slow local infusion allows us to study the pharmaceutical/chemical effects of a local neural circuitry. Depending on the type of chemical, volume, concentration, brain area and duration of the infusion, the likely range is from 0.1-1mm. The slanted cut of the tapered probe minimizes the tissue damage during implantation and enables depth-dependent recording along the device tip. With the T-DOpE probes, we always recorded the typical electrophysiological landmarks of hippocampus CA1, such as multi-units, SPW-Rs, and theta oscillations (**fig. 2.4b**). On top of the recording capability, T-DOpE probe enables optical stimulation for optogenetics and focal drug infusion for pharmacological intervention. The diameter of our probe is ~150 μm and is in between optical fiber (for optogenetics) and silicon

probes. Our device is significantly smaller than a stainless steel cannula which is commonly used in intracranial drug infusion.

Hippocampal circuit activity is critical for episodic and spatial memory. Hippocampal theta (~6-10 Hz), gamma (~35-80 Hz), and sharp wave-ripple (SPW-R, ~100-250 Hz) oscillations all contribute to mnemonic functions of the circuitry.[33-37, 73] Cannabinoids impair memory and alter CA1 rhythms, suggesting a possible role for local CB1R in hippocampal activity and oscillations supporting memory.[47, 48] However, CB1Rs are expressed in multiple hippocampal sub-regions (e.g., both CA1 and CA3) and cell types (e.g., excitatory pyramidal cells and inhibitory interneurons),[51, 58-60, 64, 66] and thus the specific loci of action of cannabinoids on CA1 activity remains unknown. The development of our device has enabled us to further our understanding of the interaction of CB1R and hippocampal oscillations specifically through the focal infusion of agonist during behavior and optogenetic initiation of SPW-Rs.

Administration of CB1R agonists disrupts theta while keeping neuronal firing rate intact, through scrambling temporal coding by cell assemblies.[47, 48] Thus while it is clear that cannabinoids disrupt neural circuits underlying theta, these studies were achieved through systemic administration of cannabinoids in rats. Until our study, it was unknown if cannabinoids were disrupting theta generated upstream of CA1, or within local circuitry. The medial septum, a proposed theta generator, has glutamatergic, cholinergic, and GABAergic connections to CA1.[64] These GABAergic and cholinergic neurons express CB1 receptors, likely inhibiting vesicle release at axon terminals.[57, 58] One hypothesis is that systemic administration of cannabinoids may decrease theta by disrupting circuitry within the medial septum, which prevents effective theta drive in CA1. An alternative hypothesis is that cannabinoids bind to CB1 receptors expressed in CA1, either on CA1 neurons or terminals of inputs into CA1, altering precise timing of

neurotransmitter release resulting in disrupted oscillations.[48] We demonstrated with our T-DOpE probe that local CA1 infusion of CP-55,940 was sufficient to disrupt theta (**fig. 2.6e**), while time spent running and average running speed did not change (**Supplementary table 2.2**). We found there was no statistically significant relationship between theta power and running speed in our experiments (**Supplementary table 2.3**), likely because navigation occurred in a virtual environment.[83] Focal CB1R activation in CA1 is sufficient to weaken the theta oscillation in behaving animals.

Linear mixed estimate model fitted by using fitlme (Matlab)
Power of theta as function of intercept and running speed grouped by infusion conditions

Infusion type	Mouse ID	Mouse Session	P-value for slopes	P-value for intercept
Drug Vehicle	m400	m400_221219	0.56272	8.454e-66
	m401	m401_221224	0.53787	1.4772e-34
	m402	m402_221212	0.19012	1.4671e-105
	m442	m442_231006	0.629	6.1918e-32
CP-55,940	m402	m402_220926	0.37642	3.176e-104
	m403	m403_221011	0.05195	1.5538e-58
	m404	m404_221018	0.69183	4.0685e-109
	m441	m441_231005	0.10348	1.0033e-38
	m442	m442_231010	0.39025	1.6338e-24

Supplementary Table 3: Linear mixed-estimate model of the theta power, velocity of the mice, and the infusion condition.

Cannabinoids inhibit SPW-Rs in rats,[47] suggesting a potential mechanism underlying the memory impairment associated with cannabinoid use in humans. This effect was attributed to reduced glutamate release in CA1 from CA3 afferents,[47, 61, 62] although CB1Rs are expressed in many locations within CA1, leaving the specific mechanism unknown. Importantly activation of CB1Rs on medial septal inputs would be expected to increase not decrease SPW-R rate (activation of the medial septum decreases SPW-R rate).[63] Both CA3 and CA1 neurons express CB1Rs.[51, 58-60, 64] CB1Rs on CA3 axon terminals of the Schaffer collaterals have been shown to act to suppress glutamate release.[51, 60] CA1 PYR express CB1Rs localized on their dendrites, activation has been shown to decrease post-synaptic excitability by increasing membrane conductances.[67] CB1Rs are

highly enriched in CA1 INT where they inhibit GABA release.[58, 59] Given the ambiguous relationship between locus of CB1R expression and SPW-R generation, it was unclear if cannabinoids were acting on excitatory drive from CA3 or local circuit interactions within CA1. Our device allows us to directly interrogate CA1 through local drug delivery and optogenetic stimulation. Our experiments show that CB1R activation is sufficient to disrupt SPW-Rs independent of CA3 synaptic transmission (**fig. 2.8e**), even if the network is sufficiently activated by optogenetic depolarization of CA1 PYR (activating ChR2 expressing PYRs is sufficient to generate CA1 ripples).[68] (**fig. 2.8d**). Thus while previous studies suggested that CB1R inhibit SPW-Rs by cutting off communication from other areas,[61, 62] our findings demonstrate the importance of physiological cannabinoid activity in the CA1 local circuit. Together, these findings reveal mechanisms by which cannabinoids disrupt specific hippocampal rhythms and suggest dysregulation of this tightly controlled system within the CA1 circuit may directly lead to memory impairment.

2.4 Materials and Methods

All protocols and experiments were approved by the Virginia Tech (Blacksburg, VA, USA) Institutional Animal Care and Use Committee (IACUC).

Preform Fabrication

For this study, we fabricated preforms with three different designs corresponding to the 3 different devices used. Preform fabrication for the thermal drawing process (TDP) is an iteration of four steps: machining, inlaying, film wrapping, and consolidation. For all the preforms in this paper, consolidation is performed by heating the preform under vacuum at 190°C. All polymer materials (films, tubes, rods, preforms and mini preforms) used during fabrication were baked

under vacuum at 80℃ to ensure they are moisture free. For the 8 electrode, 1 microfluidic channel and 1 waveguide fiber preform, we start by rolling PVDF films (McMaster-Carr) onto a PC tube (McMaster-Carr). We then rolled PC films (Laminated Plastics) onto the preform and consolidated it. 8 grooves were machined into the consolidated preform and inlayed with BiSn alloy (Indium Corporation). Additional PC films were wrapped around the preform, which is then consolidated. The 8 electrode, 8 microfluidic channel and 4 waveguide fiber preform was fabricated by first milling 4 hollow channels into a solid PC rod. The preform was then wrapped with PC film and consolidated. 4 more hollow channels were machined, and the preform was again wrapped with PC film and consolidated. 12 more hollow channels were machined into the resulting preform, and were inlayed with 8 BiSn alloy strips (Indium Corporation) and 4 polymer waveguides (PC core, PMMA cladding). Finally, the preform was wrapped with additional PC film and consolidated. The 12 microfluidic channel, 8 waveguide fiber was fabricated in a very similar manner. The only differences being 8 hollow channels were machined for the second layer of microfluidic channels, and there were 8 waveguides instead of 4 and no BiSn strips inlayed in the outermost layer of device feature elements.

Mini-preform Fabrication

Thermal drawing of mini-preforms was accomplished utilizing a specialized thermal draw tower which heats the preform in a custom-built furnace and pulls it down to mini-preforms via a capstan motor. The temperature of the furnace, the feeding rate, and the drawing speed control the final geometry of the mini-preform. The furnace is divided into top, middle and bottom sections that can be individually set to different temperatures. The top section preheats the preform, the middle section softens the preform and is where the fiber is drawn. The bottom section is where the fiber is cooled. For our fabrication process, the furnace's sections were set at

150°C, 275°C and 120°C respectively (Note these may not be the actual preform temperatures as they are readouts of the temperature sensors mounted in the furnace). The drawn down fiber's diameter is maintained at 2mm. The fiber is cut into 10cm segments to form mini-preforms for thermal tapering process.

Tapered Device Fabrication

Tapering was achieved using a custom thermal tapering setup built from optomechanical components (Thorlabs), a linear motor, a DC power supply, and a custom-built furnace consisting of a ceramic tube wrapped with nichrome heating wire and thermal insulation. The mini-preform was held in place and the alignment adjusted using opto-mechanical components. A DC power supply was then used to power a custom-designed furnace to 230°C. Note this is the nominal temperature measured by a thermal coupler and may not be the mini-preform's actual temperature. Once the mini-preform was softened, it was pulled via a computer controlled linear motor (Zaber Technologies), resulting in a tapered structure. The speed of the motor and its travel distance can be utilized to adjust the tapered structure's geometry. To produce a neural probe which minimally damages the nearby tissue, the tapered structure was cut at an angle, resulting in two individual T-DOpE probes. This device can be built in an academic lab or engineering core facility with the custom equipment mentioned above and relevant skills.

Assembly of Multifunctional tapered microprobe

The connection of the T-DOpE probe was accomplished on a custom connection setup built with opto-mechanical components. Translation stages (Thorlabs) and a digital microscope (Linkmicro) were used to provide finer position control during connection. For electrical connection, the device backend was heated to 160°C. This temperature is high enough to melt the

BiSn electrodes but low enough to not damage the probe. 42AWG copper wires (Remington Industries) guided by a hypodermic needle were lowered into the melted electrodes. The device was then cooled to solidify the BiSN electrodes. Microfluidic connection was accomplished by inserting a custom drawn hollow (150 µm OD, 75 µm ID) PC tube into the microfluidic channels on the probe's back end. Thermally drawn 200 µm diameter Polymer optical waveguides (PC core, PMMA cladding) were polished (30-1 µm grit) and carefully coupled onto waveguides on the probe's connection end. To seal the microfluidic connection and keep the waveguide in place, UV resin (Piccassio) was applied to the entire probe backend and cured.

To properly interface with our recording setup, optical laser, and drug delivery systems, the probe is further fitted with adapters components. The probe's copper wires were soldered to either pin connectors (chronic implantation) or custom designed PCBs (acute implantation) which can be readily connected to Intan acquisition systems via PCBs purchased from NeuroNexus. The probe's waveguides were connected to Ø1.25mm stainless steel ferrules (Thorlabs). The microfluidic tubes were connected to IDEX Health & Science fluidic components via UV resin. The IDEX components themselves were made compatible with our drug delivery system by a custom-made adapter.

Electrochemical spectral impedance measurement

Impedance measurements are done via a potentiostat (Gamry Instruments). The measurements were performed by lowering the sensing end of a fully connected T-DOpE probe into phosphate-buffered saline (PBS, Thermo Fisher). A Pt wire (Basi) was used as a counter and reference electrode. Data acquisition was accomplished via Gamry's proprietary software.

Headbar Implantation

Mice are induced and maintained at a surgical plane of anesthesia with isoflurane while mounted in stereotax. Hair is removed and scalp is disinfected. Bupivicaine nerve block is injected once under the scalp. The scalp is removed with surgical scissors and the skull is cleaned and dried with 3% hydrogen peroxide, followed by application of the sterile dental adhesive Optibond (Kerr Dental), which is cured with blue light. A < 0.2 mm burr hole is made above the right cerebellum, and a stainless-steel wire is inserted between the skull and the brain, parallel to the brain surface, then the wire is affixed to the skull with sterile dental acrylic. This wire is connected to the ground of the system. A titanium headplate (2 cm long, ~ 1 gram) is positioned above lambda, parallel to skull, and permanently fixed in place with sterile dental acrylic.

Craniotomy

Mice are induced and maintained at a surgical plane of anesthesia with isoflurane while mounted in the stereotax. A 0.5-1.0 mm burr hole (using dental drill with 0.2 mm burr bit) is made above the hippocampus and the dura is removed. Biocompatible silicon elastomer (Kwik-cast; World Precision Instruments) is applied to the burr hole.

AAV Injection

Mice are induced and maintained at a surgical plane of anesthesia with isoflurane while mounted in stereotax. Hair is removed and scalp is disinfected. Bupivicaine nerve block is injected once under the scalp. A < 0.2 mm burr hole is made above the hippocampus (mm from bregma: −1.8, lateral: 1.5). Glass pipette containing AAV5-CaMKIIa-hChR2(H134R)-EYFP (UNC Gene Therapy Center – Vector Core) is lowered into CA1 (mm from surface: -1.2). 100nL of AAV (titer: $4.1x10^{12}$ GC/mL) is injected into tissue ($1nLs^{-1}$) using microinjector syringe pump (WPI: MICRO2T & 504127). Glass pipette is left for 5 minutes for virus to diffuse, then removed from

brain. Craniotomy is covered using biocompatible silicon elastomer (Kwik-SIL; World Precision Instruments) and scalp is closed with Vetbond (3M).

Drug Preparation

CP-55,940 stock was prepared in ethanol at a concentration of 1.68mg/mL. CP-55,940 injection solution was a mixture of 1:1:18 ethanol, solubilizer, and saline for a final drug concentration of 84μg/mL. 200nL of solution was delivered at a rate of $1nLs^{-1}$ directly into CA1. For a total delivery of an estimated 16.8ng or 44.6picomols. Drug vehicle solution was a mixture of 1:1:18 ethanol, solubilizer, and saline. 200nL of vehicle solution was delivered at a rate of 1nL s^{-1} directly into CA1. We used a standard precision injection apparatus (NanoFil Syringe and UMP-3 Syringe pump, World Precision Instruments) for all tests and experiment.

***In Vivo* recording**

All mice used in experiments were derived from crossing C57BL/6J (JAX #000664) x FVB/NJ (JAX #001800). During the time of experiments, mice were between the ages of 16-30 weeks old. Mice of both sex were used in all experiments. Mice, trained and habituated to head-fixed navigation, are placed in the head fixation apparatus, and the T-DOpE probe is lowered through the craniotomy into the brain until SPW-Rs are recognized and left in place for 30-45 minutes until tissue is relaxed. The amplified neural signals are then recorded with RHD2000 system (Intan Technologies LLC). For chronic recordings, probe was fixed to the skull with dental cement, after the probe was lowered into CA1 and SPW-Rs were identified.

Optical Stimulation

The T-DOpE probe's optical ferrule was coupled to a diode-pumped solid-state (DPSS) laser (Laserglow Tehcnologies, 100mW maximum power, wavelength = 473nm.) through a mating

sleeve (Thorlabs). We calibrated the optical output of our probe for each optical session. The optically evoked activity was closely monitored to meet the desired power output. The outputs of the optical power varied between 50 -700 μW. We calculated the optical power density to be 3 - 47 mW/mm^2. For investigating the effect of CP-55,940, 400, 150 ms optical pulses at low, medium, and high power were delivered. Time in between the power levels were set to 1 second (one set), and time in between stimulation sets was 5 seconds long.

Data analysis

Data analysis was carried out with Matlab (The Mathworks) and custom scripts were used to analyze the extracellular recording. Due to the nature of the experiment where the researcher had to prepare the drug immediately before the experiment, they were not blinded to the manipulation conditions. However, analysis pipelines including ripple detection and theta power detection were consistent across animals and were not manipulated for experimental condition. For each session, the LFP power analysis was performed on the electrode right above the electrode detecting highest power of SPW-R. The data was low-pass filtered and then downsampled from 30 kHz to 1250 Hz. Spectrograms were computed to visually analyze the sessions in both time and frequency domain. The calculations of spectrograms were computed using hamming window of 5 seconds and overlaps of 2.5 seconds. The calculation of power spectral density was performed by using the multi-taper estimate method. SPW-Rs were detected using the LFP data. The LFP was first spectrally filtered from 100 to 250 Hz and threshold filtered to 1.5- 3.0 of the standard deviation of the whole data. The events that exceed 40- 50 ms were counted towards the SPW-R events. The SPW-R was visually inspected and compared with the raw recording. The threshold and the duration of the SPW-Rs were manually adjusted to minimize the error in detection. The running epochs were computed by taking the derivative of the virtual position of the mouse

(>2cm/s and >1s running epochs). The power spectra of the running epoch were also computed using the multi-taper estimate method. The spectra were also minmax normalized for the comparison over all the session (**fig. 2.6c,d**). Since the peak of the theta power varied over the animals and sessions, we computed the area under the curve (6-11 Hz) for the comparison between baseline and vehicle or drug (**fig. 2.4e**). The average running speed were computed for each running epoch. The average running speed pre and post infusion was also computed to compare running behavior before and after drug infusion. The percent time spent running was computed for all sessions. The Shpiro-Wilk normality test was adapted to check for normality and the paired t-test was used to observe the running behavior pre and post infusion. Linear mixed-effects model was used to characterize the relation between the running speed and the theta power. Spectra of the optically induced activity were computed using the multi-taper estimate. To maintain the temporal information, the Wavelet Transform was computed and averaged. Spike sorting was performed using Kilosort1, followed by manual refinement using[84, 85]. The putative cell type identification and cluster quality analysis was completed using Cell Explorer.[74] The cross-correlogram and auto-correlogram were normalized for visual observations. The two comparison groups were tested with Shapiro-Wilk normality test to check if the groups are normally distributed. If the two groups were normally distributed, we used the paired two-sided T-test. For those that are not normally distributed, the experimental designs with two comparison groups were analyzed by two-sided Wilcoxon signed rank tests. The difference between the two groups were considered statistically significant if the p-value is less than 0.05. All tests were performed using Matlab code.

2.5 Reference

1. Buzsáki, G. Large-scale recording of neuronal ensembles. *Nature neuroscience* **7**, 446-451 (2004).

2. Steinmetz, N.A. et al. Neuropixels 2.0: A miniaturized high-density probe for stable, long-term brain recordings. *Science* **372** (2021).
3. Chung, J.E. et al. High-Density, Long-Lasting, and Multi-region Electrophysiological Recordings Using Polymer Electrode Arrays. *Neuron* **101**, 21-31.e25 (2019).
4. Ko, E., Vöröslakos, M., Buzsáki, G. & Yoon, E. flexLiTE: flexible micro-LED integrated optoelectrodes for minimally-invasive chronic deep-brain study. *bioRxiv*, 2022.2008.2005.503006 (2022).
5. Patel, P.R. et al. Chronic in vivo stability assessment of carbon fiber microelectrode arrays. *Journal of Neural Engineering* **13**, 066002 (2016).
6. Viventi, J. et al. Flexible, foldable, actively multiplexed, high-density electrode array for mapping brain activity in vivo. *Nature Neuroscience* **14**, 1599-1605 (2011).
7. Campbell, P.K., Jones, K.E., Huber, R.J., Horch, K.W. & Normann, R.A. A silicon-based, three-dimensional neural interface: manufacturing processes for an intracortical electrode array. *IEEE Trans Biomed Eng* **38**, 758-768 (1991).
8. LeChasseur, Y. et al. A microprobe for parallel optical and electrical recordings from single neurons in vivo. *Nature Methods* **8**, 319-325 (2011).
9. Zhao, Z. et al. Ultraflexible electrode arrays for months-long high-density electrophysiological mapping of thousands of neurons in rodents. *Nature Biomedical Engineering* **7**, 520-532 (2023).
10. Marc, D.F. et al. NeuroRoots, a bio-inspired, seamless Brain Machine Interface device for long-term recording. *bioRxiv*, 460949 (2018).
11. Lundy-Ekman, L. Neuroscience-e-book: fundamentals for rehabilitation. (Elsevier Health Sciences, 2012).
12. Carandini, M. From circuits to behavior: a bridge too far? *Nature neuroscience* **15**, 507-509 (2012).
13. Quiroga, R.Q., Reddy, L., Kreiman, G., Koch, C. & Fried, I. Invariant visual representation by single neurons in the human brain. *Nature* **435**, 1102-1107 (2005).
14. Ekstrom, A.D. et al. Cellular networks underlying human spatial navigation. *Nature* **425**, 184-188 (2003).
15. Boyden, E.S., Zhang, F., Bamberg, E., Nagel, G. & Deisseroth, K. Millisecond-timescale, genetically targeted optical control of neural activity. *Nature Neuroscience* **8**, 1263-1268 (2005).
16. Zhang, F., Aravanis, A.M., Adamantidis, A., de Lecea, L. & Deisseroth, K. Circuit-breakers: optical technologies for probing neural signals and systems. *Nature Reviews Neuroscience* **8**, 577-581 (2007).
17. Zhao, Z. et al. Nanoelectronic Coating Enabled Versatile Multifunctional Neural Probes. *Nano Letters* **17**, 4588-4595 (2017).
18. Rubehn, B., Wolff, S.B.E., Tovote, P., Lüthi, A. & Stieglitz, T. A polymer-based neural microimplant for optogenetic applications: design and first in vivo study. *Lab on a Chip* **13**, 579-588 (2013).
19. Kim, K. et al. Artifact-free and high-temporal-resolution in vivo opto-electrophysiology with microLED optoelectrodes. *Nature Communications* **11**, 2063 (2020).
20. Zou, L. et al. Self-assembled multifunctional neural probes for precise integration of optogenetics and electrophysiology. *Nature Communications* **12**, 5871 (2021).
21. Jeong, J.-W. et al. Wireless Optofluidic Systems for Programmable In Vivo Pharmacology and Optogenetics. *Cell* **162**, 662-674 (2015).

22. Shin, H. et al. Multifunctional multi-shank neural probe for investigating and modulating long-range neural circuits in vivo. *Nature Communications* **10**, 3777 (2019).
23. Canales, A. et al. Multifunctional fibers for simultaneous optical, electrical and chemical interrogation of neural circuits in vivo. *Nature biotechnology* **33**, 277-284 (2015).
24. Loke, G. et al. Digital electronics in fibres enable fabric-based machine-learning inference. *Nature Communications* **12**, 3317 (2021).
25. Marion, J.S. et al. Thermally Drawn Highly Conductive Fibers with Controlled Elasticity. *Advanced Materials* **34**, 2201081 (2022).
26. Jiang, S. et al. Spatially expandable fiber-based probes as a multifunctional deep brain interface. *Nature Communications* **11**, 6115 (2020).
27. Yan, W. et al. Thermally drawn advanced functional fibers: New frontier of flexible electronics. *Materials Today* **35**, 168-194 (2020).
28. Kim, J. et al. Laser Machined Fiber-Based Microprobe: Application in Microscale Electroporation. *Advanced Fiber Materials* **4**, 859-872 (2022).
29. Zhang, Y. et al. Thermally Drawn Stretchable Electrical and Optical Fiber Sensors for Multimodal Extreme Deformation Sensing. *Advanced Optical Materials* **9**, 2001815 (2021).
30. Pisano, F. et al. Depth-resolved fiber photometry with a single tapered optical fiber implant. *Nature Methods* **16**, 1185-1192 (2019).
31. Redish, A.D. Beyond the cognitive map: from place cells to episodic memory. (MIT press, 1999).
32. Buzsáki, G. & Moser, E.I. Memory, navigation and theta rhythm in the hippocampal-entorhinal system. *Nature Neuroscience* **16**, 130-138 (2013).
33. Buzsáki, G. Theta Oscillations in the Hippocampus. *Neuron* **33**, 325-340 (2002).
34. Buzsáki, G. Theta rhythm of navigation: Link between path integration and landmark navigation, episodic and semantic memory. *Hippocampus* **15**, 827-840 (2005).
35. Buzsáki, G. Two-stage model of memory trace formation: A role for “noisy” brain states. *Neuroscience* **31**, 551-570 (1989).
36. Wilson, M.A. & McNaughton, B.L. Reactivation of Hippocampal Ensemble Memories During Sleep. *Science* **265**, 676-679 (1994).
37. Buzsáki, G. Hippocampal sharp wave-ripple: A cognitive biomarker for episodic memory and planning. *Hippocampus* **25**, 1073-1188 (2015).
38. Fernández-Ruiz, A. et al. Long-duration hippocampal sharp wave ripples improve memory. *Science* **364**, 1082-1086 (2019).
39. Girardeau, G., Benchenane, K., Wiener, S.I., Buzsáki, G. & Zugaro, M.B. Selective suppression of hippocampal ripples impairs spatial memory. *Nature Neuroscience* **12**, 1222-1223 (2009).
40. Gridchyn, I., Schoenenberger, P., O'Neill, J. & Csicsvari, J. Assembly-Specific Disruption of Hippocampal Replay Leads to Selective Memory Deficit. *Neuron* **106**, 291-300.e296 (2020).
41. Ego-Stengel, V. & Wilson, M.A. Disruption of ripple-associated hippocampal activity during rest impairs spatial learning in the rat. *Hippocampus* **20**, 1-10 (2010).
42. Jadhav, S.P., Kemere, C., German, P.W. & Frank, L.M. Awake Hippocampal Sharp-Wave Ripples Support Spatial Memory. *Science* **336**, 1454-1458 (2012).
43. Soltesz, I. et al. Weeding out bad waves: towards selective cannabinoid circuit control in epilepsy. *Nature Reviews Neuroscience* **16**, 264-277 (2015).

44. Chesher, G.B., Jackson, D.M. & Malor, R.M. Interaction of Δ9-tetrahydrocannabinol and cannabidiol with phenobarbitone in protecting mice from electrically induced convulsions. *Journal of Pharmacy and Pharmacology* **27**, 608-609 (1975).
45. Karler, R. & Turkanis, S.A. SUBACUTE CANNABINOID TREATMENT: ANTICONVULSANT ACTIVITY AND WITHDRAWAL EXCITABILITY IN MICE. *British Journal of Pharmacology* **68**, 479-484 (1980).
46. Wallace, M.J., Wiley, J.L., Martin, B.R. & DeLorenzo, R.J. Assessment of the role of CB1 receptors in cannabinoid anticonvulsant effects. *European Journal of Pharmacology* **428**, 51-57 (2001).
47. Robbe, D. et al. Cannabinoids reveal importance of spike timing coordination in hippocampal function. *Nature Neuroscience* **9**, 1526-1533 (2006).
48. Robbe, D. & Buzsáki, G. Alteration of Theta Timescale Dynamics of Hippocampal Place Cells by a Cannabinoid Is Associated with Memory Impairment. *The Journal of Neuroscience* **29**, 12597 (2009).
49. Lichtman, A.H., Dimen, K.R. & Martin, B.R. Systemic or intrahippocampal cannabinoid administration impairs spatial memory in rats. *Psychopharmacology* **119**, 282-290 (1995).
50. Lichtman, A.H. & Martin, B.R. Δ9-Tetrahydrocannabinol impairs spatial memory through a cannabinoid receptor mechanism. *Psychopharmacology* **126**, 125-131 (1996).
51. Abush, H. & Akirav, I. Cannabinoids modulate hippocampal memory and plasticity. *Hippocampus* **20**, 1126-1138 (2010).
52. Wise, L.E., Thorpe, A.J. & Lichtman, A.H. Hippocampal CB1 Receptors Mediate the Memory Impairing Effects of Δ9-Tetrahydrocannabinol. *Neuropsychopharmacology* **34**, 2072-2080 (2009).
53. Ranganathan, M. & D'Souza, D.C. The acute effects of cannabinoids on memory in humans: a review. *Psychopharmacology* **188**, 425-444 (2006).
54. Ilan, A.B., Smith, M.E. & Gevins, A. Effects of marijuana on neurophysiological signals of working and episodic memory. *Psychopharmacology* **176**, 214-222 (2004).
55. Curran, V.H., Brignell, C., Fletcher, S., Middleton, P. & Henry, J. Cognitive and subjective dose-response effects of acute oral Δ9-tetrahydrocannabinol (THC) in infrequent cannabis users. *Psychopharmacology* **164**, 61-70 (2002).
56. Farrell, J.S. et al. In vivo endocannabinoid dynamics at the timescale of physiological and pathological neural activity. *Neuron* **109**, 2398-2403.e2394 (2021).
57. Sullivan, J.M. Mechanisms of Cannabinoid-Receptor–Mediated Inhibition of Synaptic Transmission in Cultured Hippocampal Pyramidal Neurons. *Journal of Neurophysiology* **82**, 1286-1294 (1999).
58. Katona, I. et al. Presynaptically Located CB1 Cannabinoid Receptors Regulate GABA Release from Axon Terminals of Specific Hippocampal Interneurons. *The Journal of Neuroscience* **19**, 4544 (1999).
59. Losonczy, A., Biró, Á.A. & Nusser, Z. Persistently active cannabinoid receptors mute a subpopulation of hippocampal interneurons. *Proceedings of the National Academy of Sciences* **101**, 1362-1367 (2004).
60. Takahashi, K.A. & Castillo, P.E. The CB1 cannabinoid receptor mediates glutamatergic synaptic suppression in the hippocampus. *Neuroscience* **139**, 795-802 (2006).

61. Sandler, R.A., Fetterhoff, D., Hampson, R.E., Deadwyler, S.A. & Marmarelis, V.Z. Cannabinoids disrupt memory encoding by functionally isolating hippocampal CA1 from CA3. *PLOS Computational Biology* **13**, e1005624 (2017).
62. Maier, N. et al. Cannabinoids disrupt hippocampal sharp wave-ripples via inhibition of glutamate release. *Hippocampus* **22**, 1350-1362 (2012).
63. Vandecasteele, M. et al. Optogenetic activation of septal cholinergic neurons suppresses sharp wave ripples and enhances theta oscillations in the hippocampus. *Proceedings of the National Academy of Sciences* **111**, 13535-13540 (2014).
64. Nyíri, G. et al. GABAB and CB1 cannabinoid receptor expression identifies two types of septal cholinergic neurons. *European Journal of Neuroscience* **21**, 3034-3042 (2005).
65. Busquets-Garcia, A., Bains, J. & Marsicano, G. CB1 Receptor Signaling in the Brain: Extracting Specificity from Ubiquity. *Neuropsychopharmacology* **43**, 4-20 (2018).
66. Neu, A., Földy, C. & Soltesz, I. Postsynaptic origin of CB1-dependent tonic inhibition of GABA release at cholecystokinin-positive basket cell to pyramidal cell synapses in the CA1 region of the rat hippocampus. *The Journal of Physiology* **578**, 233-247 (2007).
67. Maroso, M. et al. Cannabinoid Control of Learning and Memory through HCN Channels. *Neuron* **89**, 1059-1073 (2016).
68. Stark, E. et al. Pyramidal Cell-Interneuron Interactions Underlie Hippocampal Ripple Oscillations. *Neuron* **83**, 467-480 (2014).
69. Klausberger, T. et al. Brain-state- and cell-type-specific firing of hippocampal interneurons in vivo. *Nature* **421**, 844-848 (2003).
70. Royer, S. et al. Control of timing, rate and bursts of hippocampal place cells by dendritic and somatic inhibition. *Nature Neuroscience* **15**, 769-775 (2012).
71. Dániel, S., Szabolcs, K., Tamás, F.F., Norbert, H. & Attila, I.G. Mechanisms of Sharp Wave Initiation and Ripple Generation. *The Journal of Neuroscience* **34**, 11385 (2014).
72. Korposh, S., James, S.W., Lee, S.-W. & Tatam, R.P. in Sensors, Vol. 19 (2019).
73. Buzsáki, G., Lai-Wo S, L. & Vanderwolf, C.H. Cellular bases of hippocampal EEG in the behaving rat. *Brain Research Reviews* **6**, 139-171 (1983).
74. Petersen, P.C., Siegle, J.H., Steinmetz, N.A., Mahallati, S. & Buzsáki, G. CellExplorer: A framework for visualizing and characterizing single neurons. *Neuron* **109**, 3594-3608.e3592 (2021).
75. Gulyás, A.I. et al. Hippocampal pyramidal cells excite inhibitory neurons through a single release site. *Nature* **366**, 683-687 (1993).
76. English, D.F. et al. Pyramidal Cell-Interneuron Circuit Architecture and Dynamics in Hippocampal Networks. *Neuron* **96**, 505-520.e507 (2017).
77. Lee, H.C. et al. Histological evaluation of flexible neural implants; flexibility limit for reducing the tissue response? *Journal of Neural Engineering* **14**, 036026 (2017).
78. Yoon, Y. et al. Neural probe system for behavioral neuropharmacology by bi-directional wireless drug delivery and electrophysiology in socially interacting mice. *Nature Communications* **13**, 5521 (2022).
79. Shin, H. et al. Neural probes with multi-drug delivery capability. *Lab on a Chip* **15**, 3730-3737 (2015).
80. Buzsáki, G., Horváth, Z., Urioste, R., Hetke, J. & Wise, K. High-frequency network oscillation in the hippocampus. *Science* **256**, 1025-1027 (1992).

81. Németh, B., Ledent, C., Freund, T.F. & Hájos, N. CB1 receptor-dependent and -independent inhibition of excitatory postsynaptic currents in the hippocampus by WIN 55,212-2. *Neuropharmacology* **54**, 51-57 (2008).
82. Thelin, J. et al. Implant size and fixation mode strongly influence tissue reactions in the CNS. *PLoS One* **6**, e16267 (2011).
83. Ravassard, P. et al. Multisensory Control of Hippocampal Spatiotemporal Selectivity. *Science* **340**, 1342-1346 (2013).
84. Pachitariu, M., Steinmetz, N., Kadir, S., Carandini, M. & Kenneth D, H. Kilosort: realtime spike-sorting for extracellular electrophysiology with hundreds of channels. *bioRxiv*, 061481 (2016).
85. Rossant, C. & Harris, K.D. Hardware-accelerated interactive data visualization for neuroscience in Python. *Frontiers in neuroinformatics* **7**, 36 (2013).

Chapter 3
Multifunctional Tetrode-like Drug Delivery, Optical Stimulation, and Electrophysiology (Tetro-DOpE) Probes

3.1 Introduction

Understanding how neural activity encodes information on a systems level requires studying neural spiking and circuit activity in awake and behaving animals.[1-7] Tools that enable monitoring single neuron action potentials in behaving animals have yielded some of the most striking discoveries of the neural correlates of behavior (e.g. place cells using single wires and grid cells using tetrodes).[8-12] Tetrodes are used widely by the neuroscience community due to low-cost of fabrication, ease of adapting the probes in new experimental designs and the ability to perform single-unit isolation in anatomically dense neuronal populations (e.g. pyramidal layer of the hippocampus).[8, 13, 14] Such classical tetrodes are passive recording devices, that is they cannot modulate neural activity. Leveraging advances in fluorescent protein sensors and optogenetics,[15-21] bi-directional neural probes have been developed allowing simultaneous monitoring and manipulation of neural activity via electrodes and light delivery.[22-27] More recently, multifunctional probes with additional manipulation dimensions, such as drug delivery channels, have emerged.[28-32] Developing multifunctional "tetrode"-like neural probes that harness the advantages of tetrodes while also enabling simultaneous multimodal neural modulation would open new avenues of systems neuroscience investigation.

There has been significant progress in multifunctional neural probes over the past few years.[25, 33-36] However, existing multifunctional probes have a fixed configuration once fabricated, and it is difficult to customize the probes for different applications. In addition, most of the multifunctional probes are fabricated using cleanroom microfabrication techniques which are time

consuming and expensive. Alternatively, the thermal drawing process (TDP) has been developed as a promising platform for producing low cost and scalable multifunctional neural probes.[28, 29, 34, 37-40] The process was originally adapted from optical fiber fabrication, where glass preforms (macro version of fiber) are heated and pulled to thin fibers. The TDP process enables scalable fabrication of multi-material (i.e., metal, polymer, semiconductor) fiber via optimization of furnace temperature and fiber pulling speed. The fiber is cut into segments and assembled into fiber-based sensors and actuators. However, there are two major challenges with this technology: (1) similar to other multifunctional probes, a new probe configuration would require a separate thermal drawing process from a new preform. (2) To achieve a small sensing end, the backend necessarily decreases in size (due to the uniform diameter along the fiber length), making the connection process harder and more complicated.

To overcome these challenges, we implemented a bundling process, similar to the preparation of classical tetrodes, into our device fabrication. We fabricated various designs of thin (<50 um) multifunctional fibers that can be bundled in any combination. This process avoids the redesign of a fixed configuration and enables rapid, in-house modular customization. Due to the relatively low count of features (electrodes, optical waveguide, and microfluidic channel) in each thin fiber, connection to the outside modules (recording setups, lasers, and microfluidic pumps) is a trivial process. As a result, we developed a fabrication method where the thin multifunctional fibers are bundled to produce tetrode-like drug delivery, optical stimulation, and electrophysiology (Tetro-DOpE) probes (Fig. 3.1).

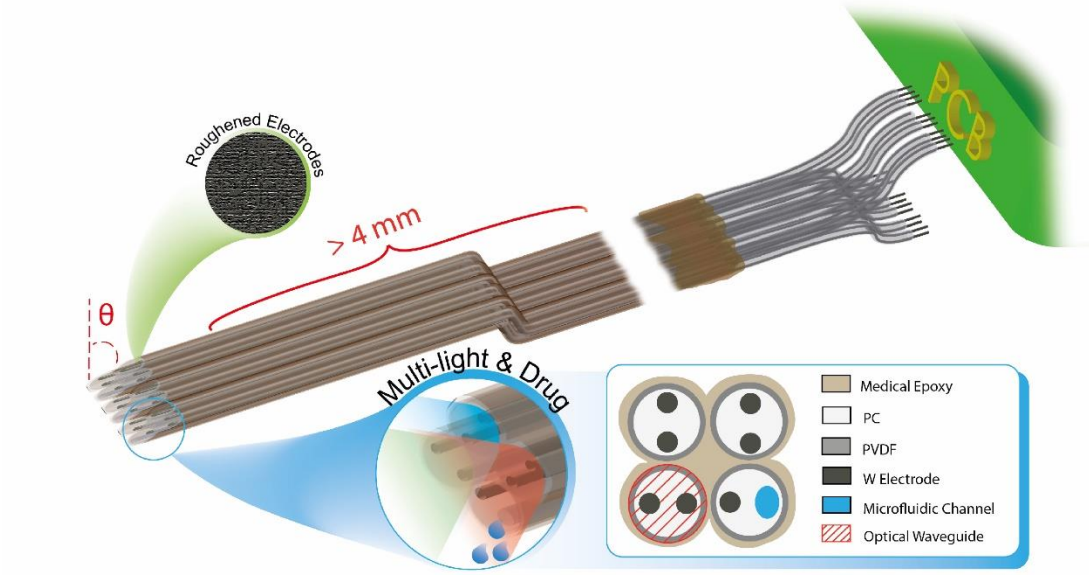

Figure 3.15: Illustration of the Tetro-DOpE probe. The probe enables multi-light and drug delivery. These bundled probes can be further assembled into bulks and/or shanks to increase the feature counts (i.e., electrodes, channels, and optical waveguides).

Here, we present highly customizable and affordable Tetro-DOpE probes which enable simultaneous electrophysiology recording, optogenetic manipulations, and local drug infusion. We designed various thin multifunctional fibers via the scalable convergence thermal drawing process which are then bundled to fabricate Tetro-DOpE probes. To demonstrate recording quality, probes were implanted in hippocampus CA1 and reliably recorded canonical CA1 circuit dynamics including theta oscillations and sharp wave-ripples (SPW-Rs) without inducing pathological states (e.g. seizures). We verified the functional ability for optical waveguides and microfluidic channels to manipulate neuronal activity in head-fixed behaving mice. To illustrate the high customizability of Tetro-DOpE probes, we assembled six-shank probes on a microdrive. The assembled probes were chronically implanted bilaterally in dorsal CA1, and stable long-term recordings were obtained in such freely moving mice. These *in vivo* experiments demonstrate that our highly

scalable and customizable Tetro-DOpE probes are capable of reliably recording and manipulating neural activity in freely behaving animals.

3.2 Results

3.2.1 Tetro-DOpE fabrication via thermal drawing process

Various designs of Tetro-DOpE probes were assembled by bundling thin multifunctional polymer fibers (<50 μm), fabricated using the convergence thermal drawing process (CTDP (Fig. 3.2a)). Critically, CTDP enables fabrication of fibers composed of multiple materials, even those with vastly different thermal properties such as metals and thermoplastics. Here, we used machining techniques to fabricate macro designed preforms consisting of a polycarbonate (PC) core (refractive index =1.59), polyvinylidene fluoride (PVDF) cladding (refractive index n= 1.41), and one or two hollow channels for the insertion of tungsten metal electrodes. Then, the preform is further wrapped in PC film, a sacrificial layer that stabilizes the drawing process and thermally consolidated (Supplementary Fig. 3.1). The preform was mounted in a custom-built furnace, heated, and pulled while tungsten wires (15 μm) were simultaneously fed into the hollow channels. The sacrificial PC layer is chemically etched with Dichloromethane (DCM) reducing the fiber diameter to <50 μm. The optical waveguide is composed of the PC core and PVDF cladding, while convergence of the tungsten wires within the empty channels results in functional electrodes. Three different fiber designs are illustrated in Fig. 3.2b: one electrode and one optical waveguide (F1), two electrodes and one optical waveguide (F2), and one electrode and one microfluidic channel (F3). The fibers produced with CTDP are flexible enough to be wrapped around a human finger without damage (Fig. 3.2c), and hundreds of meters can be fabricated from a single CTDP draw. Tetro-DOpE probes were fabricated by bundling fibers into a tetrode configuration by coating with medical epoxy and using a short PC scaffold to produce a uniform geometry by removing excess

epoxy (fig. 3.2d). Various designs of Tetro-DOpE probes are shown in Fig. 3.2e: (i) four electrodes and four optical waveguides, (ii) four electrodes and two optical waveguides, and (iii) three electrodes, two optical waveguides, and one microfluidic channel. Illustrated in fig. 3.2f is a fully assembled Tetro-DOpE probe with three electrodes for electrophysiology, two optical waveguides for optogenetics, and one microfluidic channel for local pharmacological intervention.

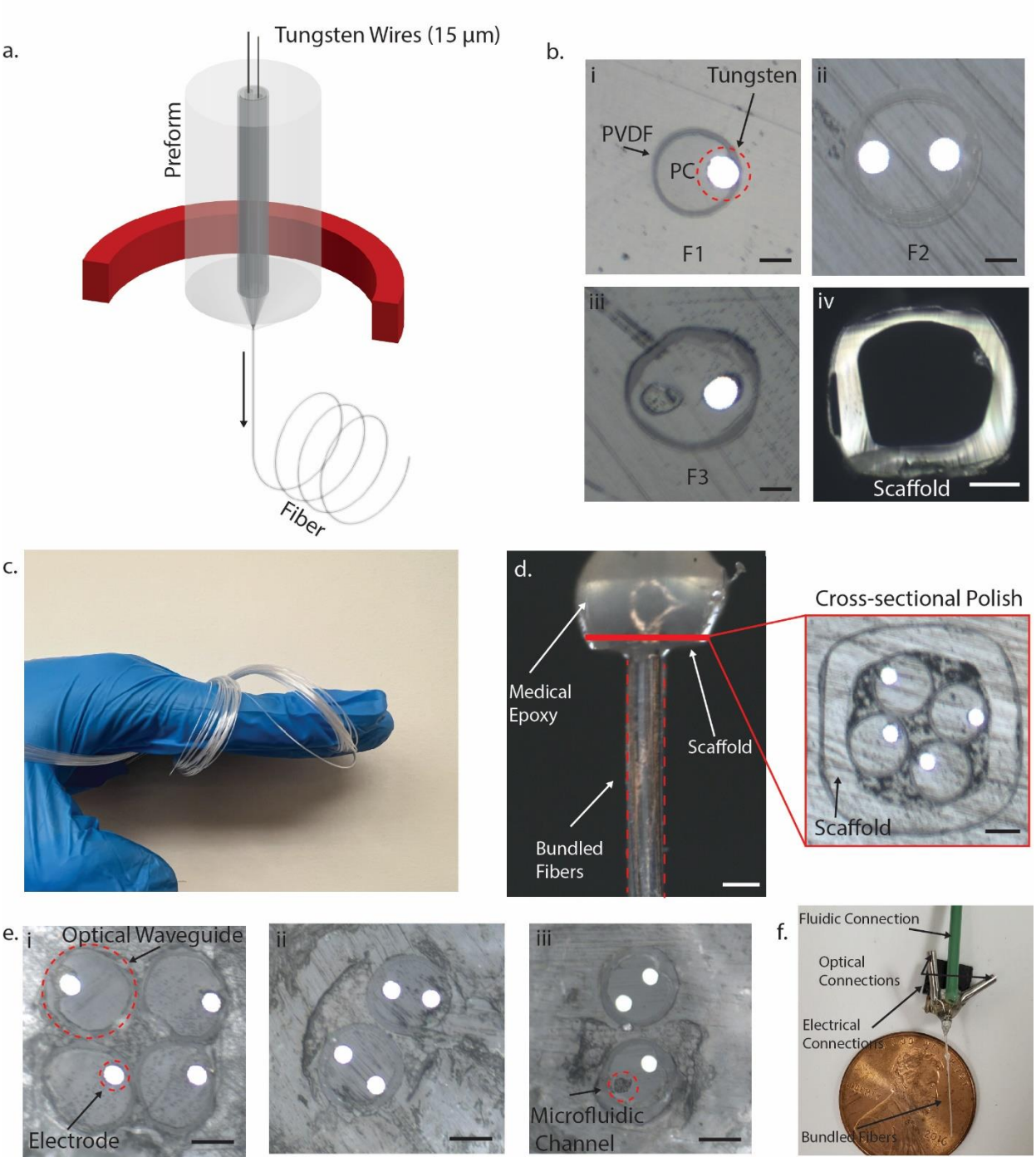

Figure 3.16: **a.** Schematic of the convergence thermal drawing process. **b.** Thermally drawn fiber with various designs before chemically etched. (i. one electrode and one waveguide. ii. two electrodes and one waveguide. iii. one electrode and one channel. iv. scaffold) **c.** Demonstration of the flexibility and the scalability of the fibers. **d.** Enlarged photograph and cross-sectional image of the scaffold and bundled fibers. The sliding scaffold cleans the excess medical epoxy. **e.** Cross-sectional image of the Tetro-DOpE probes with various configurations. (i. four electrodes and four waveguides. ii. four electrodes and two waveguides. iii. Three electrodes, one waveguide, and one channel) **f.** Image of a working probe connected to fluidic tube, optical ferrules, and pin connectors.

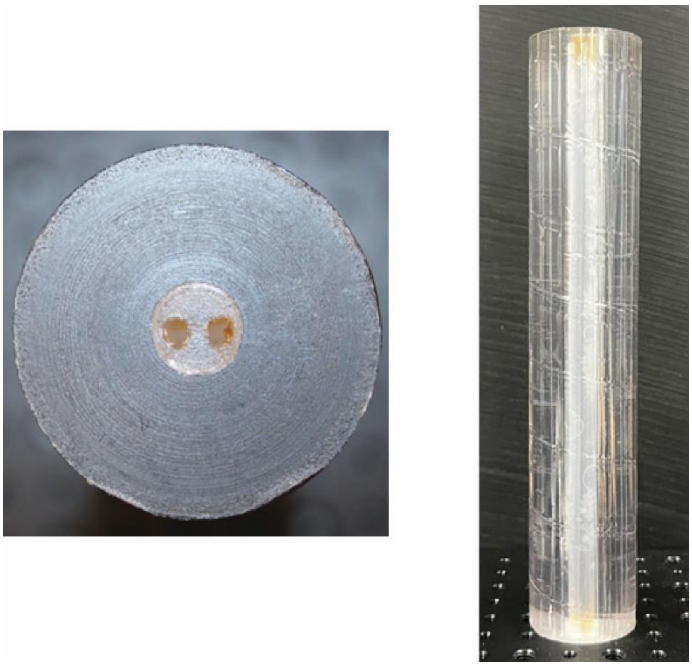

Supplementary Figure 3.1: Photograph of the preform used to fabricate fiber design F2 and F3.

3.2.2 Tetro-DOpE probe characterization

Due to the small cross sectional area of the tungsten electrode (diameter : 15 μm), the impedance of the electrdoes at 1 kHz is ~ 1MΩ. Although action potentials can be reliably recorded with this impedance range[41], lower impendance enables higher signal to noise ratio, which leads to better spike sorting quality. To decrease impedance, we increased the surface area by roughening the electrode surface with silicon carbide polishing film. The cross-sectional image of the polished and roughened electrodes are shown in fig. 3.3a along with the respective spectral impedance measurement. Surface roughening decreased impedance more than two-fold (from ~1.1 MΩ ~0.4MΩ). To demonstrate the flexibility of the probes, the bending stiffness of the thin fibers (design F1 and F2) and tungsten wire (50 μm) were measured with a dynamic mechanical anaylzer. The fiber design F2 has higher bending stiffness than fiber design F1 due to additional tungsten electrodes, which are the least flexible component (i.e., F2 has two electrodes while F1 has one

electrode). To demonstrate the optical delivery capability, a Tetro-DOpE device with the design in fig. 3.2c (ii) (four electrodes and four optical waveguides) were connected to diode-pumped solid-state (DPSS) lasers with various wavelegnths (λ = 635nm, 520nm, 450nm) commonly used in optogenetics. Fig. 3.3c are images from the time-lapse video (supplementary video 1) demonstrating the individual addressability of the optical waveguides. The light transmission is well confined within the optical waveguides as shown in fig. 3.3d. Furthermore, we inserted our Tetro-DOpE probe in 0.6% agarose gel and infused purple food coloring dye to demonstrate drug delivery capability via the microfluidic channel. Dye was diffused into the agarose gel phantom during 5 minutes of dye infusion through the channel (fig. 3.3e). These results demonstrate functional performance of Tetro-DOpE probes.

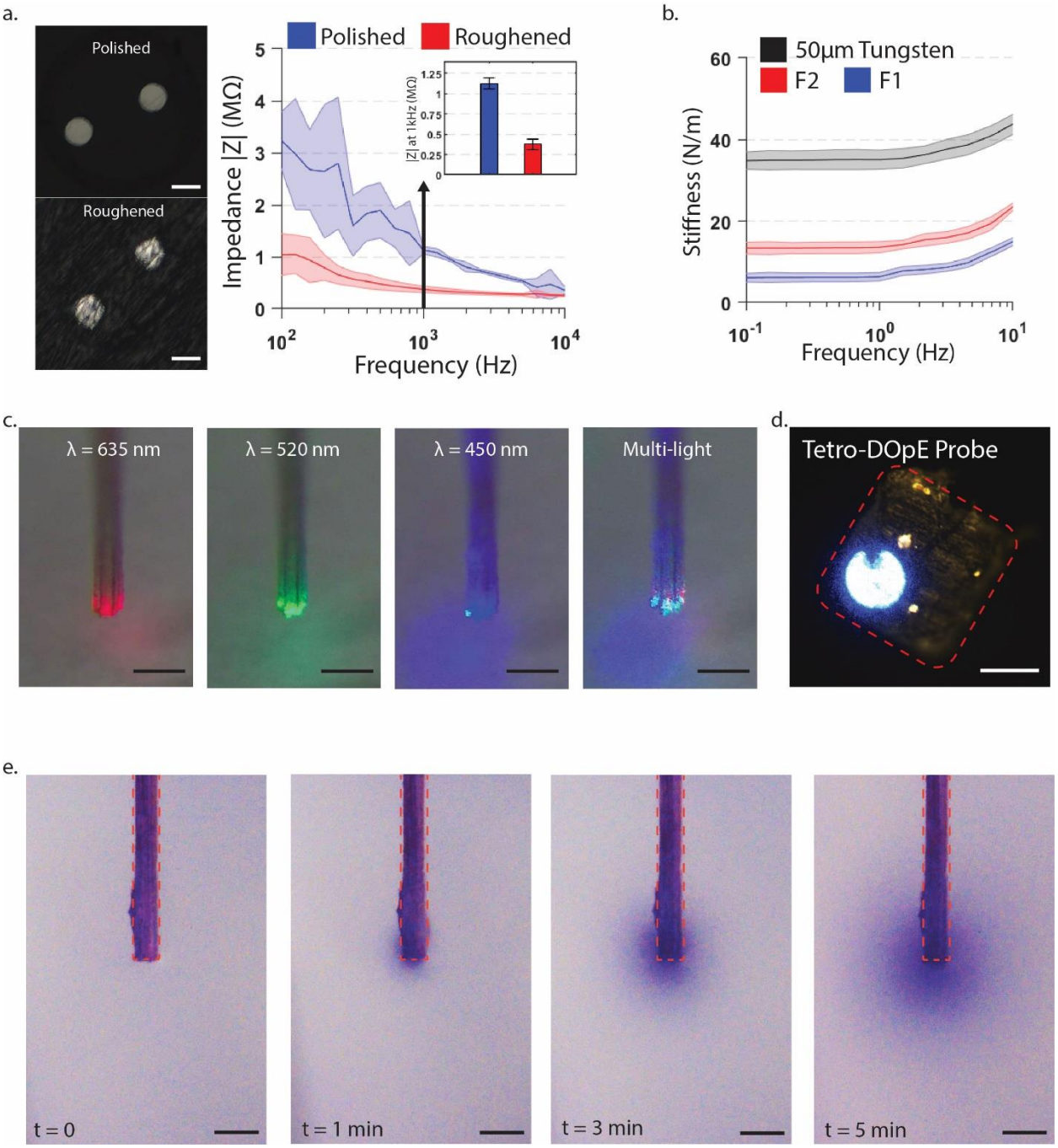

Figure 3.17: a. Impedance measurement of polished and roughened electrodes. **b.** Bending stiffness of fiber design F1 and F2 compared with 50 µm tungsten wire. **c.** Demonstration of individually addressable optical waveguide **d.** Cross-sectional image of the probe with the optical stimulation. **e.** Time-lapsed images to demonstrate the drug infusion using a food coloring at 1nL/s infusion rate in a 0.6% agarose gel phantom.

3.2.3 *In-vivo* validation of Tetro-DOpE probes

To evaluate in vivo function we used tungsten electrodes to obtain electrophyisological recordings using the electrodes, optogenetically manipulated neural circuitry with the optical waveguides, and infused saline using the microfluidic channel. The Tetro-DOpE probes are connected to an Intan recording system using the pin connections, to DPSS laser using optical ferrules and silica fibers, and to WPI micropumps using fluidic connection (fig. 3.4a). An illustration of the experimental set-up is shown in fig. 3.4b with mice running on a wheel in 1-D virtual reality, promoting spontaneous running behavior. The probe implantation was targeted to the hippocampus CA1 pyramidal cell layer (fig. 3.4c). Fig. 3.4d shows an example wideband extracellular recording (0.1- 8000 Hz) in the CA1 of hippocampus. Within the 10-second-window, we observed three individual sharp wave-ripples (SPW-Rs; 150-250 Hz oscillation lasting 50-100 ms), a reliable electroanatomical landmark suggesting proximity to the pyramidal layer of hippocampus CA1.[42-44] Additionally, multi-unit activity (population spiking) is clearly present in the raw trace (fig. 3.4d). By reliably implanting and recording from the targeted region across animals (CA1, n = 8 animals), we demonstrate that our Tetro-DOpE probe can record both multi-unit activity and local field potentials without disrupting the local circuitry. Furthermore, we expressed Channelrhodopsin-2 (ChR2) in CA1 pyramidal cells to validate the optical waveguides in the Tetro-DopE probes. CA1 was optically stimulated at five intensities. Optically evoked changes in neural activity were observed as negative deflections and oscillations in the raw LFP and increased spiking in the 0.3-8 kHz band pass filtered signal fig. 3.4e. Note that at lower power, population depolarization is not visible. The resolution of optical stimulation enables reliable optical induction of SPW-Rs without generating higher-frequency pathological oscillations.[45] With these optogenetic experiments (animal number =3), we demonstrate a high sensitivity in the optogenetic stimulation using our Tetro-DOpE probes. To evaluate the local infusion via the

microfluidic channel, we infused 200nL of saline with a rate of 1nL/s. As expected from the literature,[29, 32, 33] we observed a silence in the spike trace after saline infusion (supplementary fig. 3.2), which is explained by the physical displacement of the cells. Altogether, we successfully demonstrated the *in vivo* functionalities (electrophysiology, optical stimulation, and local infusion) of our novel Tetro-DOpE probes.

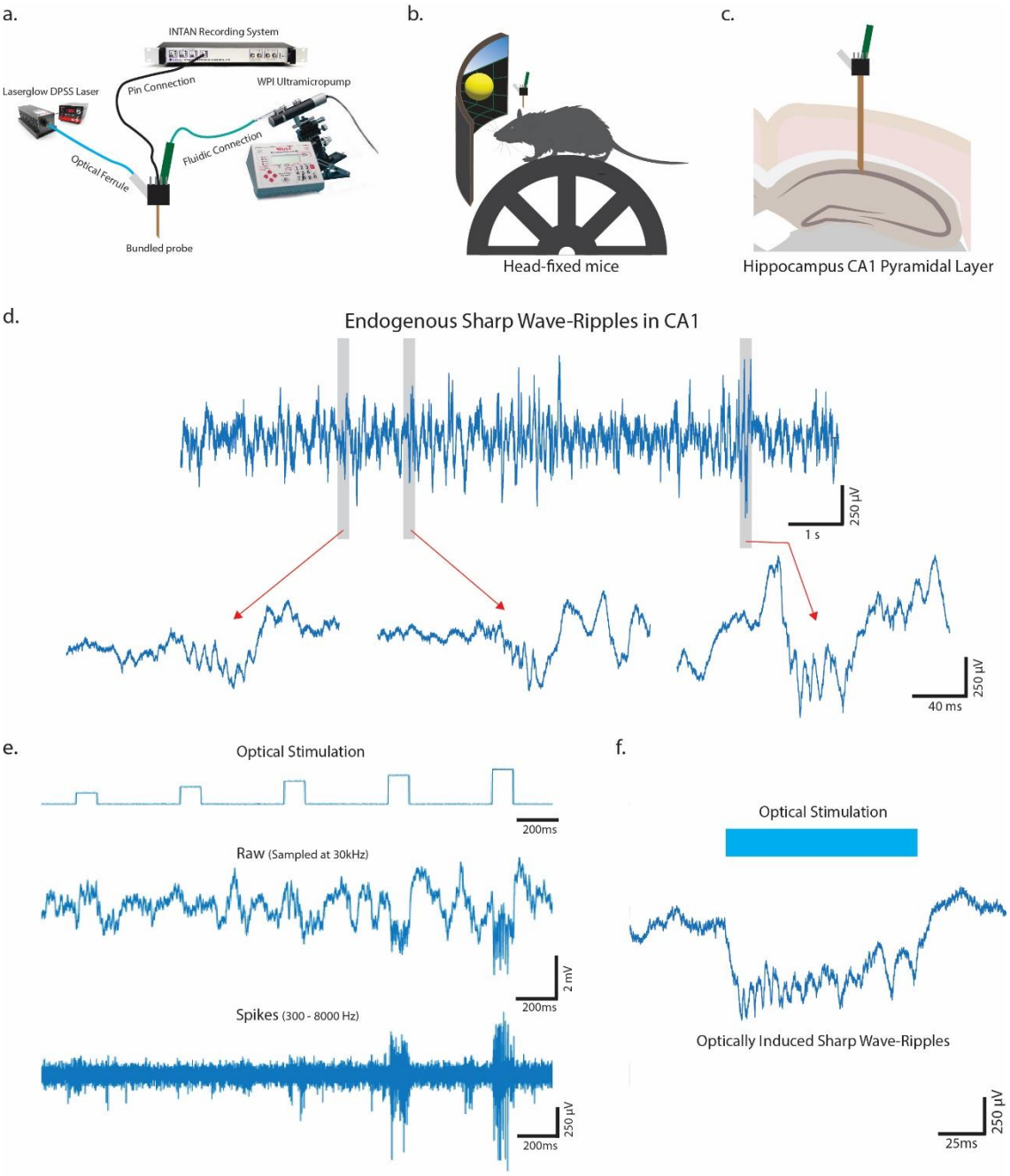

Figure 3.18: **a.** Hardware equipment used in the tri-modality *in-vivo* setup. **b.** Illustration of the mouse setup. A head-fixed, wild-type mouse is mounted on the wheel. A virtual reality environment is presented on the screen to instigate running. **c.** Schematic of the targeted implant site, hippocampus CA1. **d.** Example wideband (0.1 – 8000 Hz) extracellular trace from CA1 recorded using Tetro-DOpE probe. The trace shows three different instances of sharp wave-ripple. **e.** Raw and filtered traces of optically evoked neural responses at various optical stimulation power. Note the different neural responses at single-unit resolution and group depolarization with respect to different optical powers. **f.** Demonstration of optical induced sharp wave-ripples.

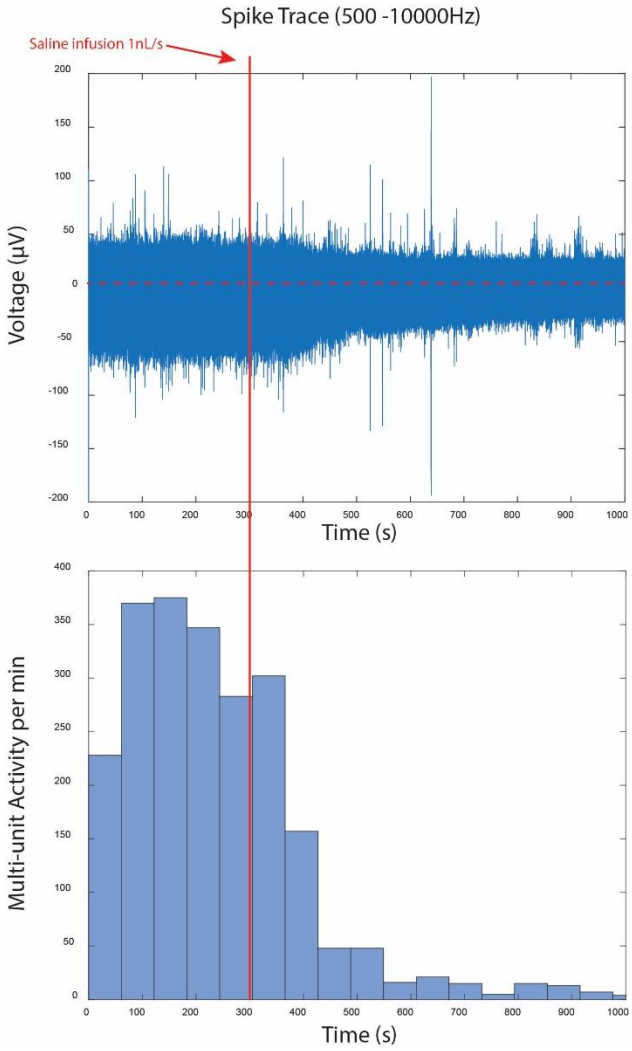

Supplementary Figure 2: The spike trace, filtered from 0.5 to 10 kHz, shows cell displacement due to local saline infusion. The multi-unit activity per min plotted respect to time. Note after the local infusion, the recorded multi-unit activity decreases drastically, also observable in the spike trace.

3.2.4 High Customizability of Tetro-DOpE probes

Unlike the existing multifunctional probes, the Tetro-DOpE probes can easily increase the feature counts by bundling more fibers (supplementary fig. 3.3) or be assembled in specific configurations for the user's need. To illustrate the high customizability of the Tetro-DOpE probe, we adapted the conventional shank configurations of the silicon probes. As shown in fig. 3.5a, the shank configured Tetro-DOpE probes were mounted on a 3-D printed plate with a microdrive[46]

and implanted into the hippocampus CA1 in both side of the hemispheres. The three shanks in each hemisphere are 150 μm apart from one another. All shanks have four electrodes, and the middle shank has light delivery capability. A photograph of the probes epoxied onto the 3-D printed plate is shown in fig. 3.4b. Unlike the silicon probe, the configuration of these shanks can easily be altered via changing the geometry of the 3-D printed plate. For the first time, we reliably recorded with thermally drawn fiber-based probe with 24 electrode sites in a freely moving chronic mouse (fig. 3.5c). Fig. 3.5d shows chronic, raw recording at the electrode sites. We clustered the action potentials using a combination of waveform template and principal component analysis (PCA). From the multi-unit (population activity) we were able to sort a high firing rate CA1 interneuron, shown in fig. 3.5e. The respective auto-correlogram is plotted in fig. 53.f. The PCA of the multi-unit and interneuron clusters are shown in fig. 3.5g. Altogether, the high customizability of the configurations provides a high flexibility in recording sites for future investigation of cross brain regions.

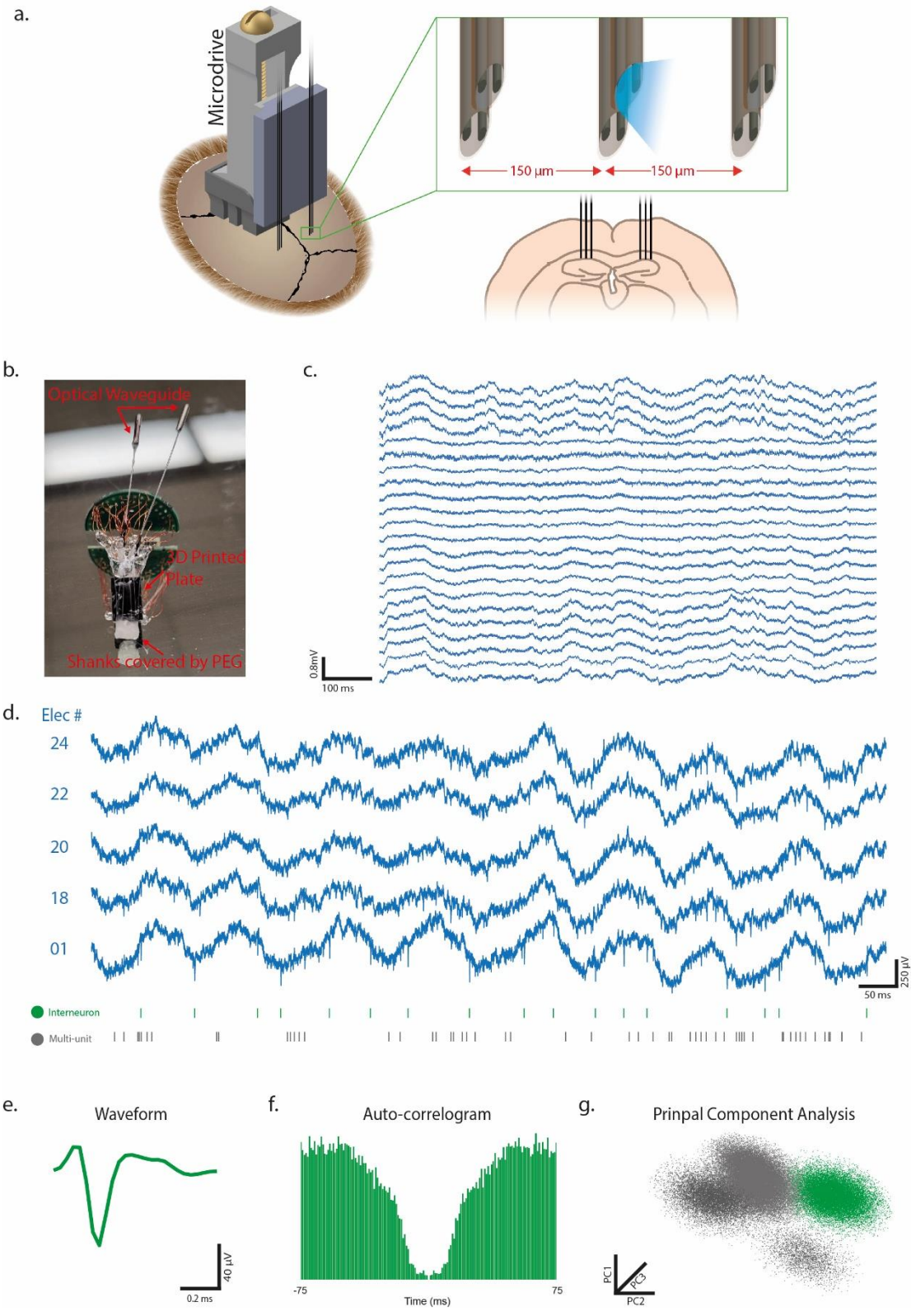

Figure 19: **a.** Schematic of the experimental set up. The Tetro-DOpE probes were assembled into shanks enabling bilateral recording of hippocampus CA1. The assembled probes were mounted onto the microdrive, which is 3d printed with aluminum. **b.** Photograph of the assembled probes

with the PCB, optical ferrules, and 3-D printed plate. **c.** A representative recording from 24 electrodes. **d.** chronic, raw recording at different electrode sites. **e.** waveform of identified unit. **f.** Auto-correlogram of the identified unit. **g.** Principal component analysis of the units.

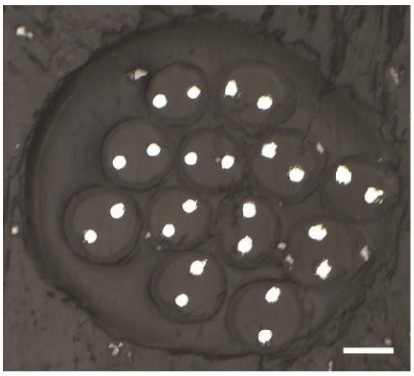

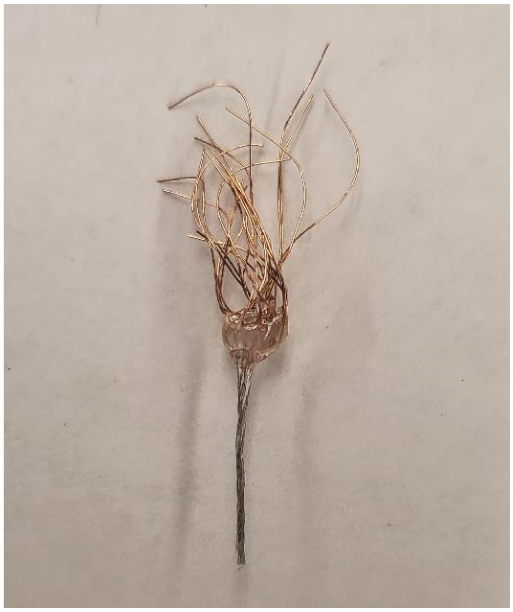

Supplementary Figure 3: Cross-sectional image of twelve multifunctional fibers bundle. The tungsten electrodes are connected to the insulated copper wires, as shown in the photograph. Scale bar: 60 μm.

3.3 Discussion and Conclusion

Here, we fabricated Tetro-DOpE probes by bundling thin multifunctional fibers produced with scalable and low-cost convergence thermal drawing process. The low count of features (i.e., electrodes, optical waveguides, and microfluidic channels) in each fiber enables simple connection to the outside module (i.e., pins, PCBs, ferrules, and tubes). The Tetro-DOpE probes reliably record *in vivo* electrophysiology (i.e., LFP and multi-unit activity), while enabling focal light and drug delivery. We assembled a six-shank Tetro-DOpE device with recording and optical stimulation capabilities to demonstrate the customizability of the probe. The device was mounted on a

microdrive and implanted into the hippocampus, enabling bilateral CA1 recording in freely moving mice.

For most fiber-based sensors, there is a trade-off between the ease of connection and the complexity of the cross-sectional design. Higher counts of electrodes and optical waveguides in a single device would cause an exponentially harder connection. However, connecting one or two electrodes and one other module (i.e., optical waveguide and microfluidic channel) requires a simple connection process. By bundling thin multifunctional fibers (<50 um), we overcome this challenge, where we can fabricate fiber-based devices with higher counts of features, while maintaining the ease of connection. The convergence thermal drawing process enables hundreds of meters of multifunctional thin fibers and can easily be distributed like the insulated wires used for classic tetrode preparation. The material cost of the thin multifunctional fibers is < $2 per meter and could be lowered in industrial operations. During the bundling process, rapid in-house modular customization can be tailored for each experiment, as shown in the six-shank device. Any academic laboratory would be able to connect the features of the probes and bundle the thin fibers to make a Tetro-DOpE probe, just like a tetrode. Altogether, we present flexible, customizable, low cost, and accessible Tetro-DOpE probes.

3.4 Materials and Methods

Preform Fabrication

Preform is the macroscale version of the fiber. The possible materials of multifunctional polymer probes largely consist of thermoplastics, metal, and semi crystalline. All polymer materials (films, tubes, and rods) were baked in 80℃ vacuum oven to ensure no water molecules reside within the polymer. Three various fibers were drawn for this study. However, the second

and third design are the same except that there exists an electrode instead of the microfluidic channel. Since this difference will be accounted in the thermal drawing process, we only designed and fabricated two preforms. For the first design, a PC rod (McMaster-Carr) is milled for the wire to be inserted into during the CTDP. The milled rode is rolled with PC films (Laminated Plastics) and then with PVDF films (McMaster-Carr). After PVDF films, we roll another layer of PC films. The rolled preform is consolidated in a vacuum oven at 190°C. During this process, the films consolidate to form a hard PC and PVDF matrix without any gaps (supplementary fig. 1). For the second design, the procedure is similar to that of the first design except for an additional mill on the other side of the PC rod. The milled PC rod is then rolled with PC films and PVDF films and consolidated.

Thermal Drawing Process

Thermal drawing process requires a specialized thermal draw tower. The preform is mounted onto the preform holder and fed into a custom-built furnace which has three temperature zones. The top zone preheats the preform, the middle zone softens the preform, and the last zone cools down the fiber. After the preform has softened in the middle zone, the bottom of the preform is pulled down via a capstan motor at a controlled manner to fabricate the fiber. The feeding speed of the preform and the pulling speed of the fiber along with the temperature of the furnace controls the final geometry of the fiber. The three temperature zones of the furnace were set to 150°C, 275°C and 120°C respectively. The middle zone temperature, feeding speed and pulling speed were closely controlled to keep the fiber (PC scaffold) at 300 μm.

Convergence thermal drawing process enables multi-material fiber drawing with vastly different thermal behavior. While the fiber is drawn, materials can be fed into the empty channel and clamped. For our fiber design 1 and 2, we used our first and second design of preform

respectively. We fed in 15um tungsten wire (Midwest Tungsten) as the fiber is being drawn. For the fiber design 3, we leave one channel empty, which becomes the microfluidic channel and feed tungsten wire on the other empty channel.

Device Fabrication

The outer PC cladding for the fiber is chemically etched with DCM. Fiber is then cut into ~5 cm segments and connected with corresponding modules (i.e., electrodes to insulated copper wires, optical waveguide to optical ferrules, and microfluidic channel to non-elastic tubing). Then, four fully connected fibers are fit into ~3mm scaffold in a 2x2 structure. The top of the bundle structure is glued together with an optical resin. Then, the scaffold slides down holding the bundle fiber in a 2x2 with some tension. The overall bundle is applied with medical epoxy and the scaffold slides up and down to remove excess medical epoxy. After the medical epoxy cures, the top of the bundle is cut with a razor blade and polished and roughened using a polishing station (Krelltech) at an angle. The copper wires are then connected to either pin connectors or a PCB.

Electrochemical spectral impedance measurement

Impedance measurements were collected via a potentiostat (Gamry Instruments). The measurements were gathered by lowering the sensing end of a fully connected Tetro-DOpE probe into phosphate-buffered saline (PBS, Thermo Fisher). A platinum wire (Basi) was used for a counter and the reference electrode. Finally, we used the Gamry's proprietary software to forward the spectral impedance data.

Headbar Implantation

Mice, mounted in a stereotax, are induced, and maintained at a surgical plane of anesthesia with isoflurane. Hair is removed using hair removal and scalp is disinfected. Then, bupivicaine

nerve block is injected once under the scalp. The scalp is removed with surgical scissors. The skull is cleaned and dried with 3% hydrogen peroxide, followed by application of the sterile dental adhesive Optibond (Kerr Dental; cured with blue light). A < 0.2 mm burr hole is dug above the right cerebellum for a ground wire. A stainless-steel wire is inserted into the burr hole between the skull and the brain, parallel to the brain surface, then the wire is affixed to the skull with sterile dental acrylic. This stainless-steel wire is connected to the ground of the system. A titanium headplate (2 cm long, ~ 1 gram) is positioned above lambda. Then, the plate is positioned parallel to skull and permanently fixed in place with sterile dental acrylic. All protocols and experiments were approved by the Virginia Tech (Blacksburg, VA, USA) Institutional Animal Care and Use Committee (IACUC).

Microdrive Implantation

The Tetro-DOpE probes epoxied onto the 3-printed plate were attached to custom metal microdrives[46] prior to implantation. Surgical procedures for headbar implantation (see above) are followed, with a deviation following the ground wire implantation. A linear burr hole, (using dental drill with 0.2 mm burr bit) just larger than the the probes, is dug above the hippocampus. The microdrive and probe, held by the stereotax, is lowered into the craniotomy 1mm, until the probe is in the cortex just above the hippocampus. The base of the microdrive is then permanently fixed to the skull with sterile dental acrylic. A miniature faraday cage is then constructed and fixed to the skull of the mouse to minimize noise, and the ground wire is attached to the faraday cage. The entire implant is wrapped in vetwrap bandaging tape to protect the animal and implant from damage. Following recovery, the probe is slowly lowered using the microdrive while recording online to identify electrophysiological markers of the hippocampus and neurons. Following each movement of the probe, location is confirmed 24 hours later after tissue relaxes.

AAV Injection

Mice, mounted in the stereotax, are induced and maintained at a surgical plane of anesthesia with isoflurane. Hair is removed using hair removal and scalp is disinfected. Then, bupivicaine nerve block is injected once under the scalp. A < 0.2 mm burr hole is dug above the hippocampus (mm from bregma: −1.8, lateral: 1.5). Glass pipette containing AAV5-CaMKIIa-hChR2(H134R)-EYFP (UNC Gene Therapy Center – Vector Core) is lowered into CA1 (mm from surface: -1.2) at a slow rate. 100nL of AAV (titer: $4.1x10^{12}$ GC/mL) is injected into tissue at a rate of $1nLs^{-1}$ using microinjector syringe pump (WPI: MICRO2T & 504127). Glass pipette is kept in place for 5 minutes for virus to diffuse, then slowly removed from brain. Craniotomy is covered using biocompatible silicon elastomer (Kwik-SIL; World Precision Instruments). Then, the scalp is closed with Vetbond (3M).

Craniotomy

Mice, mounted in the stereotax, are induced and maintained at a surgical plane of anesthesia with isoflurane. A 0.5-1.0 mm burr hole (using dental drill with 0.2 mm burr bit) is dug above the hippocampus. Then, the dura is removed. Biocompatible silicon elastomer (Kwik-cast; World Precision Instruments) is applied to the burr hole to keep the brain from drying.

in-vivo Recording

Mice, habituated to head-fixed navigation, are placed in the head fixation apparatus, and the Tetro-DOpE probe is lowered through the craniotomy into the brain. When SPW-Rs are recognized, the probe is left in place for 30-45 minutes until tissue is relaxed. The amplified neural signals are then recorded with RHD2000 system (Intan Technologies LLC). For freely moving

chronic mouse recordings, the omnetic connector from the PCB was connected to RHD2000 system and the electrophysiology signal was recorded.

Optical stimulation

The optical ferrule from the probe is coupled to a diode-pumped solid-state (DPSS) laser (Laserglow Tehcnologies, 100mW maximum power, wavelength = 473nm.) through a mating sleeve (Thorlabs). The optical output is calibrated each optical stimulation session. The optically evoked LFP activity is closely monitored to determine power output necessary to optically induce SPW-Rs. Across experiments optical power varied between 6-92 μW and optical power density to be 3.1 – 47.3 mW/mm^2.

Data Analysis

Data analysis was performed in Matlab (The Mathworks). Kilosort, spike2, and Matlab custom scripts were written to sort neural spikes and analyze the local field potentials. The extracellular electrophysiology signals were digitally filtered from 0.5–500 Hz and 300–8000 Hz to obtain local field potentials and single unit traces respectively. The spike sorting algorithm was implemented by first filtering out individual spikes using standard deviation dependent threshold. Then, the dimensionality of the spikes were reduced via principal component analysis and individual clusters were identified with K-means clustering.

3.5 Reference

1. Buzsáki, G. Large-scale recording of neuronal ensembles. *Nature Neuroscience* **7**, 446-451 (2004).
2. Carandini, M. From circuits to behavior: a bridge too far? *Nature Neuroscience* **15**, 507-509 (2012).
3. Wang, X.-J. Neurophysiological and Computational Principles of Cortical Rhythms in Cognition. *Physiological Reviews* **90**, 1195-1268 (2010).

4. Buzsáki, G. & Draguhn, A. Neuronal Oscillations in Cortical Networks. *Science* **304**, 1926-1929 (2004).
5. Rubin, A. et al. Revealing neural correlates of behavior without behavioral measurements. *Nature Communications* **10**, 4745 (2019).
6. Yuste, R., MacLean, J.N., Smith, J. & Lansner, A. The cortex as a central pattern generator. *Nature Reviews Neuroscience* **6**, 477-483 (2005).
7. Ekstrom, A.D. et al. Cellular networks underlying human spatial navigation. *Nature* **425**, 184-188 (2003).
8. Hafting, T., Fyhn, M., Molden, S., Moser, M.-B. & Moser, E.I. Microstructure of a spatial map in the entorhinal cortex. *Nature* **436**, 801-806 (2005).
9. O'Keefe, J. & Dostrovsky, J. The hippocampus as a spatial map. Preliminary evidence from unit activity in the freely-moving rat. *Brain Research* **34**, 171-175 (1971).
10. Hong, G. & Lieber, C.M. Novel electrode technologies for neural recordings. *Nature Reviews Neuroscience* **20**, 330-345 (2019).
11. Schultz, W. Responses of midbrain dopamine neurons to behavioral trigger stimuli in the monkey. *Journal of Neurophysiology* **56**, 1439-1461 (1986).
12. Bruce, C., Desimone, R. & Gross, C.G. Visual properties of neurons in a polysensory area in superior temporal sulcus of the macaque. *Journal of Neurophysiology* **46**, 369-384 (1981).
13. Gray, C.M., Maldonado, P.E., Wilson, M. & McNaughton, B. Tetrodes markedly improve the reliability and yield of multiple single-unit isolation from multi-unit recordings in cat striate cortex. *Journal of Neuroscience Methods* **63**, 43-54 (1995).
14. Mokri, Y. et al. Sorting Overlapping Spike Waveforms from Electrode and Tetrode Recordings. *Frontiers in Neuroinformatics* **11** (2017).
15. Emiliani, V. et al. Optogenetics for light control of biological systems. *Nature Reviews Methods Primers* **2**, 55 (2022).
16. Deisseroth, K. Optogenetics: 10 years of microbial opsins in neuroscience. *Nature Neuroscience* **18**, 1213-1225 (2015).
17. Joshi, J., Rubart, M. & Zhu, W. Optogenetics: Background, Methodological Advances and Potential Applications for Cardiovascular Research and Medicine. *Frontiers in Bioengineering and Biotechnology* **7** (2020).
18. Chen, W. et al. The Roles of Optogenetics and Technology in Neurobiology: A Review. *Frontiers in Aging Neuroscience* **14** (2022).
19. Fenno, L., Yizhar, O. & Deisseroth, K. The Development and Application of Optogenetics. *Annual Review of Neuroscience* **34**, 389-412 (2011).
20. Wang, M., Da, Y. & Tian, Y. Fluorescent proteins and genetically encoded biosensors. *Chemical Society Reviews* **52**, 1189-1214 (2023).
21. Ovechkina, V.S., Zakian, S.M., Medvedev, S.P. & Valetdinova, K.R. Genetically Encoded Fluorescent Biosensors for Biomedical Applications. *Biomedicines* **9** (2021).
22. Eunah, K., Mihály, V., György, B. & Euisik, Y. flexLiTE: flexible micro-LED integrated optoelectrodes for minimally-invasive chronic deep-brain study. *bioRxiv*, 2022.2008.2005.503006 (2022).
23. Zhao, Z. et al. Nanoelectronic Coating Enabled Versatile Multifunctional Neural Probes. *Nano Letters* **17**, 4588-4595 (2017).

24. Rubehn, B., Wolff, S.B., Tovote, P., Lüthi, A. & Stieglitz, T. A polymer-based neural microimplant for optogenetic applications: design and first in vivo study. *Lab Chip* **13**, 579-588 (2013).
25. Zou, L. et al. Self-assembled multifunctional neural probes for precise integration of optogenetics and electrophysiology. *Nature Communications* **12**, 5871 (2021).
26. Kim, K. et al. Artifact-free and high-temporal-resolution in vivo opto-electrophysiology with microLED optoelectrodes. *Nature Communications* **11**, 2063 (2020).
27. Zhou, Y. et al. A silk-based self-adaptive flexible opto-electro neural probe. *Microsystems & Nanoengineering* **8**, 118 (2022).
28. Jiang, S. et al. Spatially expandable fiber-based probes as a multifunctional deep brain interface. *Nature Communications* **11**, 6115 (2020).
29. Kim, J. et al. T-DOpE probes reveal sensitivity of hippocampal oscillations to cannabinoids in behaving mice. *Nature Communications* **15**, 1686 (2024).
30. Jeong, J.-W. et al. Wireless Optofluidic Systems for Programmable In Vivo Pharmacology and Optogenetics. *Cell* **162**, 662-674 (2015).
31. Shin, H. et al. Multifunctional multi-shank neural probe for investigating and modulating long-range neural circuits in vivo. *Nature Communications* **10**, 3777 (2019).
32. Yoon, Y. et al. Neural probe system for behavioral neuropharmacology by bi-directional wireless drug delivery and electrophysiology in socially interacting mice. *Nature Communications* **13**, 5521 (2022).
33. Shin, H. et al. Neural probes with multi-drug delivery capability. *Lab on a Chip* **15**, 3730-3737 (2015).
34. Garwood, I.C. et al. Multifunctional fibers enable modulation of cortical and deep brain activity during cognitive behavior in macaques. *Science Advances* **9**, eadh0974.
35. Vöröslakos, M. et al. HectoSTAR μLED Optoelectrodes for Large-Scale, High-Precision In Vivo Opto-Electrophysiology. *Advanced Science* **9**, 2105414 (2022).
36. Ouyang, W. et al. A wireless and battery-less implant for multimodal closed-loop neuromodulation in small animals. *Nature Biomedical Engineering* **7**, 1252-1269 (2023).
37. Sahasrabudhe, A. et al. Multifunctional microelectronic fibers enable wireless modulation of gut and brain neural circuits. *Nature Biotechnology* (2023).
38. Zheng, N. et al. Multifunctional Fiber-Based Optoacoustic Emitter as a Bidirectional Brain Interface. *Advanced Healthcare Materials* **12**, 2300430 (2023).
39. Park, S. et al. One-step optogenetics with multifunctional flexible polymer fibers. *Nature Neuroscience* **20**, 612-619 (2017).
40. Canales, A. et al. Multifunctional fibers for simultaneous optical, electrical and chemical interrogation of neural circuits in vivo. *Nature Biotechnology* **33**, 277-284 (2015).
41. Neto, J.P. et al. Does Impedance Matter When Recording Spikes With Polytrodes? *Frontiers in Neuroscience* **12** (2018).
42. Wilson, M.A. & McNaughton, B.L. Reactivation of Hippocampal Ensemble Memories During Sleep. *Science* **265**, 676-679 (1994).
43. Buzsáki, G. Hippocampal sharp wave-ripple: A cognitive biomarker for episodic memory and planning. *Hippocampus* **25**, 1073-1188 (2015).
44. Buzsáki, G., Lai-Wo S, L. & Vanderwolf, C.H. Cellular bases of hippocampal EEG in the behaving rat. *Brain Research Reviews* **6**, 139-171 (1983).
45. Stark, E. et al. Pyramidal Cell-Interneuron Interactions Underlie Hippocampal Ripple Oscillations. *Neuron* **83**, 467-480 (2014).

46. Vöröslakos, M., Petersen, P.C., Vöröslakos, B. & Buzsáki, G. Metal microdrive and head cap system for silicon probe recovery in freely moving rodent. *eLife* **10**, e65859 (2021).

Chapter 4
Femtosecond Laser Machined Microscale Electroporation Fiber Probes

4.1 Introduction

Electroporation is a biophysical phenomenon where short (microseconds) electrical pulses, which induce high electric fields (thousands of V/cm), are used to introduce nanoscale defects in the cell membrane.[1-3] In regard to the applied pulse parameters, there are two modes of electroporation: reversible electroporation (RE) and irreversible electroporation (IRE). In the case of RE, the nanoscale defects increase the membrane permeability, allowing exogenous materials (i.e., DNA, protein, or large molecules) to be transferred into the cell.[4-7] The defects in the membrane can recover after the treatment, thereby maintaining high cell viability. RE drug delivery enables a lower, nontoxic concentration to be administered compared to conventional drug delivery systems.[7] For example, Electrochemotherapy (ECT) is a branch of RE, where chemotherapeutics, such as bleomycin or cisplatin, are injected with a lower concentration, lowering the side effects of the drugs.[5, 7, 8] Another active RE research is in the DNA, RNA, and protein transfections of cells.[5] Compared to the previous method of viral-mediated gene delivery, RE is less expensive and more efficient in performing transfection.[9, 10] During an IRE treatment, higher magnitude electric fields excessively increases the permeability of the cell, leading to disturbance in the cellular homeostasis and cell death.[11-15] Traditionally, radiofrequency ablation[16], microwave ablation[17], and cryoablation[18] have been used to indiscriminately destroy undesired tissues in the body. IRE has some key advantages over these traditional methods: reduced treatment time, absence of the heat-sink effect, sharp ablation margins, and tissue selectivity.[19] Due to these advantages, IRE was transferred into the clinical trials for prostate cancer treatment in 2010.[20] Recently, it has gained significant traction for the treatment of locally advanced pancreatic cancer

as well as for liver and renal tumors. Although IRE has its advantages, the treatment volume is relatively small, and the procedure is relatively complex, involving the precise placement of a multitude of electrodes. Furthermore, due to nerve excitation during the pulse, a neuroblocker and cardiac synchronization need to be employed. Typically, four electrodes are needed for applications involving tumor ablation. The designs of new and less invasive probes[21, 22] have been proposed to alleviate these issues ranging in applications from cancer therapy to cardiac ablation.

In recent decades, scientists have studied the two modalities of electroporation in vitro and in vivo, resulting in relatively standardized protocols for the procedures.[23] Lately, both single-cell and microscale electroporation have been investigated for several purposes: higher cell viability and transfection rate, faster optimization of DNA or RNA transfection procedures, smaller volumes of samples, experiments with rare and expensive drugs, and cell selectivity.[24-26] Future works in the ablation of epilepsy and/or seizure focal points require sharp microscale ablation zones and cell selectivity.[26] Currently, the two main types of microscale electroporation devices are microcapillary[27-29] and microchannel[30-34] based devices. Microcapillary-based devices contain and electroporate the samples in the disposable reaction chambers (usually in pipettes).[35] Microchannel-based devices manipulate the location of the samples through fluidic pumps and microchannel geometries.[36] However, these two types are not adaptable for in vivo experimental environments.[26] Recently, a glass fiber microprobe has been developed for microscale electroporation of arbitrarily selected groups, proposing the possibility of a simplified in vivo experimentation.[37]

In vivo transfection of mice brain through electroporation has been studied.[38-41] Yet, many of the in vivo microscale electroporation devices are restricted to the use of pipettes with

microelectrodes, which have disadvantages of bulky setups. Fiber-based probes have advantages in the scalability (thousands of devices with one thermal draw) and the consistency of device parameters (electrode separation distance) compared to the traditional in vivo microscale electroporation devices (pipettes with microelectrodes). The probes are also minimally invasive, requiring only a microscale burr hole for intracranial insertion. Deep brain regions (i.e., hippocampus, hypothalamus, amygdala, etc.) may be electroporated to eliminate or transfect desired neurons with minimal damage along the electrode insertion track. The hippocampi of rodents are roughly 20~30 mm^3 and the identified layers within hippocampi, such as Dentate gyrus or CA3, are in several mm^3 ranges.[42, 43] Currently, electrical (relatively low voltage compared with electroporation), chemical, and optical stimulations are the main sources of neuron manipulation used to understand the brain circuitries. For example, picosecond electrical pulses (500ps, 10kV/cm) were recently reported to suppress action potentials in hippocampal CA1.[44] Pulsed electric fields elicit transient blood-brain barrier (BBB) disruption (up to 72 hrs) at relatively low electric fields (~100 V/cm).[45, 46] The electric fields generated using these minimally invasive fiber-based probes lend this approach as suitable for inducing neurological phenomenon with minimal damage to intact tissue. With microscale electroporation as an additional tool to manipulate neurons, further advancements in understanding the neuronal circuitries may be possible.

The thermal drawing process (TDP), traditionally used to fabricate the optical glass fibers[47], is an emerging platform for developing multimaterial fiber-based micro-devices.[48-54] The method is highly versatile, enabling the assemblage of various functional materials in a complex cross-sectional design.[48] The unique cross-sectional architecture leads to new innovations in fiber-based micro-devices and advanced textiles for sensing, actuating, biomedical applications, and energy harvesting. From a single inexpensive preform, fibers of hundreds of meters in length are produced,

thus reducing the cost and the time of the fabrication.[48] Recently, a new class of multifunctional neural probe has been developed using this method, enabling simultaneous electrical recording, drug delivery, and optical and electrical stimulation in vivo.[54, 55] Information, such as temperature, can be stored and processed in our daily clothing that has digital electronics embedded fibers woven in.[55] Flexible and disposable fiber has recently been designed to sense the microfluidic activities, such as the presence or the flow rate of a fluid.[56]The microfiber probes fabricated with the TDP method show promising prospects in biomedical applications. Machine Currently, the functions of the flexible fiber-based neural probes are mostly realized locally at the tip.

We developed a new polymer fiber-based microprobe using the scalable thermal drawing process, enabling localized microscale electroporation and drug delivery at the center of the electroporation region. We exposed the electrodes and the microfluidic channel at various locations along the fiber length using a femtosecond laser micromachining technique. With two phases (source and sink) fabricated into a single fiber, pulses could be delivered with one insertion, reducing the complexity in electrode placements. The size of the microscale electroporation is customizable by adjusting the spacing between the electrode exposures and the pulse parameters. To demonstrate the two modes of electroporation, we delivered electrical pulses to a 3D collagen hydrogel scaffold in which human glioma cells (U251) were seeded. Then, RE or IRE area was determined by fluorescent staining. Numerical simulation was performed to estimate the electric field distribution in the scaffold and determine the electric field thresholds of IRE. Our data suggest that the newly developed class of fiber-based microscale electroporation devices has the potential in conducting in vivo microscale ablation/ transfection experiments where the traditional microchannel and microcapillary-based devices had difficulties.

4.2 Results and Discussion

4.2.1 Thermal Drawing Process

Two varieties of the fiber were fabricated using the TDP method for microscale electroporation (Figure 4.1). Due to the high electrical voltage during the electroporation, we utilized polycarbonate as the insulating medium of the fiber device for its high dielectric breakdown voltage (200 kV/cm). Thin films of PC were baked in an oven vacuum for 7 days to remove the water inside. In this way, undesirable, random pores will be avoided in the fiber during the thermal drawing process. As shown in Figure 4.1a, a preform was fabricated by rolling, consolidating, and milling. After each rolling of PC films, the intermediate preform was put in a vacuum oven to remove the air in between the film layers and therefore consolidated. The preform was mounted in the 3-layered temperature controllable furnace for the fiber productions (Figure 4.1b). The four spools of copper wire fed the wires from the top of the preform to the bottom of the fiber. The TDP process was closely monitored through the temperature sensors, the strain sensor, and laser micrometer. We controlled the diameter of the fiber by adjusting the temperature of the furnace and/or the drawing speed of the fiber. The diameter of the fiber was reduced by 40~60 folds while maintaining the cross-sectional features of the preform.

In a typical draw, we can obtain a fiber of several hundred meters (Figure 4.1c). In Figure 4.1d, the flexibility of the fiber is demonstrated by wrapping the fiber around a conventional pen. The cross-sections of the two varieties of the fiber are shown in Figure 4.1e and f, respectively. The diameters of the fibers and the copper wires are 398 ± 17 μm and 80 μm. The diameter of the microfluidics channel in the second design is 27 ± 8 μm. The edges of the rectangular grooves are maintained in the fiber. By these copper electrodes alone, microscale electroporation of arbitrarily selected cell groups can be achieved at the tip of the fiber, similar to the previously reported glass

fiber probe. However, there is a limitation in the size of the electroporation due to the fixed distance of the two electrodes at the tip. New sets of preform fabrication and thermal drawing need to take place for various distances between electrodes. We overcame this challenge by implementing a femtosecond micromachining technique along the fiber length to enable distributed functional sites, eliminating the labor demanded to fabricate various electrode distances for different sizes of microscale electroporation.

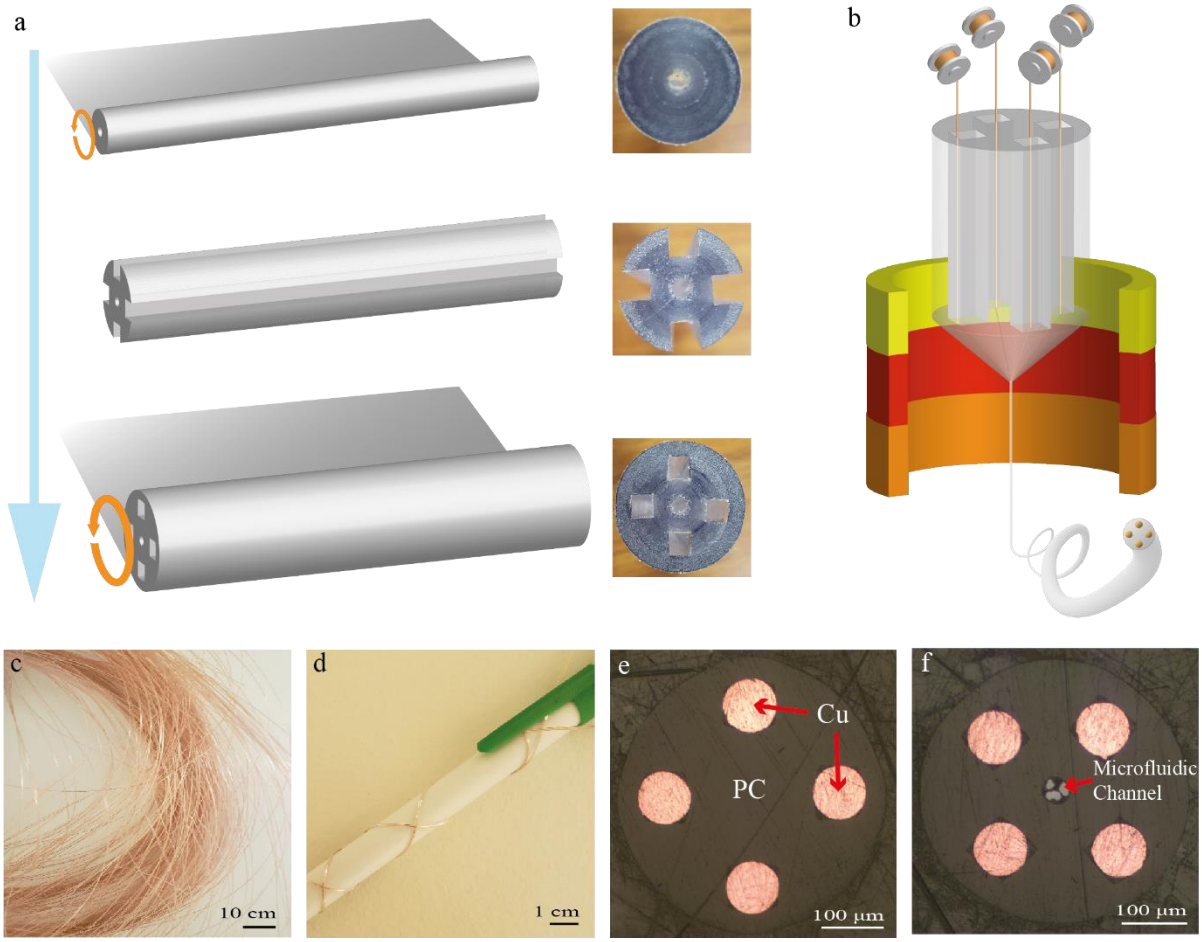

Figure 4.20: Thermal Drawing Process of the Fiber-based Microprobe. a A representative preform fabrication process and the corresponding preform cross-sections. b A schematic of the thermal drawing process of the fiber. c A single thermally drawn fiber with the length of over 300m. d A demonstration of the flexibility of the polymer fiber. e, f A cross-section of the fiber with four copper electrodes with and without microfluidic channel.

4.2.2 Electrode Exposure and Microfluidic Windows through Femtosecond Laser Micromachining

To expose the electrodes and the microfluidic channel along the fiber length, we adapted a custom femtosecond laser setup. The schematic and the picture of the laser setup are shown in Figure 4.2a. The system is fully controlled with custom LabView panels, enabling precise manipulations of the fiber in x, y, z, and rotational directions. We investigated the optimal laser parameters and the fiber orientations for the various sizes and depths of the exposed electrodes and microfluidic channels. In Figure 4.2 b,c, we show the before and after the femtosecond micromachining technique along the fiber length. We observed black dust or residues of PC around the exposure, similar to the residual melt from cutting PC using a CO_2 laser.[59] The depth required to expose the electrode was 30 ~40 μm; this depth is directly proportional to the preform dimension. We experimentally determined that 0.6 μJ for the pulse energy cut deep enough to expose copper electrodes. The quality controls of the exposed electrode were conducted in the following manner. We covered the tip of the fiber probe with a medical epoxy. Then, we measured the impedance of the exposed electrode using a potentiostat (Interface 1010E, Gamry Instruments) in phosphate-buffered saline (PBS, Thermo Fisher). We observed a high impedance when the micromachining did not expose copper electrodes because PC and epoxy are electrically insulating material. Statistically, roughly 5% of the exposed electrodes with the pulse energy of 0.6 μJ were still covered with PC. This is due to the slight irregular thickness of the electrode covering the PC layer. We utilized Zygo Newview 8200 with a 10x Mirau objective to capture the 3-dimensional features of the exposed electrode (Figure 4.2e). As shown in SI (video), the laser cuts layer by layer from the top to the bottom of the electrode exposure. We grooved a 30 x 100 μm rectangular window, which connects the microfluidic channel to the outside. The cross-section of the exposure is shown in Figure 4.2f. To cut narrow and deep into the microfluidic channel, we employed 1 μJ for the

pulse energy and rectangular micromachining at 6 different depths. Two criteria of the orientation had to be met in order to have a successful microfluidic window. The laser had to point into the center of the microfluidic channel, and the angular orientation of the fiber had to be closely manipulated such that the two electrodes are equidistant from the laser location. In Figure 4.2g, we present our flexible, fiber-based, microscale electroporation probe. The tip of the fiber is mechanically and electrically insulated with a medical epoxy, allowing no drug to be delivered and/ or any microscale electroporation at the tip. For this specific fiber probe, we exposed two 50 by 200 μm electrode windows, roughly 1mm apart. 400 μm below the first electrode exposure, we fabricated a 30 by 100 μm microfluidic window. By exposing different dimensions and changing the distance between the electrode exposures using the femtosecond laser micromachining, we can achieve various microscale electroporation sizes. Additionally, there is no limit to the number of exposures on the same electrode, possibly introducing multiple microscale electroporation along the fiber length. The two unused electrodes may be exposed to a more dynamic electric field (microscale electroporation shapes) or measurements (impedance changes). In Figure 4.2h and SI, we demonstrated local drug delivery near the microfluidic channel by injecting a purple dye. The video (SI) displays no leakage of dye at the tip or along the fiber length.

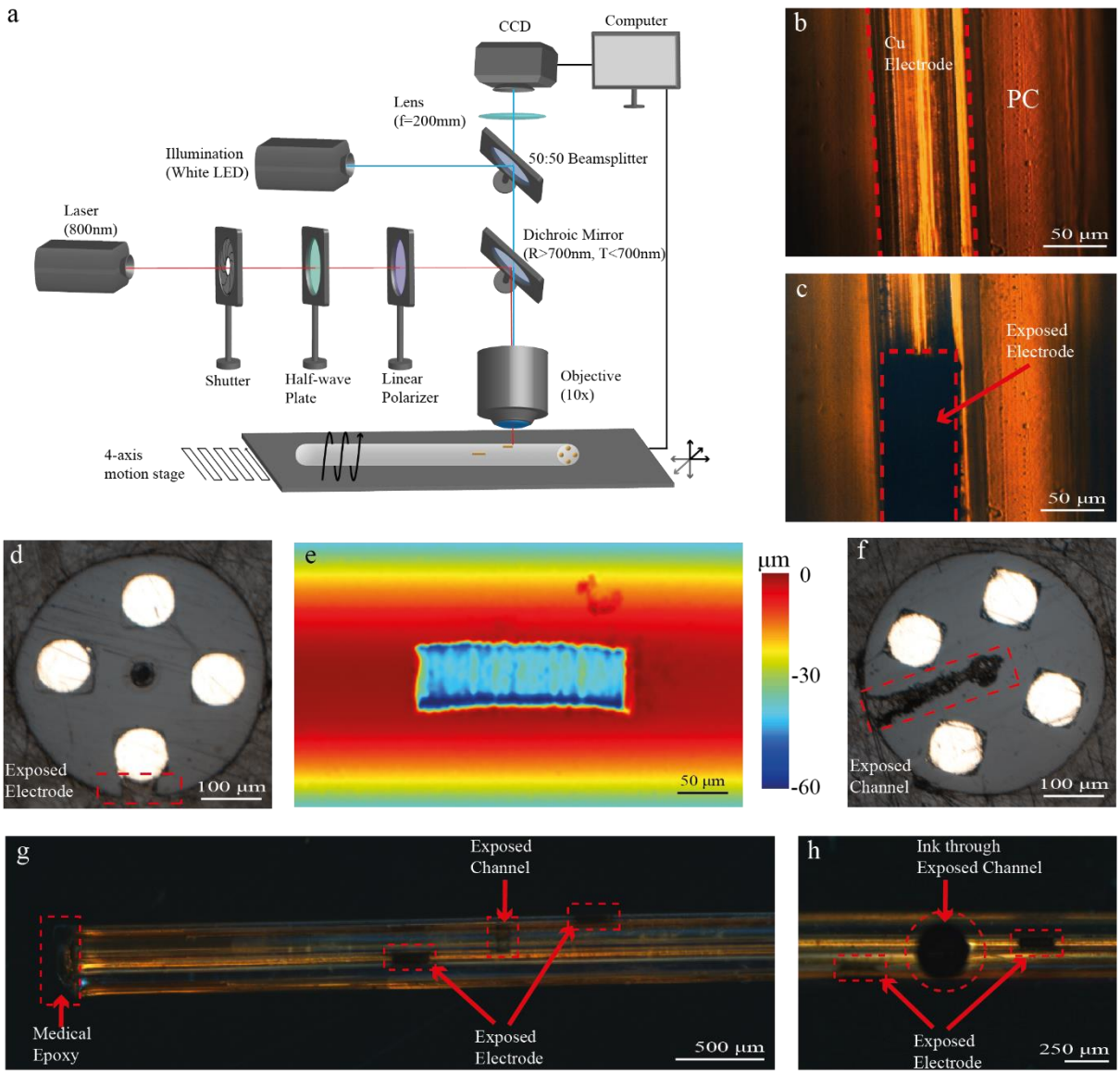

Figure 4.21: Femtosecond laser micromachining techniques along the fiber length. a A schematic of custom femtosecond laser setup to expose electrodes and the microfluidic channel. b,c An image taken by the CCD from the laser setup before and after the micromachining. Black dust and PC residues are visible after the laser micromachining. d A cross-section of the fiber with an exposed electrode. e A profiling image to show the 3-dimensional features of the exposed electrode. There is a 50 x 200 µm rectangular exposure with a depth of 40~ 60 µm. f A cross-section of the fiber with an exposed microfluidic window. The dimension of the rectangular exposure is 30 x 100 µm with a depth of ~ 200 µm. g An image of the fiber-based microprobe for microscale electroporation. The tip of the fiber is mechanically and electrically insulated with medical epoxy. The two electrodes are exposed for electroporation and an exposed channel for drug delivery. h A demonstration of the drug delivery using ink.

4.2.3 Numerical Simulation of Microscale Electroporation

The geometry of the setup is shown in Figure 4.3a. Only half of the collagen scaffold is presented to display the position of the fiber in the hydrogel. The exterior boundaries are electrically and thermally insolated. Two exposures of the fiber electrode are set to source (φ=V) and sink (φ=0) phases, respectively. Figure 4.3b shows the angular orientation of the fiber probe with respect to the scaffold. To easily visualize the positions of the two exposed parts, we only show a quarter of polycarbonate (grey part) in Figure 4.3b. In the actual fiber device, the polycarbonate fills the whole void as insulating and support layers of the four electrodes. The two small windows that connect the collagen and the electrode represents the exposed electrodes. There was a concern in the distribution of the electric field and the electroporation region due to the thinness of the hydrogel and the orientation of our fiber probe. Depending on the orientation of the probe, the relative positions of the top and bottom boundaries of the hydrogel to the exposed electrodes could affect the electric field distribution. We investigated the electric field and the temperature distribution with respect to the angular orientation of the fiber probe. The angle between the upper exposure and the vertical plane, θ, is investigated at 0, 30, 45, 60, and 90 degrees.

Figure 4.3c and d show the respective electric field and temperature distribution at the center plane of the collagen layer for various θ. At the center plane of the scaffold, the electric field and the temperature distributions differ with respect to the probe angular orientation. Since the electric field distribution directly influences the electroporation region, the orientation of the fiber probe (exposed electrodes) has to be consistent for each well, or else the ablation region at each depth for different wells will not agree. The temperature distribution results show that the maximum temperature rises only by 2 ℃ for the irreversible electroporation parameters. Hence,

the ablated area formed in hydrogel experiments is mainly caused by irreversible electroporation rather than thermal damage.

The ablation volumes for different rotations of the fibers are given in Figure 4.3e. The irreversible threshold, 450 V/cm, was obtained by matching the calculated ablation volume to the volume surrounded by the electric field isosurface and comparable to the previously reported values[57, 60]. We observed no large fluctuations in the final ablation volumes at various angular orientations of the probe. The electric field distribution at different layers for $\theta = 0°$ is shown in Figure 4.3f. Due to the configuration of the two exposed electrodes, the ablation areas at different layers are inconsistent. This makes it difficult to determine the electric field by matching the area between the simulation and the numerical results; thus, we used the ablated volume to calculate the electric field threshold.

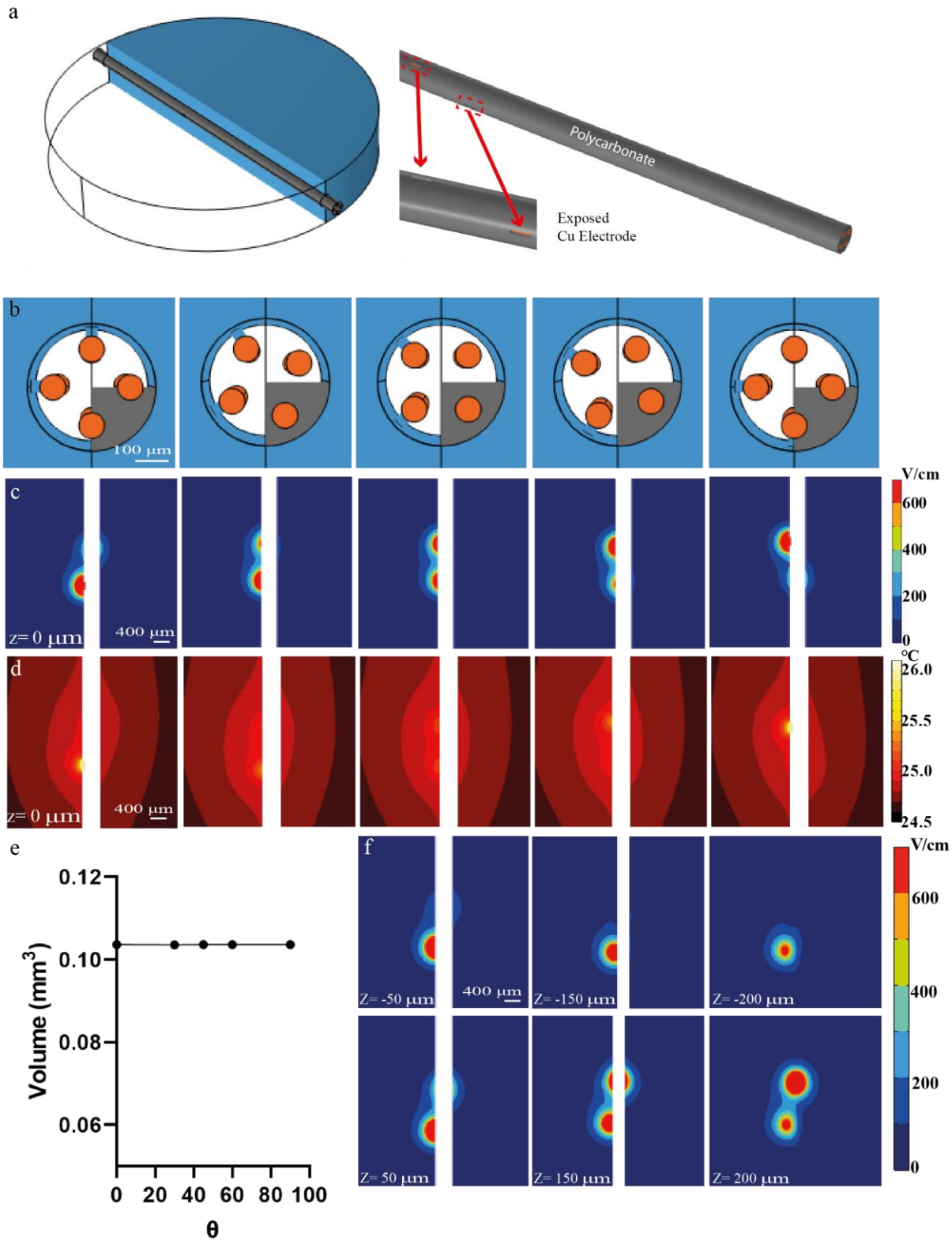
a
Polycarbonate
Exposed
Cu Electrode
b
100 µm
c
z= 0 µm
400 µm
V/cm
600
400
200
0
d
z= 0 µm
400 µm
°C
26.0
25.5
25.0
24.5
e
Volume (mm3)
0.12
0.10
0.08
0.06
0 20 40 60 80 100
θ
f
Z= -50 µm
400 µm
Z= -150 µm
Z= -200 µm
Z= 50 µm
Z= 150 µm
Z= 200 µm
V/cm
600
400
200
0

Figure 4.22: Numerical Simulation of the Electroporation Effects Using the Fiber-based Microprobe. a The geometry of the 3D scaffold (only half presented here) and the fiber-based microprobe. Enlarged detail of the fiber and the exposed copper wire on the right model. b The schematic of the fiber probes placed with different angles to the vertical directions (from left to right, θ=0, 30, 45, 60, and 90 degrees). Only a quarter of the polycarbonate in the fiber is presented to better visualize the exposed places of the fiber. The blue substance outside the fiber is the 3D hydrogel scaffold. The exposure is visible between the 3D hydrogel scaffold and the copper wire. c,d The electric field and temperature distributions at the middle plane of the 3D scaffold for different angles (from left to right, θ=0, 30, 45, 60, and 90 degrees). Pulse parameters used were: 200, 500 V,100 μs, 1Hz pulses. e Ablation volume for the fiber probes with different angles to the wells (θ=0, 30, 45, 60, and 90 degrees as shown in b). The irreversible electroporation threshold was 450 V/cm. f The electric field distributions at different planes when θ=0. Z=200 and -200 μm are the planes tangent to the upper or nether side of the fiber. Pulse parameters used were: 200, 500 V,100 μs, 1Hz pulses.

4.2.4 In Vitro Microscale Electroporation

Electroporation experiments were performed in a 3D hydrogel scaffold in which malignant glioma cells U251 were seeded to demonstrate the feasibility of the fiber electrodes in electroporation application. The experiment setup is shown in Figure 4.4a. Treatment pulses were generated by the pulse generator and recorded through an oscilloscope. Although the simulation showed no ablation volume changes with respect to the angular orientations of the probe, we consistently placed the fiber probe with $\theta = 0°$ to obtain consistent images. Each fiber was immersed in the hydrogel scaffold with a thickness of 1.5 mm. After the study of the control group, we concluded that the 1.5 mm thickness of the hydrogel in the scaffold did not have a large effect on the cell viability. A typical pulse waveform is shown in Figure 4.4b. The amplitude of the clean voltage waveform was 500V. We observed a consistent spike at the onset of the current waveform, followed by some noise throughout the pulse on-time. This could be caused by the relatively low current value.

First, we employed this setup to test the reversible electroporation effect. Pulse parameters were set to 100 pulses with a pulse width of 100 μs, a pulse amplitude of 300 V, and a repetition

rate of 1 Hz. Before treatment, the 3D scaffolds with cells were dyed by YO-PRO-1 and Calcein red AM. Treatment pulses were applied 30 minutes after the staining. Each well was imaged immediately after the treatment. The unaffected cells presented red fluorescence, indicating live cells with an intact membrane structure. The dissipation of red fluorescence or the expression of green fluorescence is an index of electroporation of membranes, as shown in Figure 4.4c. The dark band beside the electroporation zone is the position of the fiber. This is a pilot study to validate that the fiber electrodes proposed here can create effective reversible electroporation.

To further validate the stability at a higher pulse dose for irreversible electroporation, we increased the pulse parameters to 200, 100 μs, 500 V, 1 Hz pulses. The hydrogel scaffolds were dyed with Propidium Iodide (PI) and Calcein green AM 24 hours after pulsing to assess the irreversible electroporation effects. Green fluorescence (Calcein green) indicates live cells, while red fluorescence (PI) stands for the dead cells. Figure 4.4d is a typical image showing the ablation results at a certain plane. The dark band across the well is the position of the fiber. The ablated area with red fluorescence beside the fiber can be identified. For the traditional two-needle electrode configuration, the ablation regions at different planes are similar. However, the ablation regions of the fiber probe at different planes cannot be comparable due to the different electrode configurations. A z-stack scanning (with a step of 5 μm) of the ablated area was used to obtain the ablation area at different planes, as shown in Figure 4.4e. A time-lapsed video of the z-plane scan is included in the supplementary information to aid the visualization of the 3d ablation volume. As to the simulation results in Figure 4.3f, it was challenging to find the exact z-plane of ablation from the fluorescent images due to the small ablation size and the uneven distribution of the cells. However, we observed that the experimental results (Figure 4.3f) match the simulation results (Figure 4.4e) at multiple z-planes (e.g. from Z= 150 μm to Z= 200 μm, at Z= -50 μm, and at Z=

50 μm). These results demonstrated the feasibility of producing microscale irreversible electroporation using the developed fiber electrodes.

We implemented the covariance error ellipse method to estimate the area of ablation at each plane. The ablation volume was estimated by integrating the elliptical area over the height through which we did the z-stack scanning. A custom Matlab script was written to input the images and output the equation and the area of the ellipses. The output covariance error ellipses were layered on top of Figure 4d,e. The average area of the specific ablated region at each plane was 0.241 ± 0.05 mm^2, and the volume was $0.1099 mm^3$. The area of each plane can differ drastically with respect to the angular orientation of the fiber probe.

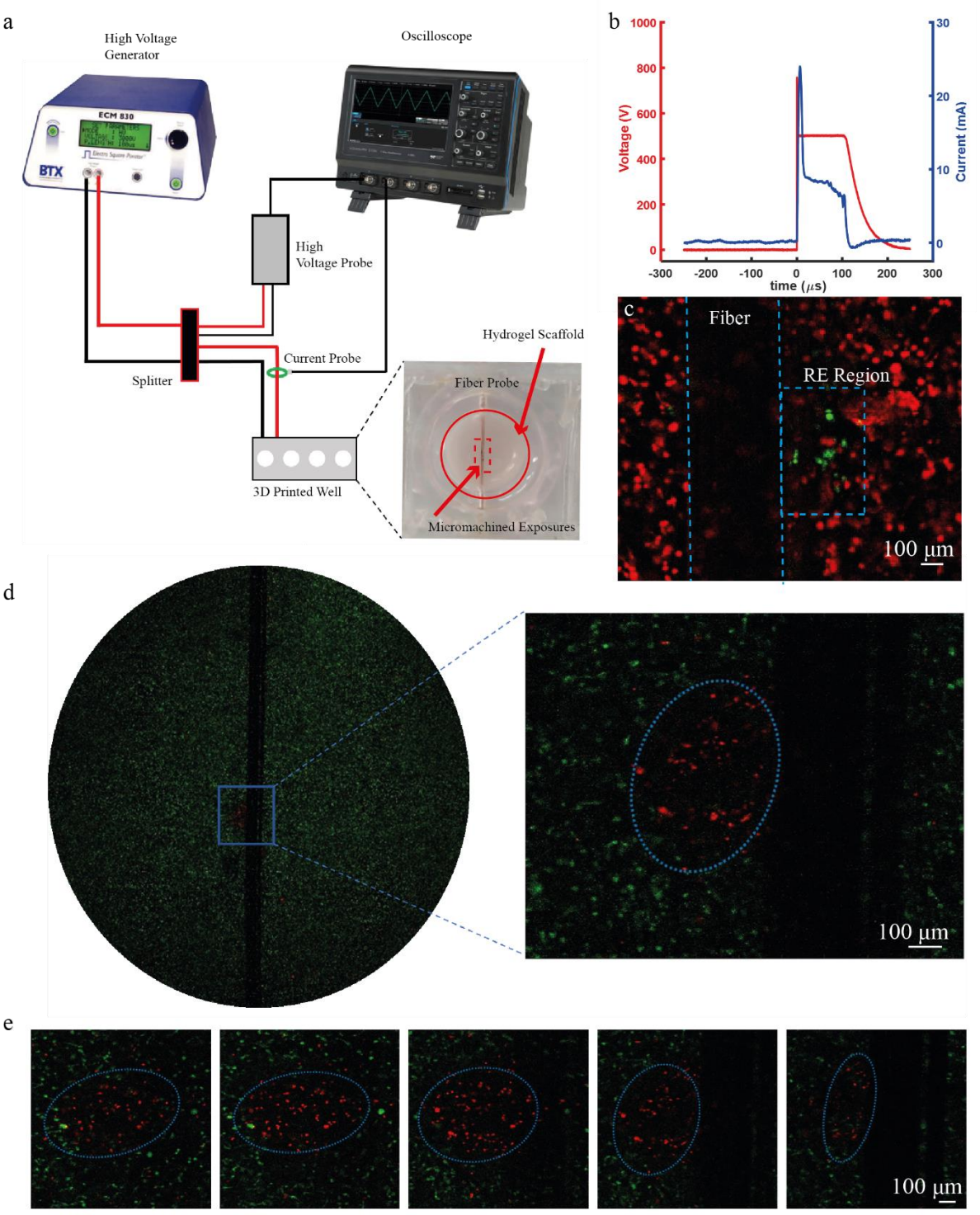

Figure 4.23: Electroporation Experiments Using the Fiber-based Microprobe in 3D Collagen Scaffold with Malignant Glioma Cells U251. **a** The experimental setup. **b** A typical voltage (500 V, 100 μs) and current waveforms. **c** A representative image of the reversible electroporation region indicated by the YO-PRO-1 (green) surrounded by live cells indicated by Calcein red AM (red). **d** A representative image of irreversible electroporation area indicated by the Propidium Iodide (red) surrounded by live cells indicated by Calcein green AM (green). The dark band

beside the ablation area is the position of fiber. **e** A representative image of irreversible electroporation area at various depths. The blue dashed ellipses layered on the ablation regions are the estimated boundary calculated with the covariance error ellipse method.

4.2.5 Customization of the Electrode Exposures

One key advantage of our fiber microprobe compared with the previously reported glass fiber probe is the customization of the electrode exposure sizes and the separation distance between the electrode exposures. The exposure size and the separation distance directly contribute to the electric field; thereby, the customization enables the manipulation of the microscale electroporation size and shape. We exposed the fiber electrodes in four unique designs to demonstrate the customization flexibility, shown in Figure 4.5. The first design consists of two side-by-side electrode exposures. The second design has two exposures on the same electrode while only one exposure on the adjacent electrode. The dimension of the exposures is 50 x 100 μm. In the third design, we changed the dimension of the exposure from 50 x 100 μm to 50 x 400 μm. Lastly, we exposed all four electrodes, keeping the parallel electrodes on the same plane. In Figure 4.5b, the corresponding simulation setup of the designs are presented. The hydrogel experiments were not further conducted because we expect the numerical simulations to reflect the experimental ablation shape, as discussed in the previous section.

With the same parameters from the hydrogel experiment, we simulated and calculated the ablation volume for each design (Figure 4.5c). The calculated ablation volumes from the first to the fourth design were 0.097, 0.106, 0.069, 0.090 mm^3.

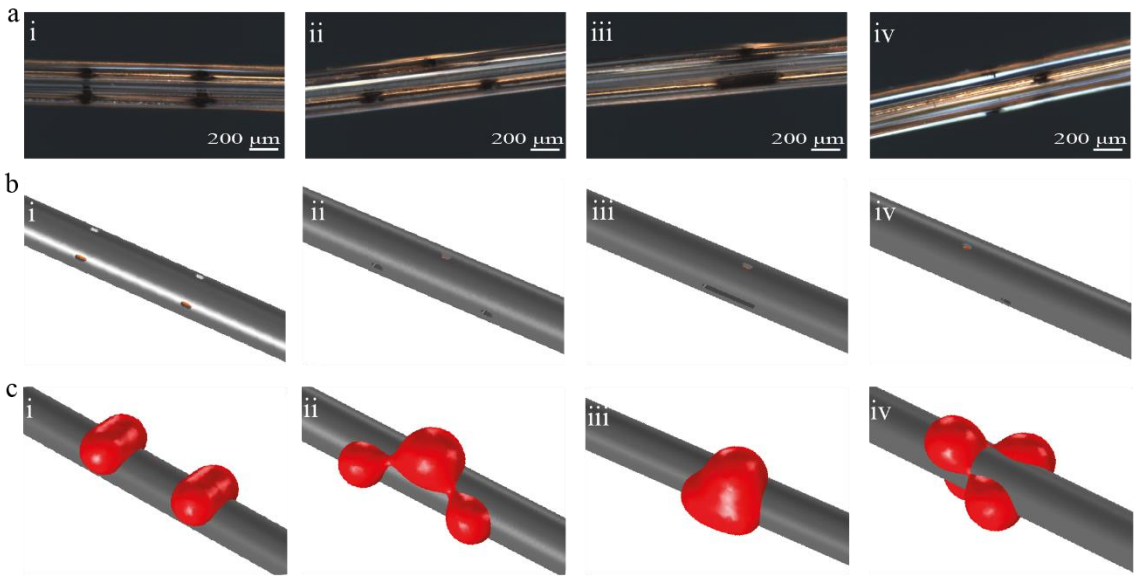

Figure 24: Ablation area control by customizing electrode exposures. **a** Femtosecond machined exposures along the fiber length. **i** Two side-by-side electrode exposures along the fiber length. **ii** Two exposures on one electrode and one exposure on the adjacent electrode. **iii** Side-by-side electrode exposures with different sizes. iv Four exposures from each four electrodes. **b** The corresponding simulation setup for each electrode exposure configuration. **c** The corresponding simulated ablation volumes for microscale irreversible electroporation applications.

4.3 Conclusion

Here, we present a novel device for microscale electroporation of cells through developing a flexible, polymer, fiber-based microprobe for both in vitro and in vivo experiments. The electrodes and the microfluidic channel were exposed along the fiber length through a custom-built femtosecond laser micromachining setup. The different electroporation sizes and shapes were realizable through customizing the electrode exposure sizes and distances between the exposures. We computed the numerical simulations to visualize the electric fields and the temperature distributions of the functioning microprobe at different angles. To validate the feasibility of the proposed fiber electrode in electroporation, we designed a 3D hydrogel scaffold, where the malignant glioma cells (U251) were seeded, and the fiber probe was placed in the middle. The two

modes of the microscale electroporation were conducted, varying the number and voltage of electrical pulses. The reversible and irreversible electroporation areas were observed by fluorescent staining. The ablation volumes were estimated by integrating the area, estimated with the covariance error ellipse method, over the height. The in vitro experiments and the numerical simulations demonstrate the microscale electroporation through our fiber microprobe. Compared with the current microscale electroporation devices, the fiber-based microprobes enable arbitrary control of cell selectivity and more systematic in vivo experiments, such as unrevealing the mysteries in the deep intercortical circuitries.

4.4 Materials and Methods

Preform Fabrication and Thermal Drawing Parameters

The thermal drawing process is a versatile fabrication method that allows thermoplastics (such as elastomers, acrylic, polypropylene, polyvinylidene fluoride, polycarbonate, polysulfone, polyetherimide, etc.) to be pulled into a fiber, maintaining the cross-sectional features. Before the preform fabrication, Polycarbonate (PC) rods, tubes (Mcmaster), and films (Laminated Plastics) were baked in a vacuum oven at 80~ 90 °C for at least one week. This process ensured that no water molecules were left inside the material. For the fiber without a microfluidic channel, 4 square grooves, perpendicular to one another, were milled from a PC rod with a diameter of 2.5 cm. The side of the square grooves was 0.625 cm. The Teflon rods with a diameter of 0.625 cm were inserted into the square grooves. Then, the intermediate preform was rolled with thin PC films. The thickness of the preform after the roll was 3.125 cm. The preform was consolidated in a vacuum oven at 190 °C for 10 minutes on four different sides. The four Teflon rods were taken out of the preform after the consolidation. The purpose of the Teflon rods was to minimize the deformation of the square grooves during consolidation. For the fiber with a microfluidic channel,

the dimensions and the steps are identical after the PC tube fabrication. A PC tube is consolidated by rolling the PC films on a Teflon rod with a diameter of 0.625 cm. The diameter of the PC rod was 2.5 cm. The next steps follow the previous preform fabrication steps.

The preform was mounted into the furnace with three temperature zones. The four copper wire spools were each mounted on a ball bearing near the top of the preform, and the wires were fed through the four hollow channels in the preform (Convergence Drawing). Another way of obtaining metal-embedded fibers is through the traditional drawing method, where low-melting temperature metals, such as BiSn, are embedded in the preform. The temperatures used during the fiber drawing were 150 °C (top), 280°C (middle), and 110 °C (bottom). The feeding speed of the preform was set to 2 mm/min. The diameter of the fiber was controlled by varying the drawing speed, which was tuned in the range between 0.3 and 4 m/min. In order for copper wires (80 μm) to be properly inscribed in the square grooves, the diameter of the preform had to be reduced by 62.5 folds; the aimed diameter of the fiber was 400μm. Fibers with a diameter larger than 400 μm might not hold the electrodes in place, while fibers with a diameter smaller than 400 μm will have a deformed cross-section, possibly clogging the microfluidic channel.

Femtosecond Laser Micromachining Setup

A regenerative Ti: Sapphire femtosecond laser with the emission wavelength of 800 nm and ~100 fs pulse width was used in the fabrication (Coherent Libra Series). The laser emits a collimated Gaussian beam with a beam waist of 3 mm. A half-wave plate and a linear polarizer were implemented to control both the power and polarization of the light. In this fabrication, no apparent polarization dependence was observed. Then, the light was focused onto the fiber surface through a 10X dry objective (Nikon, NA: 0.25). The same objective was also used to implement an inverted reflected light microscopy, which was used to monitor the micromachining process in

real-time. The reason for an inverted design, instead of an upright design, was to reduce the re-deposition during the laser micromachining process. The pulse energy used in the fabrication was 0.6 and 1 μJ, and the repetition rate was 100 Hz, which was selected to maintain decent machining efficiency while minimizing the thermal effect. The excessive thermal effect would damage the surrounding region of the targeted position. In order to accommodate the non-flat surface of the fibers, we used a custom-built system which is equipped with a rotational stage along the fiber axis to precisely position the interested area towards the laser pulses.

The smallest feature size of the femtosecond laser micromachining is tunable, depending on the numerical aperture (NA) of the objective lens. In this work, we used a 0.25 NA objective lens which has a smallest feature size of around 10 micrometers. The choice of this value is to balance the processing time and the details of our windows, which is around hundreds of micrometers. We have previously achieved a 1 micrometer feature size on polymer materials with a 0.75 NA objective lens.

The fiber was mounted on a customized holder, which was further mounted on an assembled 4-axis computer-controlled motion stage, including linear translations in x, y, z directions (ASI MS-2000, ASI LS-50, and Newport UTM50CC) and rotations around fiber axial direction (Thorlabs PRM1Z8). Necessary manual kinetic mounts were also implemented to ensure the parallelism between the fiber and the stage's translation axis. The micro-hole was machined via the line-by-line and layer-by-layer method. The size of the machined mark for a single pulse was roughly 10 μm in diameter, and thus the center-to-center distance between lines was set at 5 μm to ensure sufficient overlap. The scanning speed of each line was 150 μm/s.

Cell Culture

Malignant glioma cells, U251 (Sigma Aldrich, 09063001), were cultured in Dulbecco's Modified Eagle's Medium (DMEM) supplemented with a 10% fetal bovine serum (Sigma-Aldrich, St. Louis, MO, USA) and a 1% penicillin/streptomycin (Invitrogen, Carlsbad, CA, USA). The cells were incubated at 5% CO_2 and 37 ℃. The media was changed every other day, and the cells were passaged at around 90% confluence.

Collagen Scaffold Preparation

3D printed wells were designed as the treatment chambers to carry the hydrogel and the fiber microprobe. The inner diameter of the chamber was 1 cm. To insert the fiber probe into the chamber, we created Φ=1 mm holes at the wells' front and rear sides. These holes were 0.5 mm higher than the bottom of the chamber. After the insertion of the microprobe, each hole was fixed with medical epoxy. The custom-designed chambers were sterilized by UV light before seeding the collagen with cells. For the 3D scaffold, 10× DMEM (10% total volume, Sigma Aldrich) and 1 N NaOH (about 2% collagen volume, Sigma Aldrich) were added to the collagen to mediate its pH neutralization. U251 cell suspension and its media were added to obtain the final concentration of the collagen to be 5 mg/mL and the cell concentration to be 2×10^6 cells/mL. To ensure immersion of the fiber probe in the thin hydrogel layer, we transferred the cell-seeded collagen hydrogel to each well to achieve a final thickness of 1.5 mm. Then, the chambers were placed in a Φ=10 cm Petri dish. The Petri dish was left in the incubator for 30 minutes, where the collagen polymerized. 600 μL cell culture media was added to each well after the collagen polymerization, and the collagen scaffolds were incubated for 24 hours before electroporation treatments.

Electroporation Set-up

To deliver the electrical pulses to the scaffold, we connected the two copper electrodes from the immerged microprobe to the pulse generator (BTX, Harvard Apparatus, Holliston, MA, USA). Both test and control groups were connected to the generator. However, the treatment pulses were only applied to the test groups. An oscilloscope (DPO2002B, Tektronix Inc., Beaverton, Oregon), combined with a high voltage probe (Enhancer 3000, BTX, Holliston, MA) and current sensor (3927, Pearson Electronics, Palo Alto, CA) were used to record the applied voltage and the response current.

Electroporation Assessment

To observe the reversible electroporation effect, we dyed the cells in the scaffold before the treatment. We observed the electroporation effect immediately after the pulsing. The media in each well was aspirated and replaced with 300 μL dye solution, containing 1 μM YO-PRO-1 (Thermo Fisher Scientific) and 2.5 μg/mL Calcein red AM (Thermo Fisher Scientific). The petri dish containing the wells was wrapped in aluminum foil to avoid any exposure to light. The scaffolds with the dyes were placed in the incubator for 30 minutes before treatment. The microprobes with the microfluidic channel windows were used for the RE test. After the treatment, every scaffold was imaged using a Zeiss LSM880 (Carl Zeiss Microscopy, NY) laser scanning confocal microscope.

For irreversible electroporation, the scaffolds were treated before staining. The cell culture media was aspirated from each well before treatment. We used the microprobes without any microfluidic channels for IRE treatment. After treatment, 600 μL media was added to each well and incubated for 24 hours before staining. The media was aspirated then replaced by 300 μL of 2.5 μg/mL Calcein green AM and 15 μg/mL PI dissolved in phosphate-buffered saline (PBS) to dye the live and dead cells, respectively. The aluminum foil-wrapped petri dish was used to place

the wells to avoid light, and the dyed samples were incubated for 30 minutes. After the staining solution had been aspirated and the samples were washed twice by PBS, the wells were imaged using the confocal microscope. To examine the ablation area at various planes, we used the Z-stack scanning with a step size of 5 μm to capture the images from bottom to top. Zeiss ZEN 3.0 (Carl Zeiss Microscopy, NY) was used to control the confocal microscope and export the images for the following analysis. The images were processed using a custom-written Matlab script to determine the ablation area and volume.

Numerical Model

A cylinder with a diameter of 1 cm and a thickness of 1.5 mm was built in a commercial finite element package (COMSOL Multiphysics, v5.6, Stockholm, Sweden) to represent the scaffold. A model of the fiber probe, four copper wires enclosed by a polycarbonate cylinder, was placed in the middle of the scaffold representation. The two neighboring wires were exposed to the scaffold in a 40 x 200 μm window. The center-to-center distance of the windows was 0.95 mm. All these dimensions were the averaged measurement results from the fabricated fibers. The aimed dimension of the window and the center-to-center distance were 40 x 150 μm and 1mm. The electric field distribution in the hydrogel was solved by the Laplace equation (1), and the Joule heating during the treatment was considered to estimate the temperature rise during the treatment. The temperature was calculated by the heat transfer equation (2):

$$-\nabla^2(\varphi) = 0 \tag{1}$$

$$-\rho c_p \frac{\partial T}{\partial t} = \nabla \cdot (k\nabla T) + Q_J \tag{2}$$

where φ is the electric potential in the domain. ρ is the tissue density, c_p is the specific heat capacity of the tissue, k is the thermal conductivity of the tissue. Q_J is the Joule heating.

The electric and thermal properties of collagen were obtained from Arena et al.[57], as shown in Table I. The electrode (Copper) property is from the COMOL Material Library. The pulse parameters for the simulation were 200 pulses with an amplitude of 500 V, pulse width of 100 μs, and a repetition rate of 1 Hz, which were employed in the IRE experiment in the study.

Table I. The physical properties used in the simulation

Parameter	Electrode	Collagen scaffold
k ($W \cdot m^{-1}K^{-1}$)	400	0.6
c ($J \cdot kg^{-1}K^{-1}$)	385	4181.8
ρ ($kg \cdot m^{-3}$)	8940	997.8
σ ($S \cdot m^{-1}$)	5.998×10^7	1.2

The electric field threshold of the irreversible electroporation was obtained by matching the volume wrapped in the electric field isosurface to the measured ablation volume.

4.5 Reference

1. Jordan, C.A., Neumann, E. & Sowers, A.E. Electroporation and electrofusion in cell biology. (Springer Science & Business Media, 2013).
2. Tsong, T.Y. in Electroporation and electrofusion in cell biology 149-163 (Springer, 1989).
3. Weaver, J.C. & Chizmadzhev, Y.A. Theory of electroporation: a review. *Bioelectrochemistry and bioenergetics* **41**, 135-160 (1996).
4. Neumann, E., Schaefer-Ridder, M., Wang, Y. & Hofschneider, P. Gene transfer into mouse lyoma cells by electroporation in high electric fields. *The EMBO journal* **1**, 841-845 (1982).
5. Luo, D. & Saltzman, W.M. Synthetic DNA delivery systems. *Nature biotechnology* **18**, 33-37 (2000).
6. Luxembourg, A., Evans, C.F. & Hannaman, D. Electroporation-based DNA immunisation: translation to the clinic. *Expert opinion on biological therapy* **7**, 1647-1664 (2007).
7. Mir, L.M., Orlowski, S., Belehradek, J. & Paoletti, C. Electrochemotherapy potentiation of antitumour effect of bleomycin by local electric pulses. *European Journal of Cancer and Clinical Oncology* **27**, 68-72 (1991).
8. Sersa, G., Cemazar M Fau - Miklavcic, D. & Miklavcic, D. Antitumor effectiveness of electrochemotherapy with cis-diamminedichloroplatinum(II) in mice.
9. Kotnik, T., Rems, L., Tarek, M. & Miklavčič, D. Membrane electroporation and electropermeabilization: mechanisms and models. *Annual review of biophysics* **48**, 63-91 (2019).

10. Ginn, S.L., Alexander, I.E., Edelstein, M.L., Abedi, M.R. & Wixon, J. Gene therapy clinical trials worldwide to 2012–an update. *The journal of gene medicine* **15**, 65-77 (2013).
11. Adam, R. et al. A comparison of percutaneous cryosurgery and percutaneous radiofrequency for unresectable hepatic malignancies. *Archives of surgery* **137**, 1332-1339 (2002).
12. Davalos, R.V., Mir, L. & Rubinsky, B. Tissue ablation with irreversible electroporation. *Annals of biomedical engineering* **33**, 223 (2005).
13. Edd, J.F., Horowitz, L., Davalos, R.V., Mir, L.M. & Rubinsky, B. In vivo results of a new focal tissue ablation technique: irreversible electroporation. *IEEE Transactions on Biomedical Engineering* **53**, 1409-1415 (2006).
14. Goldberg, S.N. et al. Percutaneous radiofrequency tissue ablation: does perfusion-mediated tissue cooling limit coagulation necrosis? *Journal of Vascular and Interventional Radiology* **9**, 101-111 (1998).
15. Miller, L., Leor, J. & Rubinsky, B. Cancer cells ablation with irreversible electroporation. *Technology in cancer research & treatment* **4**, 699-705 (2005).
16. Mirza, A.N. et al. Radiofrequency ablation of solid tumors. *Cancer journal (Sudbury, Mass.)* **7**, 95 (2001).
17. Simon, C.J., Dupuy, D.E. & Mayo-Smith, W.W. Microwave ablation: principles and applications. *Radiographics* **25**, S69-S83 (2005).
18. Friedman, P.L., Wang, P. & Cravalho, E.G. (Google Patents, 1992).
19. Jiang, C., Davalos, R.V. & Bischof, J.C. A Review of Basic to Clinical Studies of Irreversible Electroporation Therapy. *IEEE Transactions on Biomedical Engineering* **62**, 4-20 (2015).
20. Onik, G. & Rubinsky, B. in Irreversible electroporation 235-247 (Springer, 2010).
21. Hsiao, C.Y. & Huang, K.W. Irreversible Electroporation: A Novel Ultrasound-guided Modality for Non-thermal Tumor Ablation. *J Med Ultrasound* **25**, 195-200 (2017).
22. Zhao, Y., McKillop, I.H. & Davalos, R.V. Modeling of a single bipolar electrode with tines for irreversible electroporation delivery. *Computers in Biology and Medicine* **142**, 104870 (2022).
23. Aycock, K.N. & Davalos, R.V. Irreversible Electroporation: Background, Theory, and Review of Recent Developments in Clinical Oncology. *Bioelectricity* **1**, 214-234 (2019).
24. Fox, M. et al. Electroporation of cells in microfluidic devices: a review. *Analytical and bioanalytical chemistry* **385**, 474 (2006).
25. Kim, J.A. et al. A novel electroporation method using a capillary and wire-type electrode. *Biosensors and Bioelectronics* **23**, 1353-1360 (2008).
26. Lee, W.G., Demirci, U. & Khademhosseini, A. Microscale electroporation: challenges and perspectives for clinical applications. *Integrative Biology* **1**, 242-251 (2009).
27. Zabzdyr, J.L. & Lillard, S.J. New approaches to single-cell analysis by capillary electrophoresis. *TrAC Trends in Analytical Chemistry* **20**, 467-476 (2001).
28. Yeung, E.S. Study of single cells by using capillary electrophoresis and native fluorescence detection. *Journal of Chromatography A* **830**, 243-262 (1999).
29. Jankowski, J.A., Tracht, S. & Sweedler, J.V. Assaying single cells with capillary electrophoresis. *TrAC Trends in Analytical Chemistry* **14**, 170-176 (1995).

30. Sedgwick, H., Caron, F., Monaghan, P.B., Kolch, W. & Cooper, J.M. Lab-on-a-chip technologies for proteomic analysis from isolated cells. *Journal of The Royal Society Interface* **5**, S123-S130 (2008).
31. Ouyang, M., Hill, W., Lee, J.H. & Hur, S.C. Microscale Symmetrical Electroporator Array as a Versatile Molecular Delivery System. *Scientific Reports* **7**, 44757 (2017).
32. Kim, J.A. et al. A multi-channel electroporation microchip for gene transfection in mammalian cells. *Biosensors and Bioelectronics* **22**, 3273-3277 (2007).
33. Garcia, P.A., Ge, Z., Moran, J.L. & Buie, C.R. Microfluidic Screening of Electric Fields for Electroporation. *Scientific Reports* **6**, 21238 (2016).
34. Geng, T. et al. Flow-through electroporation based on constant voltage for large-volume transfection of cells. *Journal of Controlled Release* **144**, 91-100 (2010).
35. Verpoorte, E. Microfluidic chips for clinical and forensic analysis. *Electrophoresis* **23**, 677-712 (2002).
36. Jain, T. & Muthuswamy, J. Bio-chip for spatially controlled transfection of nucleic acid payloads into cells in a culture. *Lab Chip* **7**, 1004-1011 (2007).
37. Kulbacka, J. et al. Ultrathin glass fiber microprobe for electroporation of arbitrary selected cell groups. *Bioelectrochemistry* **135**, 107545 (2020).
38. dal Maschio, M. et al. High-performance and site-directed in utero electroporation by a triple-electrode probe. *Nature Communications* **3**, 960 (2012).
39. Nomura, T., Nishimura, Y., Gotoh, H. & Ono, K. Rapid and efficient gene delivery into the adult mouse brain via focal electroporation. *Scientific Reports* **6**, 29817 (2016).
40. Saito, T. & Nakatsuji, N. Efficient gene transfer into the embryonic mouse brain using in vivo electroporation. *Developmental biology* **240**, 237-246 (2001).
41. Judkewitz, B., Rizzi, M., Kitamura, K. & Häusser, M. Targeted single-cell electroporation of mammalian neurons in vivo. *Nature Protocols* **4**, 862-869 (2009).
42. Peirce, J., Chesler, E., Williams, R. & Lu, L. Genetic architecture of the mouse hippocampus: identification of gene loci with selective regional effects. *Genes, Brain and Behavior* **2**, 238-252 (2003).
43. Jacobs, L.F., Gaulin, S., Sherry, D.F. & Hoffman, G.E. Evolution of spatial cognition: sex-specific patterns of spatial behavior predict hippocampal size. *Proceedings of the National Academy of Sciences* **87**, 6349-6352 (1990).
44. Li, C. et al. Picosecond Pulse Electrical Field Suppressing Spike Firing in Hippocampal CA1 in Rat In Vivo. *Bioelectromagnetics* **41**, 617-629 (2020).
45. Lorenzo, M.F. et al. Temporal Characterization of Blood-Brain Barrier Disruption with High-Frequency Electroporation. *Cancers (Basel)* **11**, 1850 (2019).
46. Sharabi, S. et al. Transient blood-brain barrier disruption is induced by low pulsed electrical fields in vitro: an analysis of permeability and trans-endothelial electric resistivity. *Drug Deliv* **26**, 459-469 (2019).
47. Temelkuran, B., Hart, S.D., Benoit, G., Joannopoulos, J.D. & Fink, Y. Wavelength-scalable hollow optical fibres with large photonic bandgaps for CO 2 laser transmission. *Nature* **420**, 650-653 (2002).
48. Loke, G., Yan, W., Khudiyev, T., Noel, G. & Fink, Y. Recent Progress and Perspectives of Thermally Drawn Multimaterial Fiber Electronics. *Advanced Materials* **32**, 1904911 (2020).
49. Bayindir, M. et al. Metal–insulator–semiconductor optoelectronic fibres. *Nature* **431**, 826-829 (2004).

50. Gumennik, A. et al. All-in-Fiber Chemical Sensing. *Advanced Materials* **24**, 6005-6009 (2012).
51. Chocat, N. et al. Piezoelectric fibers for conformal acoustics. *Adv Mater* **24**, 5327-5332 (2012).
52. Khudiyev, T. et al. Electrostrictive microelectromechanical fibres and textiles. *Nat Commun* **8**, 1435 (2017).
53. Egusa, S. et al. Multimaterial piezoelectric fibres. *Nat Mater* **9**, 643-648 (2010).
54. Canales, A. et al. Multifunctional fibers for simultaneous optical, electrical and chemical interrogation of neural circuits in vivo. *Nature Biotechnology* **33**, 277-284 (2015).
55. Loke, G. et al. Digital electronics in fibres enable fabric-based machine-learning inference. *Nature Communications* **12**, 3317 (2021).
56. Yuan, R. et al. Microfluidics in structured multimaterial fibers. *Proceedings of the National Academy of Sciences* **115**, E10830-E10838 (2018).
57. Arena, C.B., Szot, C.S., Garcia, P.A., Rylander, M.N. & Davalos, R.V. A three-dimensional in vitro tumor platform for modeling therapeutic irreversible electroporation. *Biophysical journal* **103**, 2033-2042 (2012).
58. Ghilani, C.D. Adjustment computations: spatial data analysis. (John Wiley & Sons, 2017).
59. Moradi, M., Mehrabi, O., Azdast, T. & Benyounis, K.Y. Enhancement of low power CO2 laser cutting process for injection molded polycarbonate. *Optics & Laser Technology* **96**, 208-218 (2017).
60. Ivey, J.W. et al. Targeted cellular ablation based on the morphology of malignant cells. *Scientific Reports* **5**, 17157 (2015).

Chapter 5
Overview and Future Direction

5.1 Overview

Thermal drawing process is a promising platform for fabricating functional fibers integrating vast combinations of materials through unique geometry along the fiber length. The functional fibers open a wide range of applications in different fields such as telecommunication, biomedical engineering, sensing and modulating technology, and photonics and optoelectronics. Specifically, these polymer fibers are implemented in various biomedical fields as neural probes, chemical sensors, tissue scaffolds, cancer and tumor treatments, soft robotics, and smart textiles. In this dissertation, I presented neural interfaces and a biomedical device fabricated with combinations of thermal drawing process, thermal tapering process, bundling techniques, and the femtosecond laser micromachining techniques.

Neural activity is regulated by synapse-neuromodulator interactions, necessitating opto-electro-pharmacological investigations. In chapter 2, we utilized the thermal drawing and tapering process to fabricate T-DOpE probes that can enable simultaneous electrophysiology recording, optogenetics, and drug infusion. These probes have higher density of features compared with the traditional fiber-based neural probes. We implement our multi-modal probes to show focal infusion of synthetic cannabinoid disrupts CA1 theta and SPW-R oscillations. We further show that CB1R agonism disrupts SPW-R generation regardless of CA3 inputs. This emphasizes the importance of cannabinoid signaling for local CA1 circuit computation.

In chapter 3, highly customizable and affordable Tetro-DOpE probes are fabricated by bundling thermally drawn thin multifunctional fibers similar to classical tetrode fabrication. This probe enables simultaneous electrophysiology recording, optogenetic manipulations, and local

drug infusion. Multifunctionalities of Tetro-DOpE probe was demonstrated in head-fixed behaving mice. A six-shank probe was mounted on a microdrive which enabled stable recordings of over months when chronically implanted in freely behaving mice.

Irreversible electroporation has been clinically used to treat tumor cells and showed successful ablation as a standalone treatment. In chapter 4, we developed a microscale electroporation fiber device using the thermal drawing process and the femtosecond laser micromachining techniques. Microscale electroporation was demonstrated in a 3D hydrogel scaffold, where malignant glioma cells (U251) were cultivated inside.

5.2 Future Direction

Leveraging the scalability of the fabrication processes, I envision these functional fibers in hospitals enabling better health care and in research centers pushing the boundaries of fundamental understanding in diseases and their treatments. I outlined some ongoing challenges and potential future directions for thermally drawn flexible multifunctional fibers in biomedical application.

5.2.1 Improvement in fiber design, materials, and functionalities

Currently, there are a limited number of materials commonly used for thermal drawing process. The different thermomechanical properties of the materials limit the possible structure and geometry of a fiber. Although there are preexisting guidelines for materials selections, more rigorous modeling and analysis can or needs to be conducted to achieve an optimal fiber design. Engineering the molecular properties (e.g., high-density and low-density PE) could enable thermal drawing of materials impossible before. Further integration of post-processing, such as laser micromachining, soft lithography, and 3-D printing, along the thermally drawn fiber will increase and/or broaden the functionalities of the fiber. This might enable integration of other functional

materials which are not compatible with the thermal drawing process. Flexibility has always been a strong advantage of thin thermoplastic fibers, yet these fibers are still tougher than most organs and tissues. Either lowering the dimension or changing the materials to integrate more seamlessly with biological matter would increase the biocompatibility of the fibers.

5.2.2 Wireless integration of functional fibers

Thus far, many functional fibers have been developed and presented in peer-reviewed journals. Some functional fibers can afford bulkier back-end electronics, such as smart textile weaved into a bed mat for pressure mapping. However, some fiber could benefit from a more compact, wireless backend connectivity. For example, wireless integration of sweat sensing fiber weaved onto a T-shirt could allow real-time sensing during an exercise. Fully wireless neural fiber probes on freely moving mice can enable new social behavior experiments. It is essential to develop wireless transmission of fiber sensor data, enabling more seamless integration of fiber technology in our daily lives.

5.2.3 Closed-loop feedback control system, in-fiber computation, and artificial intelligence

Multiple functionalities can be embedded into a single fiber enabling bidirectional sensing and actuating. For example, multifunctional fiber neural probes enable extracellular electrophysiology recording while simultaneously manipulating the nearby neural circuits. A closed-loop feedback system could be applied to bidirectional fiber technology enabling real-time treatment or care. For instance, a closed-loop drug infusion or electrical pulses with relevant dosage can be administered after detection or prediction of an epileptic event. Real-time monitoring of the patient's bed pressure map can enable a closed-loop control to disperse high pressures on specific locations to prevent pressure ulcers. In-fiber computation of simple signal processing and data storage can greatly aid the commercial use of fibers, like wireless integration.

These computations should reduce the bulkiness of back-end electronics for closed-loop control. Some of these computations can be as simple as filtering and de-noising and as complex as machine learning and artificial intelligence. Embedding fibers with capabilities of ML and AI would unlock new possibilities in smart textiles and soft robotics. For example, a sweat sensing fiber, temperature sensing fiber, pH sensing fiber, and an AI fiber to notify the user or patient with higher quality information such as dehydration.